NON-COPLANAR ARC OPTIMIZATION FOR STEREOTACTIC ABLATIVE RADIOTHERAPY TREATMENT PLANNING

by:

John David Lincoln

Submitted in partial fulfillment for of the requirements.
for the degree of Doctor of Philosophy

at

Dalhousie University
Halifax, Nova Scotia
August 2023

Dedication

I dedicate this dissertation to my grandfather, the late Victor John Emmanuel Surajdeen. For you, I strive every day to be a leader not a follower.

Table of Contents

List of Tables

List of Figures

Abstract

Stereotactic ablative radiotherapy (SABR) is a technique that delivers a high dose of radiation in a single or small number of fractions and requires rapid fall off outside the target.

In current clinical practice it is imperative when treating with ablative doses that radiation to organs-at-risk (OARs) is minimized as much as possible to avoid treatment related toxicity in healthy tissue. Often SABR is delivered with volumetric modulated arc therapy (VMAT), an efficient delivery technique that relies on complex modulation throughout an arc to optimize dose objectives.

Non-coplanar optimization methods have been proposed to automatically select geometries that minimize overlap between targets and organs-at-risk (OARs) in the radiation beams-eye-view (BEV). When applied in intensity modulation radiotherapy IMRT or VMAT, these have been shown to significantly reduce dose to OARs as compared to conventional coplanar trajectories. These methods still face barriers to widespread clinical implementation, such as efficiency issues.

The purpose of this thesis is to demonstrate that automatically optimized non-coplanar arc geometries for SABR with VMAT leads to dose reductions to OARs. Additionally, this thesis considers the differences between cranial and extracranial SABR and evaluates arc geometry optimization for sites with varying biological complexity.

The thesis is comprised of three manuscripts that evaluate the arc geometry optimization for sites treated with SABR. The first manuscript for cranial SABR, "*Comparison of anatomically informed template trajectories with patient specific trajectories for stereotactic radiosurgery and radiotherapy,"* compares a commercial general arc template with an optimized arc template and patient specific arc geometry, concluding that patient specific geometries were dosimetrically superior. The second manuscript for extracranial SABR, "*Static couch non-coplanar arc selection optimization for lung SBRT treatment planning,"* demonstrates a patient-specific method to choose arcs that combine dose reduction to OARs with clinically acceptable target conformity. The third manuscript for extracranial SABR, "*Biologically optimized non-coplanar arc selection for small and large target volumes in liver SBRT,"* shows that choosing optimized arcs has the potential for dose reduction to target-encompassing OARs, such as the liver.

These manuscripts address differences and similarities of performing SABR in various sites throughout the body. They offer solutions that are ready to use and require minimal additions to current clinical workflows. Finally, they also demonstrate the dosimetric advantages of non-coplanar arc delivery for multiple disease sites.

List of Abbreviations Used

2D – Two dimensional

3D – Three dimensional

AAA – Anisotropic Analytic Algorithm

AXB – Acuros External Beam Algorithm

BAO – Beam Angle Optimization

BEV – Beams-Eye-View

CI – Conformity Index

CRT – Conformal Radiotherapy

CT – Computed Tomography

CTV – Clinical Target Volume

DAO – Direct Aperture Optimization

DCA – Dynamic Conformal Arcs

DICOM – Digital Imaging and Communications in Medicine

DoF – Degrees of Freedom

DVH – Dose Volume Histogram

FFF – Flattening Filter Free

GI – Gradient Index

GTV – Gross Tumor Volum

HD – High Definition

HU – Hounsfield Unit

HyTEC – Hypofractionated Treatment effects in the Clinic

IMRT – Intensity Modulated Radiotherapy

ITV – Internal Target Volume

LINAC – Linear Accelerator

MLC – Multi-leaf collimator

MR – Magnetic resonance

NTO – Normal tissue optimization

OAR – Organ-at-Risk

PDD – Percentage Depth Dose

QUANTEC – Quantitative Assessment of Normal Tissue Effects in the Clinic

PRV – Planning Risk Volume

PTV – Planning Target Volume

RTOG – Radiation Therapy Oncology Group

SABR – Stereotactic Ablative Radiotherapy

SBRT – Stereotactic Body Radiotherapy

Sim - Simulation

SRS – Stereotactic Radiosurgery

SRT – Stereotactic Radiotherapy

SSD – Source to surface distance

SAD – Source to axis distance

TPS – Treatment Planning System

USF – Urgent Sparing Factor

VMAT – Volumetric Modulated Arc Therapy

WHO – World Health Organization

Z – Atomic Number

Acknowledgements

I would like to begin by thanking my supervisor Dr. Chris Thomas for his support, guidance, kindness, and patience. Chris, above all, beyond your clinical and academic excellence, your care and compassion shine brighter than most. Thank you for the privilege of being your PhD student.

Next, I would like to thank my committee members: Dr. Krista Chytyk-Praznik, Dr. Lee MacDonald, and Dr. Alasdair Syme. Thank you all for your continued support as well as the non-trivial task of having to read this dissertation. Lee, thank you even further for laying such strong foundations for all this work, your mentorship, friendship, and patience. I look up to you more than you know. Thank you to my external examiner Dr. Nicolas Ploquin for your invaluable contributions to this dissertation.

I am extremely grateful for the mentorship I received during my time at Dalhousie University. Thank you to Dr. Kevin Hewitt for introducing me to the field of Medical Physics. Thank you to Dr. Tim Bardouille for introducing me to scientific research and for your ongoing friendship. Thank you to Dr. James Robar for the countless opportunities you have offered and your commitment to Medical Physics excellence. Thank you to the AIF group, specifically Brian Little and Gillian Hatcher. Thank you to Dr. Amanda Cherpak for your willingness to help in any capacity, your incredible leadership and professionalism is inspirational. Thank you to Angela Henry for being the undisputed backbone of our Medical Physics department.

I also need to thank Dr. Cody Church. I did not expect to make a lifelong friend during my graduate studies; mammo4eva. To Dr. Gayle MacDonald, thank you. Your excellence is undoubtable, your compassion for students is second to none. To my friends, the family I was fortunate enough to choose, thank you for keeping me sane these last five years.

To Mom: you are the reason I am on this journey, thank you for your endless support and strength, I love you. To Dad: thank you for introducing me to “Frigit” and teaching me that growth is never out of reach, I love you. To Michelle: you have taught me so much, thank you for showing me that ***anything*** is possible, I love you. To Sophie and Curio: I love you both.

Lastly and most importantly, to Breagh: thank you for your love and being on this journey with me, I love you so much.

1 Chapter 1: Introduction

1.1 Preface

Statistics Canada’s 2022 report on cancer prevalence concluded that eastern Canada (Nova Scotia, New Brunswick, Prince Edward Island, and Newfoundland & Labrador) experiences a greater incidence of cancer than anywhere else in the country[1]. The prevalence in Nova Scotia over the last 25 years has been ~50,000 cases with ~20,000 of these diagnoses happening in the last 5 years[1]. It is expected that one in two Canadians will develop cancer, and that half will receive radiation therapy. This implies that approximately 10,000 Nova Scotians with cancer required radiation therapy in the last 5 years. Improving techniques like SABR for many disease sites could reduce the burden on patients by reducing the fraction number, which could provide greater access to those who may not currently elect for radiotherapy due to socioeconomic or other barriers.

It is important to note that although statistics are meaningful especially in the context of aggregated data, each Nova Scotian/Canadian/individual living with cancer is first and foremost a human being. The World Health Organization (WHO) constitution[2] states “The enjoyment of the highest attainable standard of health is one of the fundamental rights of every human being without distinction of race, religion, political belief, economic or social condition”. Medical research advances of which the work in this thesis exemplifies, should heed the same powerful sentiment when considering the implications of clinical translation.

The aim of treatment planning in radiation therapy is to deliver a therapeutic dose of radiation to a specific anatomical volume[3]. This goal is hindered by the complementary importance of ensuring that while a therapeutic dose is delivered, surrounding normal tissues are avoided[3] or dose to them is maintained below toxic levels. The existence of this trade-off between therapeutic delivery and normal tissue sparing lends itself naturally to optimization. This thesis will focus on specific optimizations to choose arc trajectories for a C-arm linear accelerator (LINAC) that aim to reduce radiation dose to normal tissues.

The manuscripts that comprise this thesis develop and apply methods for arc selection based on specific anatomical locations throughout the body. The methodologies were evaluated in the context of ablative dose regimes where failure to deliver radiation precisely could have potentially toxic or, in worst-case scenarios, lethal consequences. In all cases, the treatment plans developed with the experimental methodology were compared with expert-planned clinical treatment plans to ensure that any dosimetric benefits or shortcomings were fairly compared to the clinical standard. Currently VMAT[4] arcs are not chosen with rigour or patient specificity. The former has the potential to cause plan variability, while the latter omits a potentially important optimization. The purpose of this research is to facilitate and automate the choice of arc selection during SABR treatment planning in terms of OAR avoidance.

This research is applicable and current in the field of radiotherapy. Methods that have shown dosimetric improvement using ablative doses in the cranium were extended to thoracic and abdominal anatomies. Optimizing VMAT arc placement has the potential to support clinical translation to fully dynamic axes optimization which has proven superior delivery efficiency of non-coplanar VMAT[5-7] as compared to static arcs.

1.2 Background

Radiation is defined as energy in the form of particles or waves, that has the potential to interact with matter as it travels through space. Ionization is the physical process by which an electron is removed from matter. Radiation is categorized as non-ionizing when it does not have the ability to ionize the matter it interacts with, and ionizing when it can ionize the matter it interacts with either directly, or indirectly[8]. Radiation has been used for medical purposes since 1895 when Wilhelm Roentgen discovered the "X-Ray" and its potential for medical imaging[9]. From this discovery, the scientific field of radiology was born with a broad scope of understanding applications of radiation in medicine through diagnosis and treatment of disease. The focus of this thesis concerns the treatment of disease.

Current medical practice is made possible by the many technological advances that have occurred since Roentgen's discovery. Treating disease with radiation can use a variety of radiation types. Electrons, photons, protons, and heavy ions can all be used to treat disease. The focus of this thesis will be on x-ray photons delivered via external beam radiotherapy (EBRT) using a LINAC.

The main disease indicated for treatment with radiation is cancer, which will be the focus of this thesis. Cancer is a disease whereby an abnormal cellular response occurs in the body that signals cells to replicate uncontrollably[10]. The result is masses of these cells, commonly referred to as tumours. Tumours can be classified as benign (noncancerous) when their growth is controlled and does not invade surrounding tissues. However, when tumour growth is uncontrollable and has the ability to metastasize into neighbouring organs they are classified as malignant[10].

Radiation has the potential to stop the growth of tumours by physically disrupting critical chemical bonds and cellular processes. The field of radiobiology concerns the impact of ionizing radiation on biological tissues and living organisms. A discussion on radiobiology and the radiobiology of SABR is found in Chapter 2.

The contents of this thesis apply radiation as a treatment modality for cancer by optimizing the arc selection component of the VMAT treatment planning process. Throughout the thesis we aim to optimize the incident direction of beams generated from an external beam megavoltage (MV) x-ray photon spectrum to spare OARs while ensuring adequate tumour coverage.

1.3 Motivation

This thesis is primarily motivated by the knowledge that OAR dose reduction in radiotherapy is correlated with decreased normal tissue complication probability[10], which in turn relieve patients of the burden of side effects, potentially improve their quality of life, and reduce health care burdens[10]. Furthermore, in the context of non-coplanar optimization techniques, this thesis demonstrates the complex nature of trade-offs associated with treatment planning. Motivated by pathfinding algorithms that already exist and the anatomical sites for which they have been developed, this thesis extends the development of pathfinding algorithms to consider suitability for clinical implications in the context of conformity and delivery efficiency. Efficiency will be defined for the purpose of this work as the combination of factors that influence treatment time such as number of monitor units and number of arcs.

Another motivation to the research presented in this thesis is the ability for algorithms and techniques being developed to be translated from cranial sites to extracranial sites. Chapter 3 will provide more in-depth insights into the myriad of techniques that have been developed in the space of non-coplanar trajectory radiotherapy that were summarized in a 2019 review paper[11]. Furthermore, this review specifically highlighted a deficiency in the literature for static-couch non-coplanar arcs applied outside of the cranium. Many non-coplanar techniques have been limited to the cranium due to the lower probability of mechanical collisions. The biological response to radiation has been well established in the cranium and extracranially where the probabilities of normal tissue complication of many OARs are correlated to maximum dose tolerances and dose volume constraints. Extending these optimizations to extracranial sites must consider not only the differing biological response to radiation of OARs, some of which do not have maximum dose tolerances, but also the much higher probability of mechanical collision with the body for many more non-coplanar geometric orientations.

The final motivation was considerations that could facilitate the clinical translation of these methods and their potential for improving clinical practice. Overcoming efficiency concerns in non-coplanar IMRT has been the subject of many studies that propose dynamic rotations and translations of LINAC axes as a solution that maintains the same dose reductions with fast deliveries[11]. Fully dynamic axes optimizations have not yet been fully integrated into regulatory approved treatment planning systems or delivery by any vendor. There are still unanswered questions concerning standardized quality assurance methodologies such as dose verification, in a fully dynamic axes setting. Not only is static-couch VMAT used by many radiotherapy clinics worldwide, but there are also well-established protocols concerning dose verification and end-to-end testing with this technique. Pushing the limits of static-couch non-coplanar arc optimization could identify areas where dynamic axes are needed, which could in turn provide a stronger argument for its clinical translation.

1.4 Research Objectives

The overarching theme of this thesis is to provide methodologies to automatically select arcs for VMAT that aim to improve OAR sparing in both cranial and extracranial SABR. These arcs leverage two degrees of freedom on a medical LINAC, specifically couch and gantry rotations.

OAR sparing is quantified by dose volume objectives that quantify the acceptability of a plan based on established constraints in radiation oncology. In this thesis we focus primarily on maximum doses to the serial OARs in cranial indications, while extracranial indications have a mix of serial and parallel OARs that require dose-volume and maximum dose considerations. Minimizing doses to OARs has the potential to reduce the incidence of normal tissue complication probability, which is imperative in the context of ablative doses.

This thesis also maintains a focus on the ability of the developed technologies to be translated into clinical practice with minimal additions to current workflows. The techniques in this thesis are generalizable to the well-established clinical procedure of static couch arc VMAT delivery using a C-arm linear accelerator. They are independent of vendor and treatment planning system (TPS). This thesis aims to show that the arc selection process can be patient specific and automated, while incorporating considerations for treatment time. Competing techniques discussed in Chapter 3 each lack in specific areas that pose barriers to widespread clinical adoption. This research leverages the efficiency and modulation of VMAT, aiming to improve the process by giving optimized initial geometry inputs. All comparisons in this work are made using the same systems as in routine clinical practice. As the arc geometries used in this thesis, do not include dynamic trajectories, these methods do not require any additional types of quality assurance that may be required for implementation of fully dynamic axes rotation and/or translation.

In the manuscripts comprising this thesis the differences between cranial and extracranial treatment planning are addressed. Their methods for optimization have the potential to differ if adequate considerations are not made, specifically in terms of how different organs of the body respond to hypo-fractionated photon therapy. Thus, optimal arcs have the potential to differ on a patient-specific basis and site-specific basis. All these concepts and information can be built into an algorithm that selects optimized arcs before VMAT is applied for modulation.

This thesis is comprised of three manuscripts, each addressing a different anatomical site to investigate optimized arcs for SABR dose reduction.

1.5 Thesis Structure

The first chapter in this dissertation serves as an overview of the entire work. Its sections highlight the relevant background and motivation for choosing optimized arcs to use with VMAT in SABR.

The second chapter focuses on SABR and the anatomical sites where it is currently used. It describes the radiobiological differences between SABR techniques compared to standard fractionation treatments. This chapter continues examining the recently published HyTec reports, that contain the most current dose-volume constraints in SABR based on clinical endpoints. The next section examines SABR delivery methods with a brief history and focus on inverse optimization. The chapter concludes with a summary of the clinical dose calculation algorithms used throughout this thesis.

The third chapter changes focus to the algorithmic details concerning non-coplanar optimizations. The 4π nomenclature is briefly discussed, followed by cost equation development and strategies to navigate through radiotherapy delivery space. A distinction is then made between the algorithmic differences that pertain to cranial and extracranial SABR individually. Methods to mitigate and overcome these differences are then discussed in terms of algorithms required to generate cost scores and then optimizing trajectories through pathfinding algorithms.

Manuscript 1 is presented in chapter 4. This manuscript is the sole work of the thesis that focussed on SABR inside the cranium, referred to as SRS/SRT. The manuscript uses a previously published cost equation and arc trajectory navigation algorithm to develop and dosimetrically evaluate anatomically informed class solution template trajectories compared to patient-specific trajectories and a geometric arc template. Each of these solutions were optimized as static-couch gantry arc trajectories, where increasing levels of complexity were hypothesized to reduce doses to OARs. Treatment planning was semi-automated to ensure a reproducible methodology and foreshadow fully automated planning.

Manuscript 2 is presented in chapter 5. This manuscript presents a methodology for optimizing utilizing a cost map that is not limited by the size of an OAR like that in chapter 4. Given a newly constructed cost map, a stochastic algorithm for arc selection was created to balance contributions of overlap cost with a trajectory arc spacing metric called mean arc distance (MAD)[12]. These arc configurations were evaluated for 18 lung SBRT cases and dosimetrically compared with a clinical 190° arc template of two coplanar arcs that only varies based on target laterality. VMAT treatment planning was performed by expert treatment planners for both arc geometries using a reproducible methodology that facilitated direct comparisons of arcs.

Manuscript 3 is presented in chapter 6. This manuscript presents a methodology that incorporates high level biological information into the construction of the overlap cost map based on categorizing OARs in terms of their seriality. For each type of OAR, a different type of cost is assigned that best suits the OAR-specific seriality. Arc selection is performed similar to chapter 5 with an additional consideration of treatment efficiency in terms of the number of arcs used. These arcs were evaluated against a clinical arc template spanning 200° for 16 liver SBRT cases with target volume stratified by their size. VMAT treatment planning was performed by expert SABR treatment planners for both arc geometries using a reproducible methodology that facilitated direct comparison of arcs.

The seventh and final chapter brings the contents of all previous chapters together and discusses future work that has the potential to further improve the research presented in this dissertation.

2 Chapter 2: Stereotactic Ablative Radiotherapy (SABR)

In this chapter the rationale behind using SABR is discussed along with the relevant physical and biological theoretical considerations.

2.1 Definition and Motivation

The term “Stereotactic Ablative Radiotherapy” abbreviated to “SABR” derives its nature from the three separate words comprising it. The first word “*stereotactic*” derives its origins from the Greek term “*sterotaxis*” meaning “solid” and “orderly”[13]. Localizing anatomies in three-dimensions (3D) with stereotactic frames allows for coordinate systems to be established with precise geometric positioning. SABR is a radiotherapy procedure that surgically removes or destroys body tissue based on precise geometric localization of anatomy. In current practice, SABR treatment plans are characterized by a highly conformal dose distribution that falls off rapidly outside of the tumour[14].

Historically the term SABR has been used interchangeably with stereotactic body radiation therapy (SBRT) where the distinction is application of the methodology to sites in the body[14]. This has been separate from stereotactic radiosurgery and radiotherapy (SRS/SRT)[15] a methodology pioneered by Lars Leksell for treatments inside the cranium. The SRS methodology preceded its use outside of the body and was dedicated to a single high dose treatment, mirroring traditional surgery, but instead done non-invasively. SRT follows the same methodology but is administered in more than one treatment. The ability to physically ablate disease comes from the nature of delivering a sufficiently high dose of radiation to damage tumour vasculature.

The manuscripts that comprise this thesis adopt the use of SRS/SRT when referring to cranial treatments in Chapter 4, and SBRT when referring to extracranial treatments in Chapters 5 and 6. However, in effort to combine their similarities when referring to the treatment method irrespective of anatomical location, the term SABR is used in this dissertation.

2.2 Radiobiology

Radiobiology is a scientific speciality dedicated to understanding the biological response of tissues to radiation. To this point, the discussion on SABR has focused on delivering a large dose to kill cancerous tumours. This amount of dose is commonly referred to as the prescription dose, dictating the amount of radiation dose that is required to kill a tumour while also mitigating toxicity. These toxicities are quantified using normal tissue complication probabilities (NTCP). The decision for the prescription dose is made by a radiation oncologist by referencing treatment protocols[16-18]. When this prescription dose is divided into multiple treatments of equal smaller doses, it is called fractionation. When the number of fractions is increased, an increase in prescription dose is required to maintain a constant level of tumour control probability (TCP). The prescription dose is essentially a trade-off between TCP & NTCP. While fractionating does not reduce the total dose to normal tissues, the dose is delivered over a longer period. The theory behind fractionation is based on four key concepts in radiobiology[10]:

1. Repair: Repair of cells that were not killed during irradiation causes increased cell survival.
2. Repopulation: Repopulation of cells through cellular division post irradiation causes increased cell survival.

3. Reassortment: Reassortment of cells from a radioresistant phase of the cell cycle to a radiosensitive phase of the cell cycle causes increased cell death.
4. Reoxygenation: Reoxygenation of hypoxic cells post irradiation causes them to become more radiosensitive.

These concepts apply to all cells, however in most cases normal healthy tissues are not hypoxic. Repair and repopulation aim to ensure cell survival of normal healthy tissues, while also prolonging the survival of tumour cells. Reassortment and reoxygenation focus on increasing tumour cell kill, while also potentially increasing cell kill in normal healthy tissues.

Modelling the extent to which cell kill occurs was a focus of Fowler who introduced the linear-quadratic (LQ) model[19]. This model states that cell survival is dependent on two factors: the first being the sum of all lethal damage that occurs from a single radiation event, and the second being the combination of all sublethal damage events that become lethal. Parameterizing these concepts yields equation 2.1 summarizing the LQ model for fractionated deliveries:

$$S = e^{-(\alpha D + \beta d D)} \tag{2.1}$$

Where *S* is the amount of cell kill defined as the surviving fraction, α is the parameter describing the linear component of the LQ model, β is the parameter describing the quadratic component of the LQ model with *d* and *D* being the fractional and total dose delivered, respectively.

This model works well for fractionated radiotherapy treatment regimes defined by a standard fractionation of 2 Gy per fraction. However, SABR is typically delivered in a small number of fractions (1 to 5, typically)[14]. Arguments have been made both for and against using the LQ model for SABR [20], with advantages citing the well established validation of the model up to ~20 Gy per fraction, and limitations concerning the discrepancies with the model at commonly used ablative doses.

One tenet that the LQ model does not account for is the extent to which ablation plays a role in cell survival. Ablative doses used in SABR that exceed 10 Gy per fraction have the capacity to physically damage tumour vasculature which has the potential to cease blood flow providing a mechanism for indirect cell kill[14]. This theory also holds for healthy normal tissues; therefore, it is imperative to avoid ablation of these organs when treating with these doses. Although some research groups have tried to modify the LQ model for SABR to account for behaviours seen experimentally, it is important to note that they use mathematics in an attempt to describe biological effects that are not well established[20].

Another aspect of radiobiology that is not explicitly outlined in the four concepts above nor in the linear quadratic model, concerns the seriality of healthy normal tissues. Seriality can be defined in terms of functional subunits of any organ. The underlying assumption is that all organs can be divided into subunits, which can be classified as functional or non-functional after being exposed to radiation. An organ is considered serial when any subunit becoming non-functional after radiation has the potential to cause the entire organ to fail. In contrast, an organ is considered parallel when many or all the subunits must become non-functional after being exposed to radiation to cause the entire organ to fail. This is reflected in the dose tolerances ascribed various OARs during treatment planning. At a high level, when an OAR is considered serial its dose tolerance will be subject to a maximum dose that any part of that OAR should not exceed that dose. Comparatively, when an OAR is considered parallel its dose tolerance will be subject to a dose volume constraint such that no more than a specific volume of that OAR should succeed a specific dose.

In practice, some OARs exhibit a spectrum of seriality making it difficult to classify them as only serial or only parallel. The generalized equivalent uniform dose (gEUD) formalism provides a mathematical model to characterize tumours and organs based on their seriality using dose-volume histograms (DVH). It is defined as the biologically equivalent dose that causes the same cell kill when delivered uniformly to a structure, that a non-uniform dose distribution would[21]. This formalism is defined in Equation 2.2:

$$gEUD = \left(\sum_{i=1}^{N} v_i D_i^a \right)^{1/a} \tag{2.2}$$

where v_i and D_i are volume and dose bins of a DVH, and a is a tissue specific parameter. The equation suggests that *gEUD* is bound by the minimum and maximum doses to the structure in question, with the specific case of $a = 1$ yielding equivalence to the structure's mean dose. Here, a is defined as a negative value for all tumours and a positive value for all normal structures. In the limiting case where a approaches negative and positive infinity, *gEUD* approaches the minimum and maximum dose, respectively.

The discussion on gEUD is relevant to this thesis as various research groups have incorporated it into their non-coplanar optimizations[22-25] as an optimization objective for biological consideration. The manuscript presented in Chapter 6 aims to address biological seriality without requiring DVH calculations to make distinctions between serial and parallel organs. Moreover, it addresses how non-coplanar optimizations could consider serial, parallel, and parallel encompassing OARs individually in terms of type of cost that can be attributed.

2.3 Treatment Sites Under Consideration

This section elaborates on the specific indications that SABR is used for in cranial and extracranial settings.

2.3.1 Cranial

Intracranial SABR, commonly referred to as SRS/SRT, is used to treat a wide variety of indications. The most common use is to treat cranial metastases that occur in patients that have a primary cancer elsewhere in the body[26]. For these treatments, SABR has been compared with whole brain radiation therapy (with and without hippocampal avoidance) (WBRT)[16] and surgical resection[27]. It has also been delivered alone with promising median survival compared to the other combinations of SABR, whole brain, or standard fractionation[28]. Other indications include pituitary adenomas, meningiomas, arteriovenous malformations, trigeminal neuralgia, vestibular schwannomas (acoustic neuromas) and glial tumours (gliomas)[26]. The Radiation Therapy Oncology Group (RTOG) 9005 defines prescription doses for metastases whose diameter measures less than or equal to 2 cm as 24 Gy[26] in a single fraction. These doses scale with an inverse relationship to the size of the target volume where target diameters measuring between 3 and 4 cm can be prescribed up to 15 Gy, while between 2 and 3 cm can be prescribed up to 18 Gy. These cranial indications all share similar organs-at-risk (OAR) structures. Since most cranial structures inside the brain are functionally serial, they are subject to maximum dose constraints. Of primary importance to avoid is the brainstem, optic chiasm, both optic lenses, both optic nerves, and both eyes. Each of these structures therefore has a maximum dose tolerance that will be discussed further in section 2.4 in terms of their clinical end points. The hippocampus and normal brain also have important avoidance priorities but are functionally parallel, having specific dose volume constraints. Multiple cranial metastases are also treated with SABR however, multiple metastases were not the focus of the work in this dissertation.

SABR for cranial indications has been widely studied in the context of non-coplanar optimizations[5,6,12,29-36], nevertheless wherever improvements are possible they should be leveraged and translated if possible, in appropriate clinical settings.

In the manuscript of Chapter 4, treatment plans were created that simulated various geometric locations of a singular cranial target volume with varying size inside the cranium. The goal of this research was to demonstrate that for various anatomical locations throughout the brain, that a patient-specific set of optimized non-coplanar arcs could outperform both an anatomical and geometric template arc solution in terms of reducing maximum doses to cranial OARs mentioned above.

2.3.2 Extracranial

Extracranial SABR, commonly referred to as SBRT or simply SABR, is used to treat a wide variety of indications that reside outside of the cranium. Its extension outside of the cranium has primarily focused on organs that can tolerate ablative doses without losing physiological function[11,26]. Parallel organs such as lung and liver were therefore deemed the early sites for testing the efficacy of SABR outside of the cranium. Spinal indications were also an early site for testing extracranial SABR[11,26], however this disease site was not the focus of this dissertation.

One of the most common cancers in the world is lung cancer, specifically non-small cell lung cancer (NSCLC) and lung metastases, with close to one million cases per year worldwide[26]. In patients that are not considered surgical candidates due to various comorbidities involving the lung or proximal organs, radiotherapy initially offered a solution to supplement the potential for limited resection. A standard fractionation over the course of six to seven weeks was found to be unfavourable compared to anatomical resection[37]. Limitations included simple beam arrangements and modest doses to ensure safety, which lead to high rates of local failure and undesirable toxicity to the lung such as radiation induced pneumonitis. Adapting the techniques already used in intracranial SABR allowed for these clinical challenges to be resolved. Delivering high doses of radiation with a high degree of conformality in few fractions was able to significantly decrease rates of local failure, while also decreasing lung toxicity[37]. In current practice, SABR for medically inoperable NSCLC as well as lung metastases has become the standard of care[37].

Challenges have been described in the literature in terms of standardizing the fractionation schedule for lung SABR[26]. In 2001, a study of 50 patients was reported with fractionations of 50 Gy to 60 Gy delivered in 5 to 10 fractions, with 94% of these patients achieving long term local control[38]. Furthermore, dose escalation studies have reported that the maximum tolerated dose (MTD) for a total of three fractions was achieved for tumour diameters greater than 5 cm at 24 Gy per fraction, with local control achieved in all but one case that was administered 16 Gy per fraction[39,40]. For standardizing prescription doses and clinical practice in lung SABR, RTOG 0915 guidelines have been recommended[18]. Here, fractionation schedules of 60 Gy in three fractions, 50 Gy in five fractions, 48 Gy in four fractions, and 30 Gy to 34 Gy in one fraction, have been proposed, with the single fraction treatments for "peripheral" lesions, whereas "central" lesions receive a smaller dose per fraction due to a higher risk of severe toxicity to proximal OARs[18,26]. In addition to lung toxicity, there are various thoracic organs that must be considered during SABR of lung. The avoidance of these OARs is prioritized based on their potential for severe and/or irreversible injury and include the spinal cord, esophagus, major airway structures (trachea and proximal bronchial tree/large bronchus), the heart, and lungs. Their dose tolerances will be further discussed in Section 2.4.

In the manuscript of Chapter 5 treatment plans were created using a cohort of 18 patients that were previously treated with lung SABR. The goal of this research was to extend cranial non-coplanar optimization to an extracranial site and show that patient-specific arcs have the capacity to reduce maximum doses to the OARs, while maintaining target conformity and prescription dose.

Another extracranial indication for SABR is the liver, where 66% of all patients diagnosed with primary hepatocellular carcinoma (HCC) are neither suitable for surgical resection nor liver transplantation[41]. The main concern of using radiotherapy to treat liver tumours concerns the risk of radiation-induced liver disease (RILD), where the risk is directly proportional to the mean radiation dose received by the liver[42,43]. Therefore, it is reasonable to consider the liver like the lung as parallel in its biological functionality[42,43]. Due to the highly conformal dose distributions used in SABR there is potential to spare functional liver while maintaining the high doses required to ablate disease. SABR has shown promising results in treating liver metastases where progression from oligometastatic disease of colorectal cancer is a prominent indication[44-46]. It is a continuously improving treatment option for non-surgical patients that has the potential to compete with and/or complement minimally invasive procedures such as radio frequency ablation (RFA), trans-arterial chemoembolization (TACE), and trans-arterial radioembolization (TARE)[41].

In multiple early-phase prospective clinical trials, various fractionation schedules have been proposed with prescription doses ranging from 15 Gy to 60 Gy delivered in one to six fractions for treatment of primary HCC[47-51]. Various rates of 1-, 2-, and 3-year local control and overall survival have been reported with noteworthy improvements upon examining the literature longitudinally. The most promising from 2016 shows 3-year primary local control of 96.3% with corresponding overall survival of 66.7% using SABR delivering 35 Gy to 40 Gy in five fractions with optional TACE[51]. Similar overall survival at 18 months was seen using SABR for liver metastases in a single fraction dose escalation study comparing the 22 Gy to 26 Gy arm to the 14 Gy to 20 Gy arm[44].

Standardizing prescription doses in liver SABR is less rigorously defined than lung SABR, in part due to the dependence of the target volume size on the allowable mean liver dose (MLD). The RTOG 1112 provides guidelines where prescription dose depends on MLD at a maximum of five fractions. The maximum acceptable MLD is 13 Gy which allows for an upper limit on the prescription dose of 50 Gy. If the prescription dose causes MLD to be exceeded, the prescription can be reduced to 45 Gy and re-evaluated[17]. In contrast, the maximum MLD of 17 Gy should be combined with prescription dose of 27.5 Gy in five fractions, where exceeding the MLD renders the patient ineligible for treatment. Liver toxicity is predicted by MLD and dose to 700 cc[17], however treatments are also limited by the proximity of target volumes to adjacent gastrointestinal structures such as the duodenum, stomach, and bowel. Dose tolerances to these OARs will be discussed further in section 2.4. In cases where these structures are not adjacent, RTOG 1112 recommends the upper limit of the PTV dose prescription limited only by MLD[17].

In the manuscript of Chapter 6, treatment plans were created on a cohort of 16 patients that were previously treated with liver SABR. The goal of this research was to incorporate biological considerations into choosing optimized patient specific non-coplanar arcs that have the potential to reduce maximum dose to GI structures and reduce MLD while ensuring clinically acceptable target conformity and prescription dose.

SABR has been proposed for other sites such as spinal tumors, bone, abdominal lesions, primary prostate cancer, renal cell carcinoma, and head and neck cancer. As these indications were not the primary focus, a high-level discussion on how to apply the non-coplanar arc optimizations of this thesis, will be examined in the "Future Works" section of Chapter 7.

2.4 OAR Dose Tolerances

In the previous section prescription doses for adequate treatment of disease in the three anatomical sites considered in this dissertation were discussed. In this section the dose tolerances of the OARs used in SABR will be discussed in terms of the recently published (2021) Hypofractionated Treatment Effects in the Clinic (HyTEC) series[52].

The HyTEC series is the third installment of literature reviews that estimate dose, volume, and outcome data in radiotherapy. It is distinguished from its predecessors, the Quantitative Analyses of Normal Tissue Effects in the Clinic (QUANTEC)[53] and joint publications of Emami *et al.*[54] and Burman *et al.*[55], where only conventional fractionated schedules were used. As discussed in section 2.2 the LQ model theoretically predicts and is validated experimentally up to 10 Gy per fraction. The goal of the HyTEC series was to systematically pool published peer-reviewed clinical data using in a useful format to assess models for TCP and normal tissue complication probability (NTCP) in terms of SABR.

The scope of the earliest publications by Emami *et al.*[54,55] considered 26 OARs citing uniform levels of risk quantified by the tolerance dose (TD) that results in a 5% and 50% risk of toxicity 5 years post irradiation (TD 5/5 and TD50/5). These risks were based on uniform irradiation of 1/3, 2/3 and 3/3 of the OAR volume. The scope of QUANTEC considered 16 OARs with nonuniform levels of risk cited across organs. These risks were attributed specific dose-volume metrics[53]. The scope of HyTEC considered 9 OARs with nonuniform levels of risk across organs for a range of dose-volume metrics[52].

In each manuscript for the thesis, RTOG guidelines were followed that cite relevant dose tolerances and clinical endpoints. We restrict metrics to the fractionations used in this research, therefore single fraction metrics are included for the single fraction cranial cases, four fraction metrics for the lung cases, and five fraction metrics for the liver cases. These are summarized in the following tables strictly for the OARs considered in this dissertation. Notably, the liver cases had differing prescription doses which inherently causes the MLD constraint to vary and these are represented in ranges below. If a constraint was not found for a specific OAR in the HyTEC overview, the QUANTEC overview was consulted for a constraint. If a constraint was not found in either HyTEC or QUANTEC, overview the Emami data was provided.

Table 2.1: Normal tissue constraints and associated normal tissue complication probabilities from Emami *et al.*[54,55], QUANTEC[53], and HyTEC[52] reviews compared to RTOG9005 guidelines used for the cranial SRS treatment planning of Chapter 4. The prescription dose was 24 Gy delivered in one fraction.

Organ-at-risk (OAR)	**Constraint: Endpoint, Reference** (HyTEC (**H**), QUANTEC (**Q**), Emami (**E**))	**RTOG 9005**
Brain	-$V_{12Gy} \leq 5$ cc: Necrosis (10%) **H** -$V_{12Gy} \leq 10$ cc: Necrosis (15%) **H** -$V_{12Gy} \leq 15$ cc: Necrosis (20%) **H**	-$V_{12Gy} \leq 10$ cc
Brainstem	-$D_{max} < 12.5$ Gy: Permanent cranial neuropathy / Necrosis (< 5%) **Q**	-$D_{max} < 12.5$ Gy
Optic Chiasm	-$D_{max} < 10 – 12$ Gy: Neuropathy (<1%) **H**	-$D_{max} < 10$ Gy -$D_{0.2cc} < 8$ Gy
Eyes	-TD5/5 Volume 3/3 ≤ 45 Gy: Blindness (5%), **E** -TD50/5 Volume 3/3 < 65 Gy: Blindness (50%), **E**	-$D_{max} < 10$ Gy
Lenses	-TD5/5 Volume 3/3 ≤ 10 Gy: Cataract requiring intervention (5%), **E** -TD50/5 Volume 3/3 ≤ 18 Gy: Cataract requiring intervention (50%), **E**	-$D_{max} < 10$ Gy
Optic Nerves	-$D_{max} < 10 – 12$ Gy: Neuropathy (<1%) **H**	-$D_{max} < 12$ Gy - $D_{0.2cc} < 8$ Gy

Table 2.2: Normal tissue constraints and associated normal tissue complication probabilities from Emami *et al.*[54,55], QUANTEC[53], and HyTEC[52] reviews compared to RTOG0915 guidelines used for the lung SABR treatment planning of Chapter 5. The prescription dose was 48 Gy delivered in four fractions.

Organ-at-risk (OAR)	**Constraint: Endpoint, Reference** (HyTEC (**H**), QUANTEC (**Q**), Emami (**E**))	RTOG 0915
Ipsilateral Lung	-$V_{20Gy} < 10$-15%: Grade ≥ 2 Toxicity (10-15%) **H** -$D_{mean} \leq 8$ Gy: Grade ≥ 2 Toxicity (10-15%) **H**	-$V_{11.6Gy} < 1500$ cc -$V_{12.4Gy} < 1000$ cc -$V_{20Gy} \leq 10\%$ -$D_{mean} \leq 6$ Gy
Contralateral Lung	-$V_{20Gy} < 10$-15%: Grade ≥ 2 Toxicity (10-15%) **H** -$D_{mean} \leq 8$ Gy: Grade ≥ 2 Toxicity (10-15%) **H**	-$V_{11.6Gy} < 1500$ cc -$V_{12.4Gy} < 1000$ cc -$V_{20Gy} \leq 10\%$ -$D_{mean} \leq 6$ Gy
Aorta	Not contained in HyTEC, QUANTEC, or Emami	-$D_{max} < 49$ Gy -$D_{10cc} < 43$ Gy
Esophagus	-$D_{mean} < 34$ Gy: Grade ≥ 3 acute esophagitis (5-20%) **Q** -$V_{35} < 50\%$: Grade ≥ 2 acute esophagitis (<30%) **Q** -$V_{50} < 40\%$: Grade ≥ 2 acute esophagitis (<30%) **Q** -$V_{70} < 20\%$: Grade ≥ 2 acute esophagitis (<30%) **Q**	-$D_{max} < 30$ Gy -$D_{5cc} < 18.8$ Gy
Heart	-$D_{mean} < 26$ Gy: Pericarditis (<15%) **Q** -$V_{30Gy} < 46\%$: Pericarditis (<15%) **Q** -$V_{25Gy} < 10\%$: Long-term cardiac mortality (<1%) **Q**	-$D_{max} < 34$ Gy -$D_{15cc} < 28$ Gy
Proximal Bronchial Tree / Large Bronchus	Not contained in HyTEC, QUANTEC, or Emami	-$D_{max} < 34.8$ Gy -$D_{4cc} < 15.6$ Gy
Spinal Cord	-$D_{max} < 23$-26.2 Gy: Myelopathy (1-5%) **H**	-$D_{max} < 26$ Gy - $D_{0.35cc} < 20.8$ Gy - $D_{1.2cc} < 13.6$ Gy
Trachea	Not contained in HyTEC, QUANTEC, or Emami	-$D_{max} < 34.8$ Gy -$D_{4cc} < 15.6$ Gy

Table 2.3: Normal tissue constraints and associated normal tissue complication probabilities from Emami *et al.*[54,55], QUANTEC[53], and HyTEC[52] reviews compared to RTOG1112 guidelines used for the liver SABR treatment planning of Chapter 6. The prescription doses varied between 27.5 and 54 Gy delivered in five fractions.

Organ-at-risk (OAR)	**Constraint: Endpoint, Reference** (HyTEC (**H**), QUANTEC (**Q**), Emami (**E**))	RTOG 1112
Liver - GTV	-$V_{15\text{-}17Gy} < 700$ cc: Liver dysfunction and Grade 3 – 5 general GI toxicity (<13%) **H** -$D_{mean} \leq 18$ Gy: Grade ≥ 3 enzyme change (<20%) **H**	-$D_{mean} \leq$ (13-17) Gy -$V_{eff} \leq$ (25 – 64) % -$V_{10Gy} < 70\%$ -$V_{18Gy} < 700$ cc (metastases) -$V_{21Gy} < 700$ cc (HCC)
Duodenum	Not contained in HyTEC, QUANTEC, or Emami	-$D_{max} < 30$ Gy -$D_{5cc} < 25$ Gy
Heart	-$D_{mean} < 26$ Gy: Pericarditis (<15%) **Q** -$V_{30Gy} < 46\%$: Pericarditis (<15%) **Q** -$V_{25Gy} < 10\%$: Long-term cardiac mortality (<1%) **Q**	-$D_{30cc} < 30$ Gy
Kidneys	-$D_{mean} <$ 15-18 Gy: Clinically relevant dysfunction (< 5%) **Q** -$D_{mean} < 28$ Gy: Clinically relevant dysfunction (<50%) **Q**	-$D_{mean} < 10$ Gy -$V_{10Gy} < 10\%$ (if $D_{mean} > 10$ Gy, opposing Kidney)
Spinal Cord	-$D_{max} <$ 23-26.2 Gy: Myelopathy (1-5%) **H**	-$D_{max} < 34.8$ Gy -$D_{4cc} < 15.6$ Gy
Stomach	-$D_{100\%} < 45$ Gy: Ulceration (< 7%) **Q**	-$D_{max} < 30$ Gy -$D_{5cc} < 25$ Gy

All these dose constraints have important clinical significance in terms of the endpoints that they represent. Of note throughout the tables presented is that there is limited data from SABR treatment planning techniques in the QUANTEC series and Emami papers, which was the initial motivation for the HyTEC series. However, as RTOG reports and reviews like these occur in parallel, it provides the opportunity for continued collaboration to establish best practices in the field. HyTEC provides recommendations for data pooling to ensure best practices for dose tolerance can be ensured which has the potential for improved comparisons on the longitudinal effects of SABR techniques[52].

2.5 Delivery Methods

This section examines different types of mechanical delivery systems for radiotherapy and their suitability for non-coplanar optimizations.

2.5.1 CyberKnife

CyberKnife® by vendor Accuray Medical Systems (Accuray Inc., Sunnyvale CA) is an X-band LINAC operating at approximately 9.3 GHz. The defining feature of the CyberKnife system is the LINAC mounted to a robotic arm, enabling it to move freely with six dimensions of freedom (6Dof). Image guidance is performed by means of two stereoscopic kilovoltage (kV) x-ray sources mounted to the ceiling, whose corresponding detectors are beneath the floor. CyberKnife can deliver precise radiotherapy, specifically intracranial and extracranial SABR using cones or MLC. The most recent version of the CyberKnife system is shown in Figure 2.1:

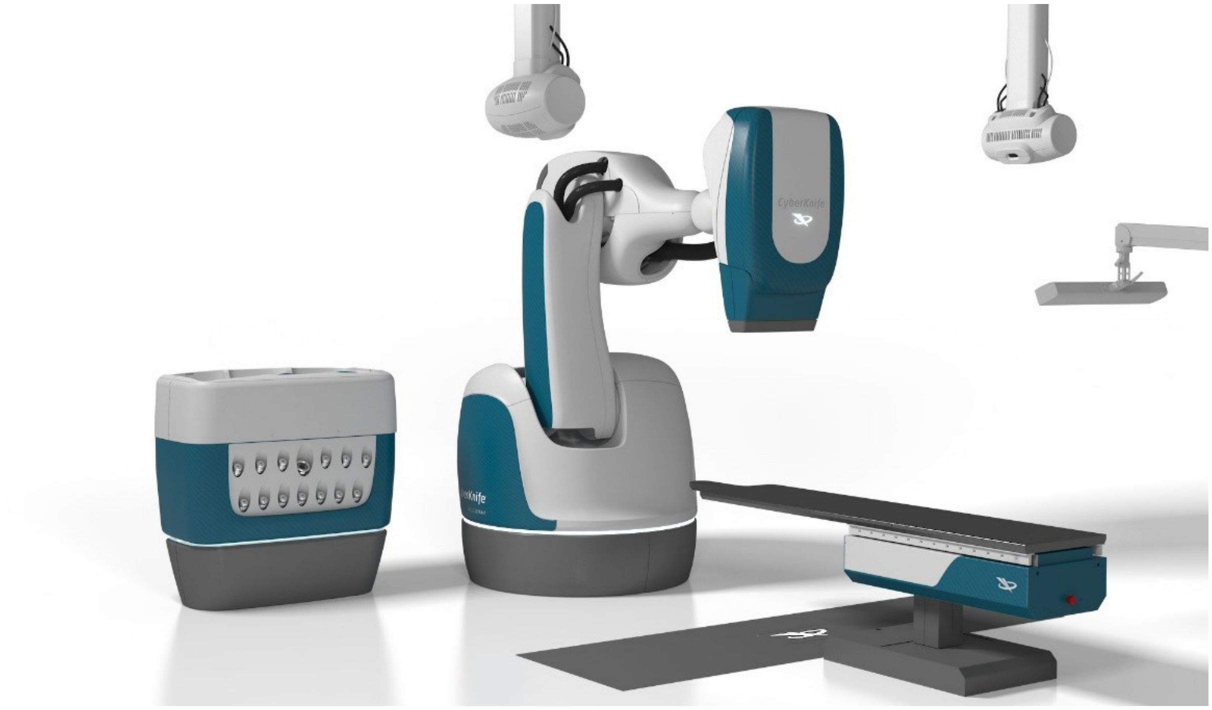

Figure 2.1: The CyberKnife® M7 system by Accuray (Accuray Inc. Sunnyvale, CA). Image publicly accessible from: *https://www.accuray.com/cyberknife/.* Date accessed: June 2023.

CyberKnife deliveries typically use non-coplanar, non-isocentric, intensity modulated fields to deliver precise radiation doses to the PTV. Due to the large degrees of freedom CyberKnife appears a suitable candidate for sampling 4π space[56,57]. However, there are mechanical limitations that must be overcome such as the inability to deliver posterior beams, as well as clinical limitations where treatments on the order of one hour have been observed due to the IMRT port-like delivery[56]. The ability to perform arc therapy with CyberKnife may alleviate some of these efficiency discrepancies, however the vendor must provide this functionality so it can be tested.

2.5.2 Gamma Knife

The Gamma Knife® radiosurgery system (Elekta AB, Stockholm, Sweden) builds on early work by Lars Leksell that was discussed in Section 2.1. Exclusively for cranial indications, this system is not a linear accelerator and instead houses Co-60 sources with spherical apertures that can be opened or closed to shape dose distributions. Its sources have an average energy of 1.25 MeV and a half life of 5.26 years[58]. Figure 2.2 shows a recent version of Elekta's Gamma Knife Icon ®.

Figure 2.2: The Gamma Knife Icon ® system by Elekta Oncology Solutions (Elekta AB, Stockholm, Sweden). Image publicly accessible from: https://www.elekta.com/products/stereotactic-radiosurgery/#sec-icon. Date accessed: June 2023.

Non-coplanar optimizations by means of couch and gantry rotation are not feasible for the Gamma Knife system as its couch does not rotate. However, geometric optimizations are possible due the positions of the sources inside the Gamma Knife's helmet that inherently samples 4π space.

2.5.3 Tomotherapy

The Tomotherapy ® system by Accuray is a closed bore LINAC housed on a slip ring like a CT scanner that has the capacity of delivering SABR doses. Its 3.6 MV beam spectrum provides the ability for imaging and treatment. The ring gantry allows for helical delivery where there is continuous couch translation during rotational delivery to produce a helical pattern. It has the capacity to deliver a standard IMRT delivery at a fixed gantry position while the couch translates in the superior-inferior direction. Tomotherapy ® uses MLC that perform binary collimation to perform intensity modulation as the couch translates. Modifications of Tomotherapy ® have included additions of kV imaging and a high-speed MLC to create the Radixact ® system shown in Figure 2.3.

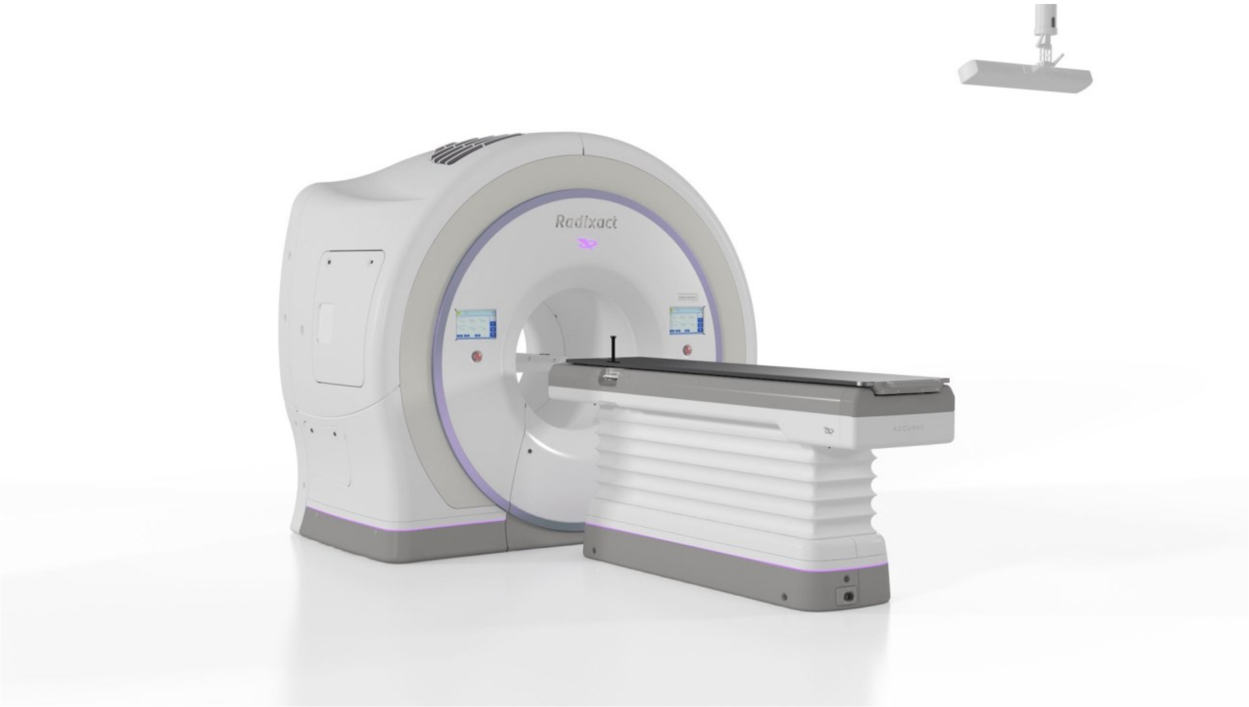

Figure 2.3: The Radixact® system by Accuray. (Accuray Inc., Sunnyvale CA). Image publicly accessible from: https://www.accuray.com/radixact/. Date accessed: June 2023.

Simulated non-coplanar optimizations have been investigated with oblique arcs created for helical delivery using Tomotherapy to encourage hardware modifications that permit couch rotation.[59,60]. Due to similarities in delivery efficiency with IMRT, treatment time is a limiting factor to the implementation of these technologies.

2.5.4 Halcyon/Ethos

A new product within the previous five years, Halcyon® (Varian Medical Systems, Palo Alto CA) was introduced as the vendor's first O ring gantry system, thereby enabling fast rotational delivery of radiation. Unlike Tomotherapy®, Halcyon ® can deliver VMAT with the RapidArc technology (Varian Medical Systems, Palo Alto CA) that is available on current C-arm LINACs. These arc deliveries occur at 2 rpm, and thus maintain comparable or improved delivery efficiency to current treatments. Varian has also added adaptive planning and improved image guidance to Halcyon® in their new Ethos® product (Varian Medical Systems, Palo Alto CA). Figure 2.4 shows the Ethos® system.

Figure 2.4: The Ethos® system by Varian (Varian Medial Systems, Palo Alto CA). Image publicly accessible from https://www.varian.com/products/radiotherapy/treatment-delivery/hypersight. Date accessed: June 2023.

No studies have been performed concerning its ability to perform non-coplanar optimizations. There is limited movement of the couch which could imply this hardware may not benefit from the optimizations in this dissertation.

2.5.5 C-Arm LINAC

Most cancer centres delivering radiotherapy throughout the world make use of the C-arm linear accelerator (LINAC).

Medical linear accelerators are machines that can generate high-energy (megavoltage, MV) x-ray spectra. These x-rays are created when the machine accelerates electrons to relativistic speeds and impinges them on a target material. The resulting interactions produce a spectrum of Bremsstrahlung photons which are then shaped through a series of collimation steps before they are made incident on a patient. The type of C-arm LINAC used throughout this dissertation is a Varian TrueBeam STx (Varian Medical Systems, Palo Alto CA) at Nova Scotia Health. A schematic diagram of this type of LINAC reproduced from Podgorsak[8] is shown in Figure 2.5.

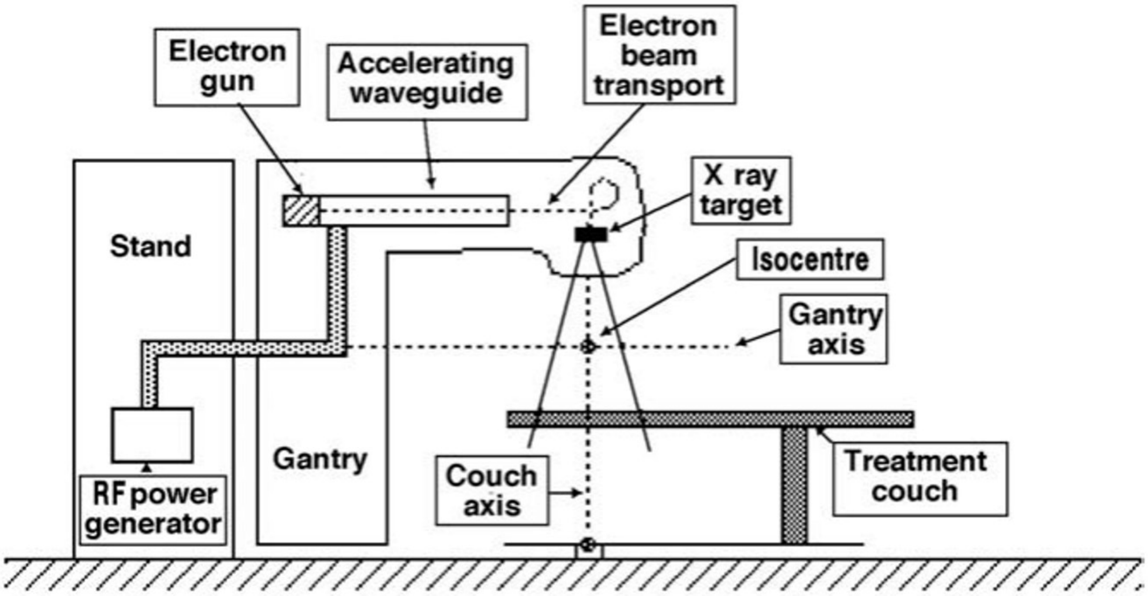

Figure 2.5: Schematic of an S-band LINAC[8].

The RF power generator is housed in the stand and operates at 2856 MHz (S-band). This gives sufficient power to accelerate the electrons generated in the gantry's electron gun towards the accelerating waveguide. The waveguide accelerates the narrowed beam of electrons through a 270° bending magnet towards a tungsten ($Z = 74$) target. The beam collimation system occurs after electrons hit the X-ray target. With increasing distance from the target, the collimation system includes primary collimation, secondary collimation jaws (upper and lower), and the MLC. Collimators are also made of tungsten to ensure that photons are absorbed within the material. Removal of the flattening filter before the beam collimation system produces flattening filter free (FFF) beams that are used to increase the dose rate of the machine. An example of Varian's TrueBeam STx system (Varian Medical Systems, Palo Alto CA) is shown in Figure 2.6. This LINAC is equipped with high definition (HD) MLC for precise beam shaping.

Figure 2.6: Novalis Certified TrueBeam STx® system from Varian Medical Systems (Varian Medical Systems, Palo Alto CA) with Brainlab 6 DoF couch and Exactrac® stereoscopic imaging (Brainlab AG, Germany). Image publicly accessible from https://www.surgicalroboticstechnology.com/page2/. Date accessed: June 2023.

2.6 Plan Delivery Methods with C-Arm LINACs

Building on the last section, this section will focus on the plan delivery methods used in this dissertation. Although all manuscripts performed VMAT treatment planning as per institutional standard of practice, there is precedence for discussing 3D-CRT, DCA, and IMRT in the context of non-coplanar optimizations to understand where benefits can be realized.

2.6.1 3D Conformal Radiotherapy (3D-CRT) and Dynamic Conformal Arcs (DCA)

In three-dimensional conformal radiotherapy (3D-CRT) the CT images of the patient are used to delineate PTV and OARs. In this way, the MLC can be collimated specifically to the PTV with a margin to account for beam penumbra, so excess radiation dose is not delivered to surrounding OARs. The PTV is then treated with one radiation field from each distinct beam direction in the plan. In this methodology, the shape of the radiation field is a projection of the PTV in the radiation BEV[3]. Forward dose calculations do not modulate fluence throughout the BEV. When PTV and OARs overlap, collimating to the PTV will not limit radiation dose through the overlapping OAR regions in the BEV. When the PTV exhibits concavities 3D-CRT will irradiate the entire uncollimated area. This makes 3D-CRT more suitable for round or convex shapes to achieve a conformal dose distribution to the target. Meyer *et al.* proposed a method for selecting optimized non-coplanar beam directions for 3D-CRT using raytracing[61].

Dynamic conformal arcs (DCA) are a special case of 3D-CRT where the MLC are sequenced to conform to the target at successive control points (CP) along a single arc or multiple arcs. Control points can be defined as the machine states that define positional locations of hardware axes. Like 3D-CRT, the dose distribution is not modulated with MLC throughout treatment, thus OAR sparing is imperative by means of collimating to the PTV as much as possible in the absence of overlapping regions.

2.6.2 Intensity Modulated Radiotherapy (IMRT) and Inverse Optimization.

The primary focus of intensity modulated radiotherapy (IMRT) is extending 3D-CRT to deliver non-uniform fluence to create an inverse optimized plan. This fluence modulation allows for radiation dose to be concentrated at a specific geometric location in the field and minimized at other specific geometric locations in the same field.

The IMRT planning procedure can thus be formulated as an optimization problem:

1. A prescribed dose (R_x) should be delivered to all parts of the PTV.
2. The resulting dose distribution should conform to the PTV with a steep dose fall off outside to avoid any surrounding OARs.
3. Dose to specific OARs proximal to the PTV must be minimized.
4. Dose to specific OARs cannot exceed a specific tolerance dose.

An objective for the prescription dose can be summarized mathematically according to Equation 2.3as the sum of squared difference:

$$O(d) = \frac{1}{N}\sum_{i=1}^{N}\left(d_i - R_{i,x}\right)^2 \tag{2.3}$$

where the objective O as a function of the dose d is dependent on the number of voxels N that are receiving the prescription dose R_x. For any voxel whose dose deviates from the R_x the objective value increases by the average of the quadratic deviation. In this case, higher objective function scores indicate worsening plan quality[3].

Multiple objective functions can be created based on the objective that a planner wants to achieve.

Dose constraints can be formulated mathematically according to Equations 2.4A & 2.4B:

$$d_i \leq d_S^{Max}, i \in S \tag{2.4A}$$

$$d_Y \leq d_S^x, i \in S_x \tag{2.4B}$$

Where the dose at any voxel d_i cannot exceed a maximum dose (d_{max}) to the structure S for all voxels i in S (maximum dose constraint of equation 2.4A). Similarly, for a dose volume constraint illustrated by equation 2.4B where dose to x cc of a structure S cannot exceed Y Gy.

Treatment plans are optimized by minimizing the weighted sum of objectives, and can be done in a variety of ways[3]. Fluence map optimization and direct aperture optimization (DAO)that satisfy the pre-determined objectives and constraints of the treatment plan are examples of inverse-planning or inverse optimization. These optimizations yield the final treatment plan for delivery with optimized dose rate and MLC positions at each control point that ensure the total objective function was minimized. It is important to note that there can be conflicting objectives and constraints in treatment planning where not everything that is requested can be met.

Non-coplanar IMRT based on cost map analysis was proposed by Yang *et al.*[62] and investigated explicitly for lung[22] and liver[23] SBRT by Dong *et al*. who found statistically significant dose reductions to OARs with a large number of IMRT fields compared to coplanar(VMAT).

2.6.3 VMAT and Inverse Optimization

Although IMRT is widely used for delivering complex radiation fields, it can be clinically cumbersome for many fields that requires manual rotation of the treatment gantry and couch to the specific field geometry. It is our institutional practice that image guidance should be performed whenever the treatment couch is moved as the patient position may have changed.

Volumetric modulated arc therapy (VMAT) proposed delivering IMRT in a single gantry arc[4]. In arc therapy the beam stays on continuously while the gantry of the LINAC rotates.

VMAT extends IMRT to a rotational treatment that is deliverable with a C-arm LINAC. Like IMRT, VMAT treatment fields do not have to conform to the target as in DCA, instead MLC sequencing occurs over an arc. Delivering from all gantry angles compared to a small number of discrete angles has the potential to better conform the prescription isodose to the target volume. There are significant efficiency gains possible using VMAT as the treatment beam is on for the entire arc, such as reduction in total number of monitor units and reduction in delivery time[4].

The VMAT treatment planning process diverges from traditional IMRT, and thus the dose distribution of a VMAT plan depends on three variables:

1. The MLC, where Bank 1 and Bank 2 positions vary as a function of time.
2. The gantry angle varies as a function of time.
3. The dose rate varies as a function of time.

In practice, jaw positions, collimator angles, and couch angles can also vary as a function of time, however the discussion here is limited to the three variables above. A high quality VMAT plan can be defined as having the best conformity, lowest dose to OARs, and most rapid dose fall off. To achieve these types of VMAT plans that are also delivered efficiently implies that considerations must be made for the mechanical limitations of the LINAC, such as dose rate, gantry angular velocity, and MLC speed. In most cases efficiency is prioritized by means of the maximum dose rate and gantry speed, while MLC are sequenced to optimize apertures based on fluence[4].

Otto suggested DAO using simulated annealing[63] with geometry-based initialization of aperture shapes for VMAT. The essence of this dissertation is to optimize the BEV of these apertures by including non-coplanar perspectives to improve VMAT treatment plan quality and efficiency.

2.7 Dose Calculation

For all treatment plans, the plan delivery methods discussed in Section 2.6 optimize all geometries from which the radiation beam will be delivered to encourage meeting the optimization criteria. Once these have been determined, dose is calculated at every iteration of the planning optimization to calculate the objective function. Dose is calculated on the patient's planning CT that contains Hounsfield Units (HU) which represent attenuation. HU are then related to electron density information at every voxel in cartesian space $\rho_e(X,Y,Z)$ through calibration curves. Knowing these differing electron densities allows us to understand how primary and scattered radiation will interact during the patient's treatment. Dose calculation software is rigorously developed, tested, and regulated across the world. Treatment planning software from various commercial vendors provide similar methods, however the work in this thesis was limited to two dose calculation algorithms implemented in the Varian Eclipse treatment planning system (TPS) (Varian Medical Systems, Palo Alto CA). The first manuscript uses the Anisotropic Analytical Algorithm[64,65] implemented in Eclipse version 13.6, while the second and third manuscripts use the Acuros XB Algorithm[66,67] implemented in Eclipse version 15.6. We moved to Acuros once it became available in our clinic, and this was reflected in comparisons to clinical treatment planning procedures throughout the dissertation. This section contains a brief explanation of both algorithms exclusively for photons.

2.7.1 Anisotropic Analytical Algorithm (AAA)

AAA is classified as a pencil beam convolution/superposition that reduces computational time using physical exponential expressions for lateral dose deposition. It makes use of Monte Carlo derived phase spaces which account for radiation interactions from the target to the exit window of the LINAC. These phase spaces thus comprise primary and scatter photons, as well as scatter electrons that are generated. To propagate the phase space onto the patient, beams are divided into smaller beams (beamlets) along a voxelated grid of predetermined size defined at isocenter. The energy from each of these is then calculated using a 3D convolution superposition determined by Equation 2.3:

$$E_\beta\left(\tilde{X},\tilde{Y},\tilde{Z}\right) = \Phi_\beta \times I_\beta(z,\rho) \times \mathrm{K}_\beta(X,Y,Z) \tag{2.3}$$

In this equation, E is the energy of a beamlet β calculated at point in cartesian space relative to the beamlet's coordinate system (*X, Y, Z*), while Φ_{B} is the fluence of the beamlet. I_β is the energy deposition function that accounts for tissue heterogeneities by scaling the dose based on radiological depth z. K_{B} is the photon scatter kernel, an analytical model described further below.

$$I_\beta(z) = \iint h_\beta(t,v,z)dt\, dv \tag{2.4}$$

and Equation 2.4 demonstrates the depth dependence (*z*) of the energy deposition function where h_β is the poly-energetic pencil beam generated using Monte Carlo.

The first step in radiological scaling is to normalize the energy deposition function by that of water (Equation 2.5). Therefore, any radiological depth will be known based on this density ratio to water.

$$I_\beta = I_\beta(z') * \frac{\rho(x,y,z)}{\rho_{water}} \tag{2.5}$$

here, z' is the radiologically scaled depth and ρ is the electron density at that depth.

The photon scatter kernel is described by K_β and is comprised of six analytical exponential functions:

$$K_\beta(x,y,z) = \sum_{k=0}^{5} \frac{c_k(z')}{r} e^{-\mu_k r} \tag{2.6}$$

These exponential scatter kernels are each characterized by their attenuations μ_k, while c_k are fitting parameters based on least square fitting to the basis exponential function to the scatter kernels developed using Monte Carlo and vary in logarithmic intervals between 1 and 100 mm [64,65].

In each case, Equation 2.6 must be modified by the density scaling factor of Equation 2.5 and yields a scaled version of k_z which is convolved (⊗) with the beamlet energy to give the final energy.

$$E'_\beta(x,y,z) = E_\beta(x,y,z) \otimes k_z(z) \tag{2.7}$$

The final superposition step involves summing the contributions of primary and secondary photons with contaminant electrons to give a total energy for each beamlet. This energy in Joules (J) is converted to dose in Gy (J/kg) scaling by electron densities.

2.7.2 Acuros External Beam Algorithm (AXB)

The AXB Algorithm differs from the AAA by considering the significant effects that tissue heterogeneities may have on dose calculation especially in small or irregularly shaped fields.

This algorithm solves the linear Boltzmann transport equations (LBTE) directly, thus accounting for heterogeneities.

The overview of the dose calculation's steps are as follows:

1. Create the physical material map (from simulation 3D imaging)
2. Transport the components of the photon beam source model into the patient (Monte Carlo).
3. Transport the scattered photons and electrons in the patient.
4. Calculate the desired dose (dose to specific medium, or dose to water).

Given a spatial volume, the Acuros XB algorithm solves the time independent 3D system of coupled LBTE [66,67]:

$$\hat{\Omega}\vec{\nabla}\Psi^{\gamma} + \sigma_t^{\gamma}\Psi^{\gamma} = q^{\gamma\gamma} + q^{\gamma} \tag{2.8}$$

$$\hat{\Omega} \cdot \vec{\nabla}\Psi^{e} + \sigma_t^{e}\Psi^{e} - \frac{\partial}{\partial E}(S\Psi^{e}) = q^{ee} + q^{\gamma e} + q^{e} \tag{2.9}$$

In these equations the superscripts e and γ denote electron and photon fluence respectively, Ψ denotes angular fluence, while σ symbolizes the cross-section, and S is the total stopping power. The parameter q denotes the various types of scattering that can occur between photons and electrons individually or together. Each equation has directionality given in spherical coordinates by $\hat{\Omega}$ and are subject to physical constraints that the solution must spatially remain within the volume, angular fluence must not exceed 4π, and energy cannot be negative.

Equations 2.8 and 2.9 must be solved numerically for the angular electron fluence Ψ^e and are done so through many spatial and angular discretization steps, with applications of scattering models. Dose is dependent on this parameter and can then be calculated according to:

$$D_i = \int_0^\infty dE \int_{4\pi} d\widehat{\Omega}\, \frac{\sigma_{ED}^e(\vec{r}, E)}{\rho(\vec{r})} \Psi^e(\vec{r}, E, \widehat{\Omega}) \tag{2.10}$$

where dose is also dependent on the electron density deposition cross section σ_{ED}^e, and the electron density ρ.

3 Chapter 3: 4π Theoretical Considerations and Algorithms

In this chapter methodologies and algorithms that were considered to implement 4π optimizations in this dissertation are presented.

3.1 4π Delivery Space

The delivery space for radiotherapy in the absence of hardware limitations has been referred to as 4π space, or simply 4π. It is the colloquial term used to describe the three-dimensional (3D) total geometrical area available for delivery of external beam radiotherapy in an idealized scenario. The term was first coined in 2013 by Dong *et al.*[22,23] from the research group at UCLA, and refers to the total area captured by sweeping through all solid angles subtended when the gantry of a linear accelerator completes a full rotation of 360° (2π) for every possible angle of a treatment couch in an orthogonal plane, that can theoretically also complete a full rotation of 360° (2π). Solid angle measured in steradians (Sr) can be found from Equation 3.1.

$$\Omega = \frac{A}{r^2}\ [Sr] \tag{3.1}$$

where Ω is the solid angle, *A* is the surface area of the spherical space, and *r* is the radius of the sphere. We see readily from Equation 3.1 that the total subtended solid angle on a sphere is equal to 4π. This occurs when the surface area of the spherical space is equal to the surface area of the sphere ($4\pi r^2$)[22,23].

In practice, medical linear accelerators (LINACs) such as the C-arm type used by Dong *et al.*[22,23] have physical limitations on axis motion, specifically the treatment couch can only complete a 180° (π) rotation and the gantry rotation plane intersects with half the rotation plane of the couch which causes LINAC collisions. Potential collisions with the patient reduce even further the possible solid angle defined by the couch and gantry combination. Therefore, the solid angle that is physically possible must be less than 4π. This concept has been well understood in trajectory radiotherapy and characterized according to axis limitations of specific machines, but it is also important to note the views of Sarkar *et al.*[68-70]. They argue that the term "4π" should not be used as it is a geometric misnomer since there are no teletherapy units currently available that can deliver from all 4π solid angles without treating along the length of the patient. In this dissertation, we have adopted the notion that delivering from every possible angle in 4π space is a theoretically ideal scenario, but unattainable using current methods. The methods employed aim to increasingly sample the available portion of the total 4π steradian space compared to what is used in current clinical practice.

Non-coplanar optimizations in radiotherapy have become synonymous with 4π radiotherapy in the field of trajectory optimization. In the manuscripts comprising this thesis, these terms have been used interchangeably throughout.

These optimizations typically have three main considerations:

1. Finding a metric that can best describe the available delivery space.
2. Understanding and accounting for the space where delivery cannot physically occur.
3. Navigating the available delivery space (1), subject to the constraints of (2).

Each of these sub-points has the potential to be investigated extensively, however in this research they will each be touched on separately.

Given that 4π describes all solid angles available, metrics are needed to quantify the cost of delivering radiation at a specific geometry.

3.1.1 Structures and Associated BEV Cost

Many non-coplanar optimizations in the literature follow the idea of using anatomical structure contours to create cost metrics. Anatomical structure sets are generated from a patient's computed tomography simulation (CT-sim) and/or magnetic resonance simulation (MR-sim). In current clinical practice, a radiation oncologist, dosimetrist, radiation therapist, or medical physicist uses the 3D images from CT-sim or MR-sim to manually draw anatomical contours for specific organs at risk (OARs). Furthermore, it is current clinical practice for a radiation oncologist to manually draw the contour for gross tumour volume (GTV) or clinical tumour volume (CTV) and add margins to achieve the planning target volume (PTV)[3]. The addition of these margins accounts for uncertainties in planning or treatment delivery[3]. Once all target and avoidance contours have been drawn and peer reviewed, the patient's structure set is complete.

The structure set can then be used to generate cost metrics. Yang *et al.* proposed a cost associated with the amount of overlap between the PTV and OAR in the two-dimensional (2D) beams-eye-view (BEV) for every combination of couch angle (*c*) and gantry angle (g) [62]. This cost equation is summarized in Equation 3.2.

$$E(c,g) = \sum_{i=1}^{n} \frac{L_i(c,g)}{A_t(c,g)} \times \frac{L_i(c,g)}{A_i(c,g)} \tag{3.2}$$

where *E* denotes the cost score in the BEV projected to isocentre, L_i denotes the overlapping area of the i^th OAR (i), A_t is the total area of the target volume, and A_i is the total area of the i^th OAR (i). Summed over a total of *n* OARs, a cost score is calculated as a function of couch and gantry angle, yielding a 2D cost map based on overlap. The assumption for this equation is that each aperture conforms perfectly to the PTV. An example cranial case is shown in Figure 3.1 where the map was normalized by its maximum value.

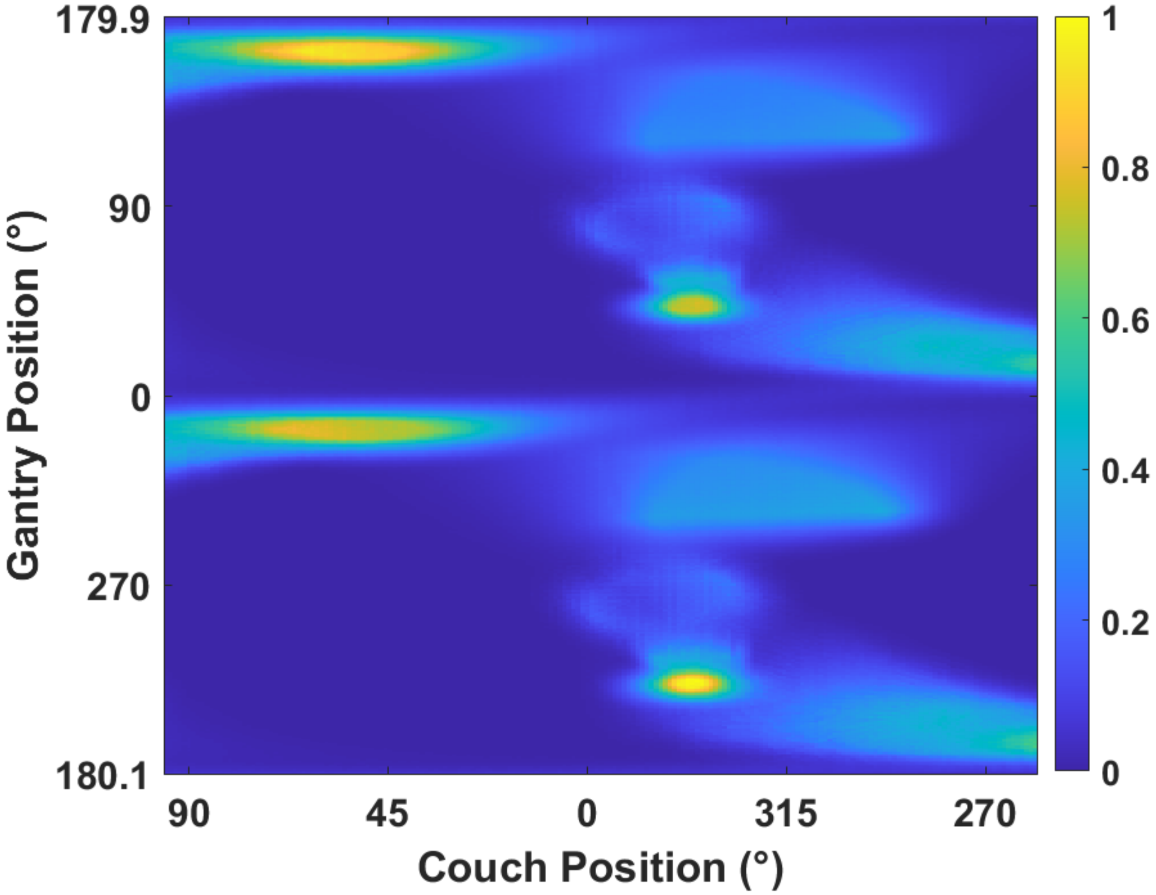

Figure 3.1: An example BEV overlap map (4π map) with corresponding angular positions denoted in IEC 1217 coordinate system[71].

In Figure 3.1 dark blue regions on the map indicate regions of low cost where there the PTV overlaps less with OARs, while brighter regions indicate regions of higher cost where the PTV overlaps more with OARs.

MacDonald *et al.*[29,30] built on this cost equation by incorporating percent depth dose (PDD) information to discern foreground versus background overlap. The rational was to associate greater cost to an angular combination where the PTV is behind an OAR, in which case radiation would have to pass through the OAR to reach the PTV. OAR specific tolerance doses were also incorporated by means of specific weighting factors. Furthermore, another term was added called the "Urgent Sparing Factor (USF)" to limit a specific proximal OAR in the BEV. These factors were evaluated for 16 acoustic neuroma cases by modifying a VMAT arc template to choose couch positions that reduced overlap between cranial OARs and the PTV. They found absolute maximum and mean dose reductions to cranial OARs of approximately 15% and 20%, respectively on average, with improvements in conformity and homogeneity[29]. They concluded that by repositioning the treatment couch based on a cost function analysis that dose reductions were possible for cranial SRT.

As well, various other research groups have used overlap information to inform their BEV cost maps and trajectory optimization[5,11,22-25,29,30,32-35,72,73]. A portion of these results are summarized in the following sections dependent on the type of trajectory optimization.

Instead of measuring areas inside of a BEV projection, some research groups have also performed raytracing to acquire cost information. There have been associations between cost and volume[73], depth[61], and number of rays traced through specific OARs and/or PTV[74-76].

In each of these scenarios, anatomical structure set information has been used to generate a cost associated with delivering radiation at specific angles. Given a specific cost space, trajectory selection is performed by efficiently navigating the space to ensure low-cost solutions are prioritized.

Finally, a significant limitation to fully accessing 4π space is that there are many angles that are physically impossible or undesirable to deliver from. First, there are undeliverable angles in 4π space that cause a collision between the patient, couch, and gantry. There are undesirable geometries that may occur such as delivering through healthy tissue unnecessarily. When these regions are not specified to be treated, it is beneficial to avoid them all together to avoid unwanted radiation toxicity. In most cases, these avoidance regions coincide with collision zones however it is more prevalent in extracranial sites to consider additional avoidance with a patient's arms.

Collision zone optimization is a subset of trajectory optimization that was not the focus of this dissertation. Figure 3.2 shows example collision zones for the same case as Figure 3.1.

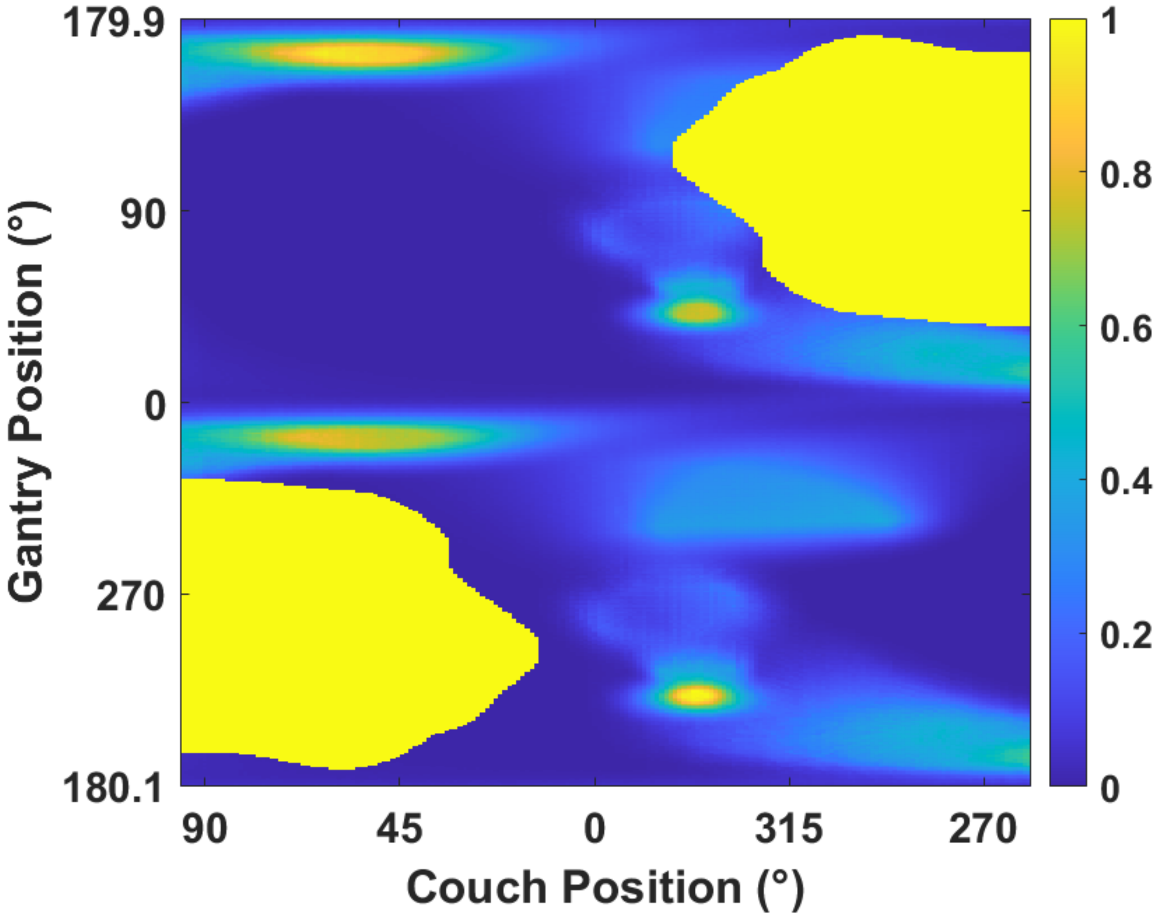

Figure 3.2: The same 4π map as Figure 3.1 with physically measured collision zones added[30].

The manuscripts that comprise this dissertation extend and expand on the methods of MacDonald & Thomas for cranial stereotactic radiosurgery and radiotherapy (SRS) collision zones[30] and modified methods based on Northway *et al.* for extracranial collision zones in lung and liver stereotactic body radiotherapy (SBRT)[77]. In this work, the collision and avoidance zones are always assigned an infinite cost score to ensure that they are avoided when navigating 4π space.

3.1.2 Navigation

Navigating a cost space aims to find a solution that incorporates an optimization of the path through a map of the cost metric. The general problem in mathematics is a subset of graph theory called “The Shortest Path Problem”. In this context, graphs are defined as a series of nodes that are connected by edges. Therefore, the shortest path problem asks the question “what is the shortest path between two nodes in a graph, such that the summed edge weights are minimized?”. There is an added difficulty of not knowing optimized beginning or ending points, nor the optimal path to trace. Sufficient points are required to sample enough to have adequate conformity, while ensuring all these points are low cost and efficient for delivery. In radiotherapy, this is akin to finding a solution that incorporates the minimization of a summed path through a map of a cost metric related to the amount of anatomy inside a BEV for that path.

Each node of the map in Figure 3.2 is a geometric BEV categorized by its unique couch and gantry angle combination, while the edge weights are summed cost values moving from one BEV to another. Infinite cost values are denoted by the bright yellow regions in Figure 3.1, they correspond to the collision zones discussed in Section 3.1.1. The non-infinity cost map values can be normalized to the maximum value, making the quantity unitless, and facilitate comparisons with various pathfinding algorithms.

Minimizing these paths in various ways on the 2D cost map allows for different types of trajectories to be created.

3.1.2.1 Fixed Ports

The most basic minimization of the 2D cost map shown in Figure 3.1 is finding the couch and gantry angle combination that has the least amount of overlap between PTV and OAR. This minimization does not require solving the shortest path problem as the overlap can be catalogued and sorted from smallest to largest. These minimum overlap BEV, are referred to as “fixed ports” as the gantry and treatment couch both remain stationary with the BEV conformal to the target. An example is shown in Figure 3.3 where 20 couch and gantry angle combinations with minimized overlap were plotted to represent choices for potentially deliverable IMRT ports. Further optimization can then be performed by means of fluence modulation via MLC to yield a fixed port IMRT plan.

.

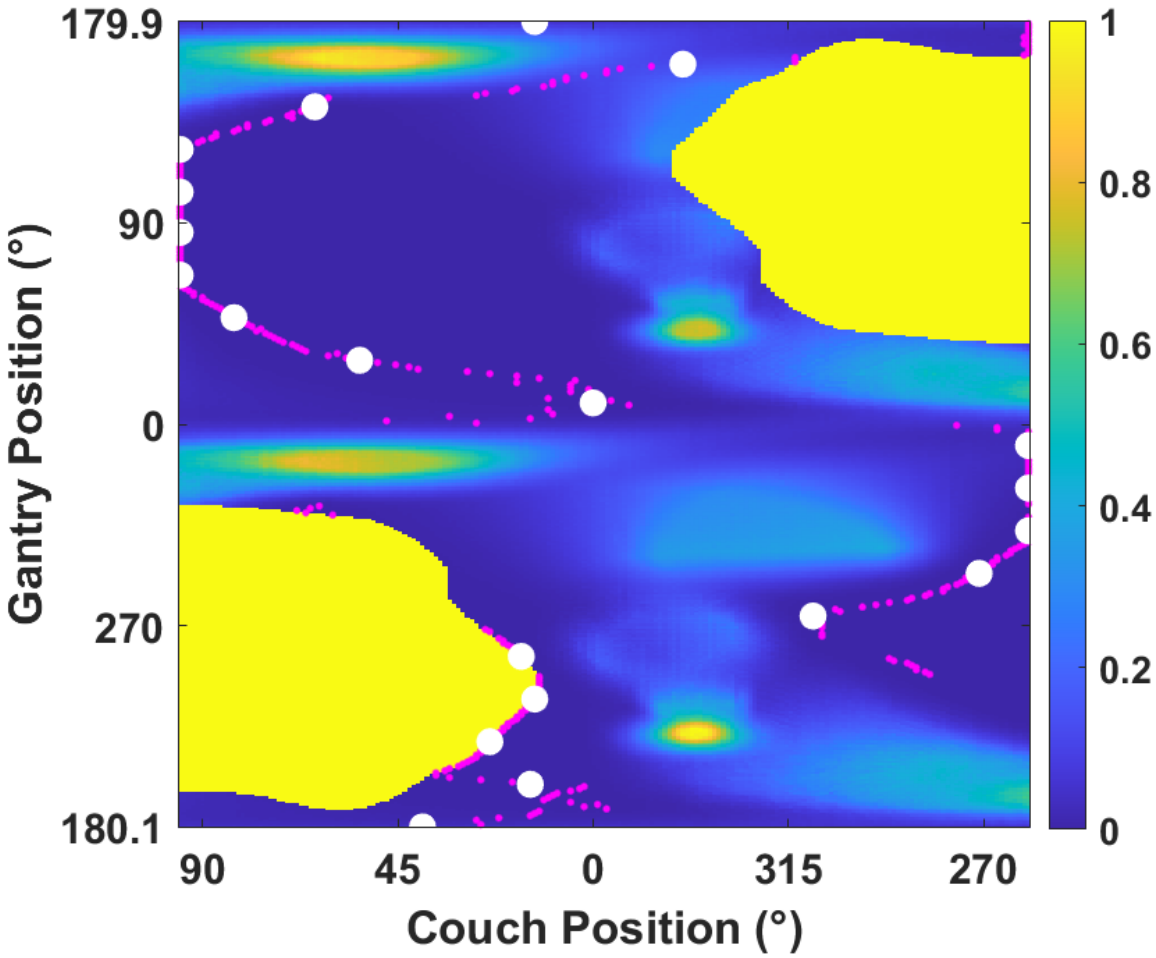

Figure 3.3: Example cost of BEV overlap map (4π map) with collision zones. Magenta dots indicate the minimum cost for each unique couch and gantry angle combination. White dots indicate 20 evenly sampled gantry angle points from that collection.

Non-coplanar optimizations resulting in IMRT ports have been studied in the literature[22,23] with dosimetric results suggesting potential for dose escalation in some cases. The work of Dong *et al.* [22,23] has been studied in hypofractionated regimes for liver and lung SBRT. In 10 liver SBRT cases, Dong *et al.* used non-coplanar optimization to integrate BEV optimization with fluence map optimization and a computer assisted design model for collision avoidance[23]. Optimized IMRT ports were selected using a greedy column generation approach resulting in 14 and 22 port solutions. Compared to coplanar VMAT their results showed reductions in mean liver dose (MLD) by 31% and statistically significant reductions in mean dose to left and right kidneys of 70% and 51%. They also found statistically significant maximum dose reductions for stomach and spinal cord of 67% and 64%, respectively [23].

They conducted similar research for 12 lung SBRT patients and attempted to lower the number of optimized non-coplanar IMRT ports[22]. Comparisons were again made with coplanar VMAT, using 7 to 9 non-coplanar IMRT ports, and found statistically significant dose reductions to the heart, esophagus, trachea, bronchus, and spinal cord of 32%, 72%, 37%, 44%, and 53% respectively[22].

Current clinical practice with non-coplanar fixed port IMRT on C-arm LINACs requires the radiation therapists to enter the treatment room between each fixed port and move the couch and/or gantry to the next fixed port position. The major limitation of these optimizations using IMRT is that although large numbers of fixed ports offer improved dosimetry, it comes at the expense of longer treatment times for patients. These limitations were addressed for the same disease sites (lung and liver SBRT) in manuscripts 5 and 6 by performing optimized non-coplanar arc selection.

3.1.2.2 Gantry Arc Trajectories

A gantry arc trajectory will be defined as a series of unique ports at more than one gantry angle where the couch remains static at one angle and the gantry sweeps through a range of angles in a continuous arc. Considering the map of Figure 3.1, a gantry arc can be thought of as a vertical line whose first point and last points are the starting and ending angles for the gantry arc. This is illustrated in Figure 3.4.

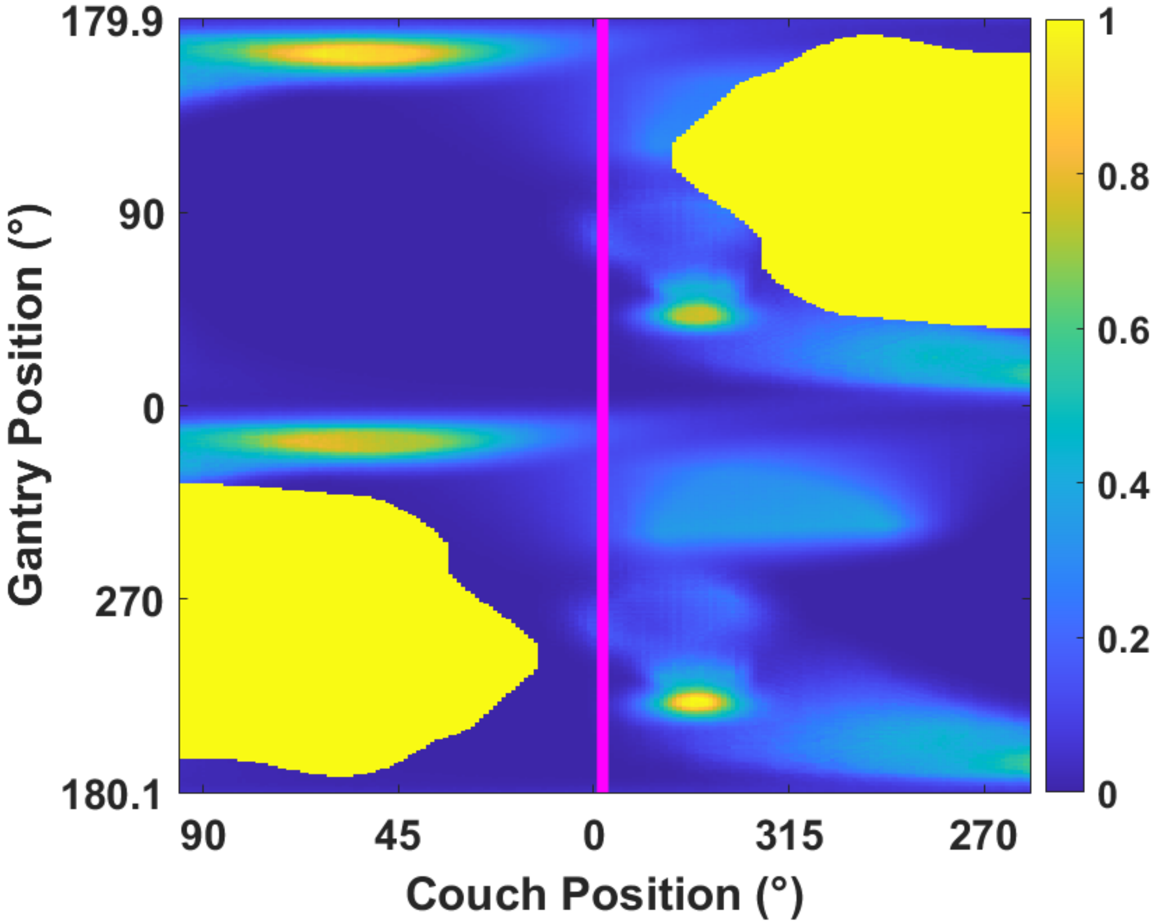

Figure 3.4: Example cost of BEV overlap map (4π map) with collision zones. The magenta line denotes a gantry arc trajectory where the couch remains static.

Research has been conducted that examined optimizations to choose gantry arc trajectories for 3D-conformal radiation therapy and/or dynamic conformal arc (DCA) therapy[61], however it has been well documented that the fluence modulation offered by IMRT consistently outperforms these techniques in terms of ensuring dose to OARs remains as low as possible with superior conformity and homogeneity[78].

The development of VMAT[4] resulted in a paradigm shift for radiation therapy as it significantly increased the efficiency of treatment delivery, while also ensuring the fluence modulation benefits of IMRT remained. As discussed in Section 2.6.2, VMAT optimization relies on initial input of gantry arc trajectories. Therefore, non-coplanar arc trajectory optimizations can be performed to generate optimized gantry arcs and potentially help to reduce the VMAT optimizer's burden of sparing normal tissue.

Gantry arc optimization, or static-couch optimization is a type of trajectory optimization where a collection of optimized sub-arcs at static couch positions with rotating gantry are chosen for treatment planning. These types of optimizations can be geometrically chosen without trajectory optimization such as the now commercially available HyperArc^{TM} (Varian Medical Systems, Palo Alto, CA). HyperArc^{TM} is based on work by Clark *et al.* who proposed a four-arc VMAT template geometry that includes non-coplanar arcs for SRS/SRT[79-82]. Ohira *et al.* compared this template with coplanar VMAT for 23 patients with one to four brain metastases[80] prescribed between 20 and 24 Gy in a single fraction. Reductions in the range of V4Gy to V16Gy were found in the brain using HyperArc configurations, with improved conformity and more rapid dose fall off compared to coplanar VMAT[80]. Although this non-coplanar arc arrangement was found to be superior to coplanar VMAT, it lacks anatomical information and patient specificity.

Furthermore, research by Woods *et al.* extended this research outside of the cranium and investigated selection of non-coplanar gantry arcs by a human planner for VMAT of the liver[83]. The authors compared these non-coplanar gantry arcs with 20 optimized non-coplanar IMRT ports and coplanar VMAT on a cohort of 20 liver SBRT patients receiving between 30 and 60 Gy[83]. Their results showed that compared to coplanar and non-coplanar VMAT, non-coplanar

IMRT plans reduced liver volumes receiving more than 15 Gy by 80 cm^3. They also concluded significant maximum dose reductions to OARs such as kidneys, spinal cord, and stomach for both non-coplanar VMAT and IMRT[83]. These authors concluded that non-coplanar IMRT was dosimetrically superior to coplanar and non-coplanar VMAT, however their non-coplanar arcs were chosen using human intervention and the 20 IMRT port deliveries could prove cumbersome to deliver clinically.

One conclusion from this research was a need to overcome the limitations of human intervention in arc selection, to find globally optimal solutions. MacDonald *et al.* have proposed a constrained modification of the Bellman-Ford algorithm[84] that gives an optimized set of sub-arcs for cranial SRS/SRT[5]. This algorithm performs a global search constrained by input parameters of arc length and number of arcs. The algorithm was used for optimized arc selection in Chapter 4 of this thesis. It is summarized in the following steps according to MacDonald *et al.*[5]:

1. Any arc solution has a starting and ending gantry angle for a given couch angle.
2. Any arc length defined by the difference between gantry starting and ending angle that is less than a constrained value m is removed from the solution.
3. Calculate the minimum cost arc solution for every valid gantry span.
4. Limit the combination of arc solutions to contain solutions with no more than x arcs.
5. The minimum cost arc trajectory is the valid combination of arcs that results in the lowest cost based on choices of m and x.

Okoli *et al.* used simulated annealing (SA) to investigate optimized non-coplanar VMAT arc selection in a prostate and liver case[85]. These findings motivate further research into larger scale dosimetric studies that include optimized non-coplanar arc selection. This has potential clinical implications as the use of non-coplanar VMAT arcs is readily available in most clinical treatment planning systems. Clinical considerations must be made in terms of proposed additions to existing clinical workflows.

3.1.2.3 Couch Arc Trajectories

In this section a couch arc trajectory will be defined similar to how we defined the gantry arc. In this case, the gantry remains at a static position while the couch is free to rotate continuously. Considering the cost map of Figure 3.1 a couch arc can be thought of as a horizontal line whose first point and last points are the starting and ending angles for the couch arc. This is illustrated in Figure 3.6.

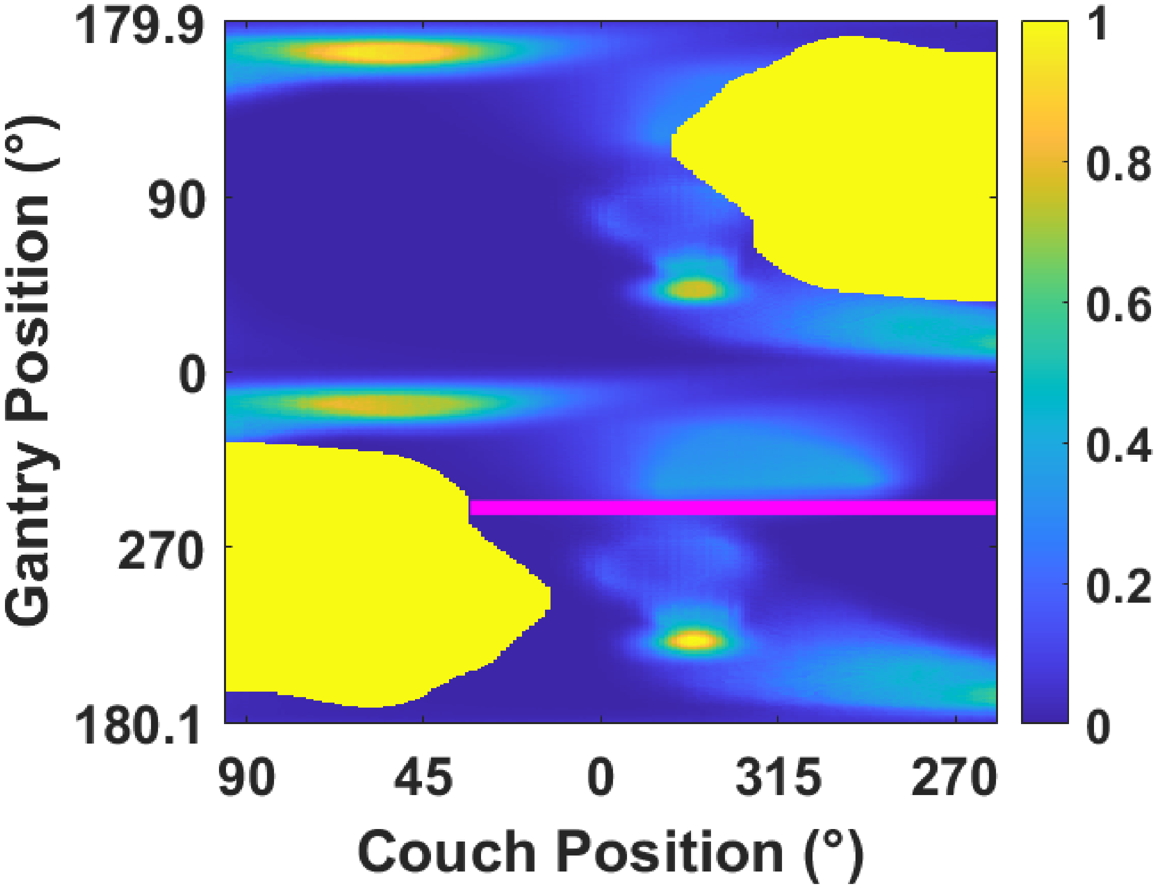

Figure 3.5: Example cost of BEV overlap map (4π map) with collision zones. The magenta line indicates a couch arc where the gantry remains static, and the couch rotates continuously.

There has been limited research to date on the use of couch arc trajectories as they are not straightforward to implement in most clinical treatment planning systems. There are also technical difficulties in the accuracy of the couch rotation system which could be a limiting factor on the delivery of treatment. This makes it difficult to perform the necessary dosimetric comparisons with current techniques. Shaitleman *et al.* proposed a method for accelerated partial breast (APBI) radiotherapy with couch arcs[78,86]. Optimization and dose calculation were performed at 10° intervals for the entire couch-arc ranging from its minimum to maximum value. The static gantry positions were manually set. Popescu *et al.* then extended this work to include up to 20° of gantry rotation for the potential of additional OAR sparing[87]. APBI was also investigated in the prone position using couch arcs with couch translations to minimize collisions[86,88].

3.1.2.4 Dynamic Trajectories

The discussion on navigation methods to this point have concerned static axes. Upon development of non-coplanar IMRT ports, it was hypothesized that coordinating the treatment axes of couch and gantry dynamically, would allow for much more efficient deliveries[62,89,90]. As with previous sections, we begin by looking at a dynamic trajectory considering the cost map of Figure 3.1. A dynamic trajectory is defined as a series of connected control points whereby the couch and gantry both rotate off the coplanar axis for delivery. These spaces can be navigated using different shortest path algorithms. The research group in Bern, Switzerland[7,24,25,91] uses the A* pathfinding algorithm[92], while MacDonald *et al.* have proposed use of a bi-directional gradient descent algorithm[29,30]. Others in the literature have also used Dijsktra's algorithm[74,76,93,94]. Each of these shortest path problems can solve a 2D rectangular graph for the minimum path. This is shown in Figure 3.7 where the dynamic trajectory is computed using a bi-directional gradient search algorithm[30].

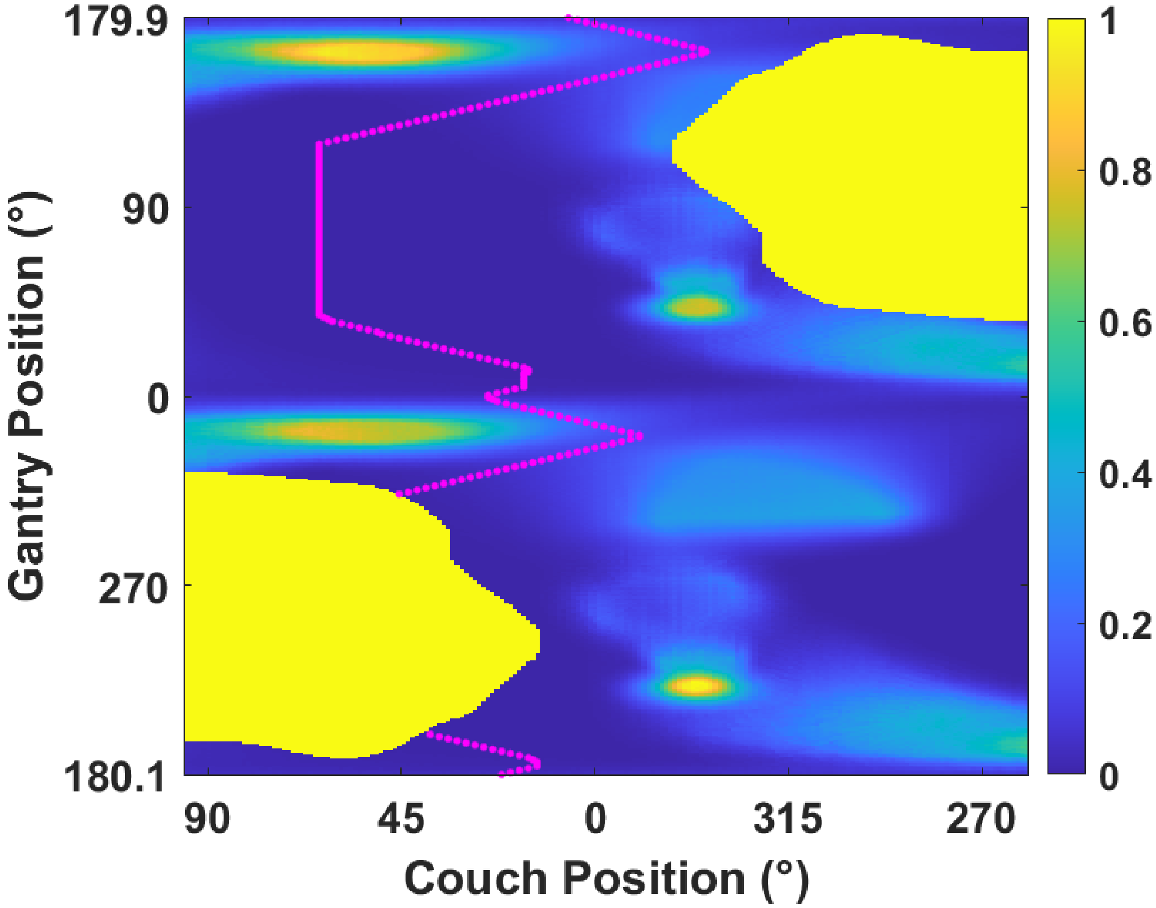

Figure 3.6: Example cost of BEV overlap map (4π map) with collision zones. Magenta dots represent a dynamic couch and gantry trajectory where both rotate continuously in tandem.

Dynamic trajectories have been researched and delivered clinically as early as 1988 where Podgorsak *et al.* proposed them for SRS[89,90]. Since then, there have been a myriad of techniques developed for dynamic rotation of the couch, gantry, and/or collimator[5,6,11,24,25,29-31,34,35,62,74,76,87,90,94,95]. The majority have also been developed in combination with fluence modulation to ensure adequate comparisons can be made with VMAT. These techniques aim to harness the OAR dose reduction capability demonstrated by non-coplanar IMRT, while also alleviating the major delivery efficiency limitation of multiple field IMRT that is clinically cumbersome, especially compared to VMAT.

Dynamic trajectory deliverability has only been validated in non-clinical settings such as Varian's Developer Mode for Truebeam® (Varian Medical Systems, Palo Alto, CA). Clinical treatment planning with dynamically optimized trajectories is currently limited to static-couch trajectories that approximate the path of a dynamically optimized trajectory. Research versions of clinical treatment planning systems can alleviate some of these limitations[24,25].

3.1.3 Mean Arc Distance (MAD)

The different types of trajectories described in Section 3.1.2 can each be quantified in terms of the cost incurred by delivering dose to overlapping BEV. However, another important consideration is the degree to which 4π space is sampled during a trajectory. This was the subject of MacDonald *et al.*[12] who proposed MAD – a trajectory sampling metric that quantifies the amount of 4π space sampled given an arbitrary trajectory.

MAD is defined by first creating a sphere with equally distributed points and then measuring the arc distance between every point on that sphere and all points for a given trajectory[12]. Control points containing positional information for the treatment couch and gantry are mapped into polar coordinates so they can be related to each point on the sphere. This is described by Equation 3.3[12].

$$\alpha_{j,k} = \tan^{-1}\left(\frac{\overrightarrow{a_j} \times \overrightarrow{b_k}}{\overrightarrow{a_j} \cdot \overrightarrow{b_k}}\right) \tag{3.3}$$

where $\alpha_{j,k}$ is the angle between a unit vector from the origin to a control point *j* along the given trajectory (*a*), and the unit vector from the origin to a sampling point *k* on the sphere (*b*). The closest control point to a given sampling point thus minimizes $\alpha_{j,k}$ and MAD is calculated according to Equation 3.4[12].

$$MAD = \mu_{\alpha} = \frac{1}{n}\sum_{(i=1)}^{n} \alpha_{i,\min} \tag{3.4}$$

where n is the total number of sample points.

These authors evaluated MAD using the matRad experimental TPS (Mathworks, Natick, USA) for single target cranial SRT in 2047 plans. Of these plans, 900 were fixed port 3D conformal, 900 were contiguous field DCA, and 192 were VMAT plans. Validation was performed in the Eclipse TPS for five synthetic and 10 clinical VMAT cases. Based on analysis of isodose volumes, they found that all isodose volumes greater than 10% of the prescription showed exponential decreases with decreasing MAD for all comparisons. Lower than 10% of the prescription, isodoses increased with decreasing MAD. They also found that larger target volumes yielded larger absolute dose reductions[12]. Thus, MAD correlates directly with conformity and fall off for isodoses larger than 10% of the prescription.

MAD provides the capability to evaluate the sampling of trajectories, specifically quantifying the degree to which arcs are spaced. This is a useful tool as increased 4π sampling may be related to conformity and can be balanced with the OAR dose reductions currently achieved with optimized BEV selection. This thesis extends the use of MAD from single target cranial SRT to lung and liver SABR in chapters 5 and 6, respectively.

3.2 Cranial 4π Algorithms

The previous section serves as an overview of the algorithms and methodologies that exist in the literature. A more thorough description of algorithms used with the cranial application of Chapter 4 are herein described. The discussion at times will be limited in specificity to the systems in place at the Nova Scotia Health Department of Radiation Oncology and Medical Physics, who use the Varian Eclipse$^{\text{TM}}$ (Varian Medical Systems, Palo Alto, CA) treatment planning system (TPS). However, in this section we aim to describe methods that are generalizable across radiotherapy vendors. The main analysis software used for algorithmic development was MATLAB (MathWorks, Natick, MA).

The research in this dissertation relies on the following steps:

1. Contour all relevant anatomical structures in Eclipse.
2. Create cost in 4π space by calculating cost heuristic for all possible machine states in MATLAB using anatomical structures.
3. Navigate the cost in 4π space using pathfinding algorithms for trajectory optimization in MATLAB.

3.2.1 Structure Delineation

After contouring, structures were exported in the digital image and communication in medicine (DICOM) format into MATLAB. DICOM files were read using the "dicomread.m" function which allows the user to extract relevant information into a native MATLAB "struct" data structure. Parsing this data structure yields a series of labels and 3D point clouds, where each point cloud corresponds to the outer boundary of a contoured structure. These point clouds are characterized by their position in cartesian coordinates, expressed as:

$$P = \begin{bmatrix} x_i \\ y_i \\ z_i \end{bmatrix} \tag{3.5}$$

Each individual structure needed to be characterized according to its type, and two types of structures were considered in the cranial optimizations: OAR and PTV. This work was limited to single target cranial cases, thus isocenter was realized by simply calculating the center of mass of the PTV structure. Once isocenter was calculated, all OAR structures were translated from the TPS coordinate system to the coordinate system for delivery, to simulate their treatment position on the linear LINAC. Given all the structure point clouds in the correct geometric positions, projection information was required to apply Equation 3.2.

3.2.2 GetProjectionSimple

Two-dimensional projections of the 3D point cloud at isocenter allow for the overlap calculation described in Equation 3.2. To get the 2D projection of a 3D point cloud we need to know how far it is being projected and by what angle. In this case, the projection is applied at a fixed isocenter which is 1000 mm source to axis distance (SAD) from the radiation source. The projection is applied at a specific couch and gantry angle combination. Using these inputs, transformation matrices were applied with the method of similar triangles to find the divergent projection of a specific structure in the BEV.

The transformation matrix that defines couch rotation was:

$$C = \begin{bmatrix} \cos\theta_c & 0 & \sin\theta_c \\ 0 & 1 & 0 \\ -\sin\theta_c & 0 & \cos\theta_c \end{bmatrix} \tag{3.6}$$

where *C* denotes the rotation matrix specific to the treatment couch, and θ_c denotes the couch angle by which the structures were rotated.

Similarly, the transformation matrix that defines gantry rotation was:

$$G = \begin{bmatrix} \cos\theta_G & -\sin\theta_G & 0 \\ \sin\theta_G & \cos\theta_G & 0 \\ 0 & 0 & 1 \end{bmatrix} \tag{3.7}$$

where G denotes the rotation matrix specific to the gantry, and θ_G denotes the gantry angle by which the structures were rotated.

The DICOM standard is a different coordinate system than that used in IEC1217, thus a final transformation was required to convert the structure set exported from Eclipse^{TM} to this local coordinate frame:

$$D = \begin{bmatrix} 0 & 0 & -1 \\ 0 & -1 & 0 \\ -1 & 0 & 0 \end{bmatrix} \tag{3.8}$$

where we define *D* as the DICOM to local coordinate frame transformation matrix.

The product of these matrices gives the final transformation matrix that correctly orients point clouds of the form *P*.

$$T = [C][G][D] \tag{3.9}$$

Where *T* is the final transformation matrix attained by multiplying each of the individual transformation matrices of Equations 3.7 through 3.9. The final set of rotated points P_R for a specific structure is:

$$P_R = [T]\bar{P} \tag{3.10}$$

where the vector of points $\bar{P}$.defines the unrotated structure.

Once the points have been rotated, the divergent projection in the BEV is found using the method of similar triangles. The plane at isocenter in the local coordinate frame is centered about the anterior-posterior (y) direction, thus the rotated points are all projected to the y plane at isocenter [0 1000 0]:

$$P_x = \frac{P_{R,x} * SAD}{SAD + P_{R,y}} \tag{3.11}$$

where P_x is the projected *x* points in the cartesian coordinate system, $P_{R,x}$ is the rotated *x* points, $P_{R,y}$ is the rotated *y* points, and *SAD* is the source to axis distance, 1000 mm. We also have:

$$P_z = \frac{P_{R,z} * SAD}{SAD + P_{R,y}} \tag{3.12}$$

Similarly, P_z is the projected z points in the cartesian coordinate system, $P_{R,z}$ is the rotated z points, $P_{R,y}$ is the rotated y points, and SAD is the source to axis distance.

Once the projected points P_x and P_z have been found, overlap can be calculated. A pictorial example is shown in Figure 3.7.

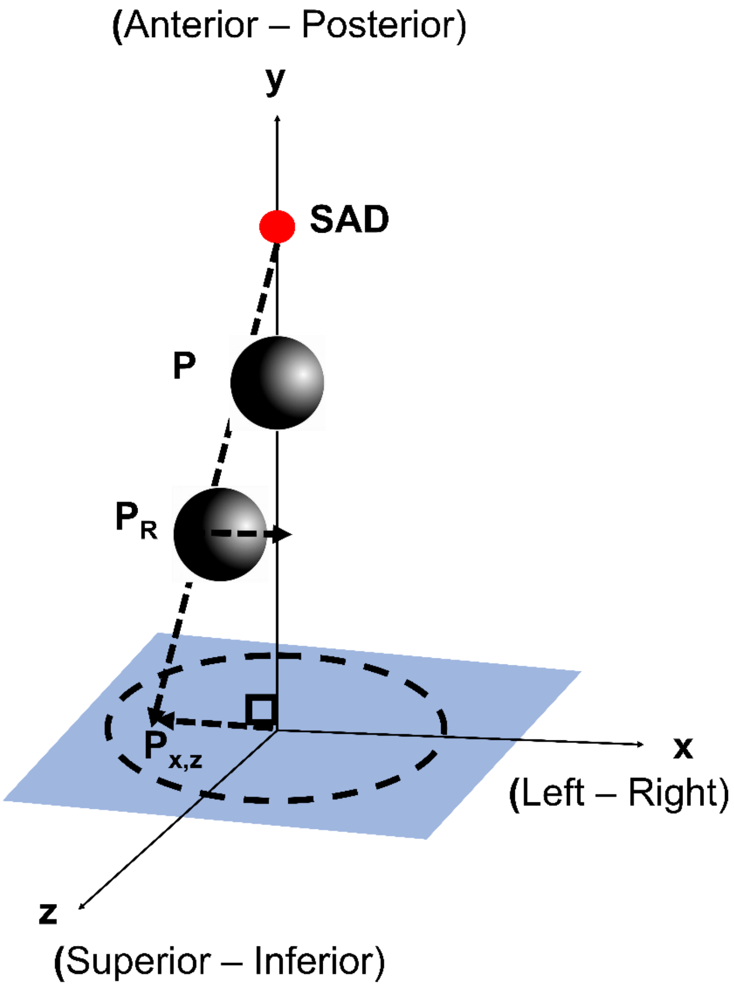

Figure 3.7: A pictorial example of applying the method of similar triangles in 3D to generate a 2D projection of a point P that has undergone a transformation to P_R and was then projected to the plane at isocenter. The source is shown in red along the y-axis and measures a source to axis distance (SAD) to isocenter in the plane.

3.2.3 GetBEVOverlap

As previously discussed, overlap is the metric by which cost is associated with choosing beams for irradiation where OARs overlap with the PTV. This is calculated according to Equation 3.2. The method is as follows:

1. Find the limits of a rectangle around the PTV and OAR based on the minimum and maximum PTV and OAR projection points. This corresponds to the minimum field size to encompass the entire PTV, which can never be larger than the maximum allowable field size of 40 x 40 cm^2.
2. Find the outermost limiting polygon around the PTV and OAR. This was calculated using the 2D "*boundary.m*" function in MATLAB, which takes inputs of the projected PTV and OAR points.
3. Build a mask of both the PTV and OAR in the positive x, y quadrant. This was done using the "*poly2mask.m"* function in MATLAB, which takes inputs of the boundary points found in step 2 and the rectangular limits found in step 1.
4. Count the number of pixels in the PTV and OAR masks found in step 3. This was done using the "*nnz.m*" which simply counts the number of nonzero elements of each input. This quantity represents the area of the PTV and the area of the OAR.
5. Find the overlapping pixels of the target and OAR masks. This was done using the logical "*and.m*" function in MATLAB, which takes inputs of the masks found in step 3.
6. Count the number of overlapping pixels found in step 5 using the "*nnz.m*" function. This quantity represents the area of the overlapping region.
7. Given each of the area calculations, the overlap is calculated exactly as shown in Equation 2.2.

This process is repeated for every combination of couch angle and gantry angle, as well as for every OAR being considered.

3.3 Extracranial 4π Algorithms

Similar to Chapter 3.2 a more thorough description of algorithms used with the extracranial applications of Chapter 5 and Chapter 6 are presented.

Moving outside the cranium is a natural extension of non-coplanar trajectory optimization techniques. One of the major complications is the significant decrease in available 4π space to deliver. There is greater potential for collisions with the patient due to the isocenter of treatment being further inferior in the patient, thus there is more of the patient occupying the possible 4π space. OAR considerations in extracranial sites can be extremely complex. The biology of most OARs in cranial radiotherapy are known to follow serial structures with well established dose limits. The exception here is the brain itself which is a unique OAR that encompasses the serial OARs and PTVs within it, with dose-volume limits corresponding to necrotic endpoints as mentioned in Table 2.1. OARs in the thoracic, abdominal, and pelvic regions have varying degrees of seriality. This is reflected by the varying dose constraints that accompany them based on fractionation, especially in the context of SABR. Finally, the size of OARs outside of the cranium can be much larger, and this must also be accounted for during algorithmic development.

In this section, algorithms will be described that facilitated building on the cranial cost associated with BEV overlap. While overlap remains a key consideration in these optimizations, it must be balanced with the size and varying dosimetry found in extracranial sites.

3.3.1 Structure Delineation

Structure delineation for extracranial settings was performed as in the discussion in Section 3.2.1 for cranial structures. The first main difference was that the body contour was included in this optimization to better characterize the depth of interactions inside the body compared to an overlapping area calculation. Second, due to the nature of the Moller-Trumbore algorithm that will be described in the following section, all structures needed to be triangulated.

Triangulation was performed using two methodologies. For the manuscript in Chapter 5 describing methods for lung SBRT, the open source Meshlab Software[96] was used to post process the body contour. Post processing removed imperfections of the point clouds exported from Eclipse™, while also allowing for reconstruction of meshes with far fewer triangular faces and corresponding vertices than originally found using MATLAB. Fewer faces and vertices are beneficial to increasing the overall efficiency of the ray tracing. Furthermore, Meshlab provides an algorithm for closing holes. This is useful as the point clouds exported from Eclipse™ potentially have large holes on either end of the CT-sim dataset, and their location in 4π space is important for avoidance. Both Meshlab reconstructed body contours with and without holes were imported back into MATLAB and subtracted to find the faces and vertices corresponding to the hole locations in 4π space. These structures were triangulated using the "*boundary.m*" function with a shrink factor of one to ensure a compact boundary was returned that envelopes the points. Once the triangulation was complete, all vertices, including the body contours, were shifted to isocenter as in the cranial methodology.

For the manuscript in Chapter 6 describing methods for liver SBRT, all calculations were performed in MATLAB by first down sampling the exported body contour from Eclipse™ to reduce the total number of faces from the resulting triangulation. Then, all structures were triangulated using the "*boundary.m*" function and shifted to isocenter. Holes corresponding to the ends of the CT dataset were identified through the ray tracing procedure and flagged if the number of intersections was one or zero.

Meshlab was used for the manuscript in Chapter 5 but not Chapter 6 as extending triangulation processes into MATLAB did not occur until the research for the third manuscript was conducted.

It was found through trial-and-error processes that in most cases these avoidance zones where patients may have their arms elevated where the CT ends, are covered by collision zones. However, as research develops into collision avoidance, understanding the location of these zones may become more important.

After all body, PTV, and OAR structures were pre-processed and triangulated, the next step was to identify the structures in the plane at isocenter.

3.3.2 Ray Tracing

Ray tracing is a technique well established in the field of computer vision for graphics purposes. The main concept concerns how light rays are transported to render a digital image of a scene. In radiotherapy it is routinely used as part of the complex process to simulate radiological interactions with matter[97]. Ray tracing has been used in 4π non-coplanar optimizations through work by Meyer *et al.* for 3D conformal radiotherapy[61] and Smyth *et al.* for dynamic couch and gantry VMAT[74,76]. The latter rely on Siddon's method[98] to compute intersections of rays with voxels that correspond to an OAR, while the former uses volumetric projections characterized by a grid at isocenter to calculate a "depth cost" and "volume cost" for both PTV and OARs[61].

3.3.2.1 *Concept and Rationale*

Equation 3.2 describes a cost score dependent on the ratio of overlapping areas to their respective structures. Areas of volumetric projections are structure size dependent, thus this equation is suitable for cranial radiotherapy where the sizes of both PTV and OARs being considered are approximately on the same order of magnitude (~10 cm^3 to ~100 cm^3). In extracranial sites OARs being considered such as lung, liver, or stomach measure on the order of 1000 cm^3. A generalizable method is preferred for both cranial and extracranial sites where these methodologies provide new capabilities to try to spare normal brain. Size differences may not be a problem if the PTV and OAR sizes were the same, however that is not always the case, especially extracranially. To emphasize the point, we can take the limit of Equation 3.2 as the projected area of an OAR approaches infinity:

$$\lim_{A_i \to \infty} \sum_{i=1}^{n} \frac{L_i(c,g)}{A_t(c,g)} \times \frac{L_i(c,g)}{A_i(c,g)} = 0 \tag{3.13}$$

It is readily apparent that for a constant amount of overlap and PTV size, a large OAR will dominate the cost equation, erroneously producing low-cost geometries that could be unfavourable.

This limitation may not have been addressed by Dong *et al.*[22,23] since the probability of choosing 7 to 22 unfavourable IMRT ports is low if there is enough 4π space to sample. They incorporated fluence modulation in their optimizations and found superior OAR sparing using these IMRT ports.

Introduced through the manuscript in Chapter 5, we propose ray tracing as a methodology to be combined with the physical concept of BEV as a solution to the limitation described in Equation 3.13. The structure of this methodology is similar to existing ray tracing concepts in radiotherapy [61,74,76], but differs in the implementation details and specific algorithms used.

3.3.2.2 Moller Trumbore

To overcome the size restriction hindering Equation 3.13, we hypothesized that BEV cost was also related to depths to the PTV and OAR. Raytracing provides a method to assess that hypothesis, [61,74,76] but it also required efficiency due to the large OARs in extracranial radiotherapy.

While Siddon's method[74,76,98] and the grid based ray tracing volume/depth cost[61] have been proposed, neither have discussed efficiency benefits compared to the Moller-Trumbore algorithm, a ray tracing algorithm that is widely used in the field of computer vision due to its fast and minimum storage nature[99]. The algorithm is fast as it reduces the number of rays to be traced to the number of triangles in each mesh, compared to a larger number of points in a voxelated scene. Its speed is also aided by only storing intersections with triangles instead of all points along a ray line[99]. The Moller-Trumbore algorithm is explicitly detailed in their 2005 publication "*Fast, minimum storage ray/triangle intersection*"[99]:

A ray *(R)* scaled by a distance *(t)* given a source origin *(S)* and direction *(D)* can be defined as:

$$R(t) = S + tD \tag{3.14}$$

A triangle can then be defined by three vertices as shown in Figure 3.8:

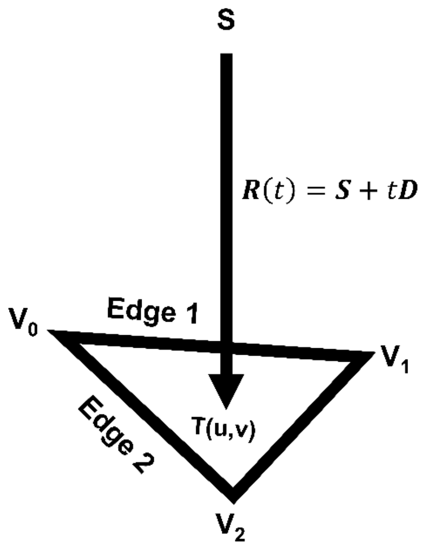

Figure 3.8: Diagram illustrating ray triangle intersection. Triangle vertices are given as V_0, V_1, and V_2. Edges are defined as the differences between each vertex. The radiation source is given as S, and the ray is characterized by equation 3.14.

The intersection is characterized the distance to the intersection *t* and the coordinates of the intersection, defined as *(u, v)*. This is done by applying a transformation to the source point of the ray.

The following equation describes a point *T (u, v)* on a triangle:

$$T(u, v) = (1 - u - v)V_0 + uV_1 + uV_2 \tag{3.15}$$

The geometry must be preserved such that the point *T* must be within a triangle formed by V_0, V_1, and V_2. As such Equation 3.15 is subject to $u \geq 0, v \geq 0, u + v \leq 1$. An intersection between *T* and *R* occur when they are equated:

$$S + tD = (1 - u - v)V_0 + uV_1 + uV_2 \tag{3.16}$$

Upon rearranging:

$$[-D \quad E_1 \quad E_2]\begin{bmatrix} t \\ u \\ v \end{bmatrix} = T \tag{3.17}$$

where E_1, and E_2 are the edges found by subtracting ($V_1 - V_0$) and ($V_2 - V_0$) respectively. $T = S - V_0$ which corresponds to the intersection location when shifted to the origin. Cramer's rule is then applied to solve Equation 3.17:

$$\begin{bmatrix} t \\ u \\ v \end{bmatrix} = \frac{1}{|-D, \quad E_1 \quad E_2|} \begin{bmatrix} |T, & E_1, & E_2| \\ |-D, & T, & E_2| \\ |-D, & E_1, & T| \end{bmatrix} \tag{3.18}$$

Finally, using properties of determinants, Equation 3.18 is simplified to:

$$\begin{bmatrix} t \\ u \\ v \end{bmatrix} = \frac{1}{(D \times E_2) \cdot E_1} \begin{bmatrix} (T \times E_1) \cdot E_2 \\ (D \times E_2) \cdot T \\ (T \times E_1) \cdot D \end{bmatrix} \tag{3.19}$$

Given the intersections *t* and the locations (*u, v*) calculations were performed to compute a new cost.

3.3.3 Identifying Overlap Region

The first step in isolating the overlap region differed slightly from the cranial methodology, as a concept from Meyer *et al.*[61] was adopted. A grid was created whose dimensions measured the maximum of each planar direction for the PTV projection at isocenter. This grid resolution was a tunable parameter set to 5 mm for the two extracranial manuscripts in this dissertation.

The next step was to project an OAR into the plane at isocenter and perform a series of overlap checks using the "*boundary.m*" function. Given an OAR overlapping the PTV, the points were matched to their corresponding locations on the grid using the "*inpolygon.m*" function to filter out any non-overlapping points from the grid.

3.3.4 GetProjectionSimple

The same volumetric projection method described in Section 3.2.2 was used for the extracranial optimizations. It served the purpose of rotating the vertices for each of body, PTV, and OAR triangulations after direction vectors were calculated to ensure rays were traced through the properly oriented triangulations.

3.3.5 Dose Surrogate

The manuscript comprising Chapter 5 introduces the concept of a surrogate for dose that is calculated by using exit and entrance distances of a particular structure interpolated onto a percent depth dose curve (PDD). The discussion in this section will highlight specific algorithmic details that are not covered in that chapter.

Each of the points containing overlap from Section 3.3.3 serves as a direction vector as measured from the radiation source. Using these direction vectors for ray tracing allows for intersections to be calculated for all the structures in question.

Exit and entrance distances of a single ray for each structure are quantified as the minimum and maximum distances from the source. The comparative exit and entrance distances for PTV and OAR are interpolated onto the PDD only after subtracting the body entrance distance. The area under the PDD curve (AUC) is then calculated using the "*trapz.m*" function for numerical integration by the trapezoidal method between the entrance and exit distance of the structure. Finally, the metric is normalized by dividing the partial AUC through the structure by the entire AUC. In Chapters 5 and 6, cost was specifically associated with this metric calculated for OARs, although it is possible that incorporating the PTV could provide a potential avenue for future research.

It becomes readily apparent why an efficient ray tracing methodology is required for these cases due to the computational overhead required. In extracranial cases there are many large OARs, each being traced by many rays, for 68,400 unique combinations of couch and gantry angle (assuming 1° sampling).

4 Chapter 4: Comparison of Anatomically Informed Class Solution Template Trajectories with Patient Specific Trajectories for Stereotactic Radiosurgery and Radiotherapy

4.1 Prologue

This manuscript is an investigation to assess the effectiveness of BEV optimization to generate anatomically informed class solution trajectories in comparison to patient specific trajectories and a geometric four arc class solution. It applies the methods of cranial BEV optimization described in Section 3.2 with the methods described by MacDonald *et al.*[5] to generate optimized arc trajectories for six cranial class solutions and patient specific solutions. A reproducible semi-automatic treatment planning process was created to compare treatment plan quality between the three increasingly complex methods of arc selection. This work highlights the importance for treatment planners and clinicians alike of anatomical considerations and, by extension, patient specificity in treatment planning.

This manuscript was published in the Journal of Applied Clinical Medical Physics:

"Lincoln JD, MacDonald RL, Little B, Syme A, Thomas CG. Comparison of anatomically informed class solution template trajectories with patient-specific trajectories for stereotactic radiosurgery and radiotherapy. *J Appl Clin Med Phys. 2022; 23; e13765.*"[100]

See Appendix A.1 for copyright permission.

4.2 Abstract

Purpose: Class solution template trajectories are used clinically for efficiency, safety, and reproducibility. The aim was to develop class solutions for single cranial metastases radiotherapy/radiosurgery based on intracranial target positioning and compare to patient-specific trajectories in the context of 4π optimization.

Methodology: Template trajectories were constructed based on the open-source MNI average brain. The MNI brain was populated with evenly spaced spherical target volumes (2 cm diameter, N = 243) and organs-at-risk (OARs) were identified. Template trajectories were generated for six anatomical regions (frontal, medial, and posterior, each with laterality dependence) based on previously published 4π optimization methods. Volumetric modulated arc therapy (VMAT) treatment plans generated using anatomically informed template 4π trajectories and patient specific 4π trajectories were compared against VMAT plans from a standard four-arc template. Four-arc optimization techniques were compared to the standard VMAT template by placing three spherical targets in each of six anatomical regions of a test patient. This yielded 54 plans to compare various plan quality metrics.

Results: Increasing plan technique complexity, the total number of OAR maximum dose reductions compared to the standard arc template for the 6 anatomical classes was: 4+/-2 (OFIXEDc), and 7+/-2 (OFIXEDi). In 65.6% of all cases, optimized fixed-couch positions outperformed the standard-arc template. Of the three comparisons, the most complex (OFIXEDi) showed the greatest statistical significance compared to the least complex (VMATi) across 12 plan quality metrics of maximum dose to each OAR, V12Gy, total plan Monitor Units, conformity index, and gradient index ($p < 0.00417$).

Conclusion: In approximately 70% of all cases, 4π optimization methods outperformed the standard-arc template in terms of maximum dose reduction to OAR, by exclusively changing the arc geometry. We conclude that a trade-off exists between complexity of a class solution methodology compared to patient-specific methods for arc selection, in the context of plan quality improvement.

4.3 Introduction

Recent advances in radiotherapy have enabled the ability to automate treatment planning procedures while ensuring there are no losses in dosimetric plan quality compared to conventionally planned treatments[101-104]. In cranial stereotactic radiosurgery/ radiotherapy (SRS/SRT) an example of one such automation is the HyperArc™ product by Varian Medical Systems (Palo Alto, CA, USA)[80]. HyperArc offers a push button solution to cranial SRS/SRT by employing a noncoplanar template solution of arcs, published by Clark *et al.*[79]. This arc-geometry template will be defined for use in this research as "the standard arc template" for sake of comparison at our institution. The standard arc template includes four arc trajectories: a full coplanar arc, a partial vertex arc, and two partial noncoplanar arcs where the treatment couch is offset by 45° to each side of the 0° couch position. While this arc geometry can be used as a starting point for cranial SRS/SRT volumetric modulated arc therapy (VMAT), it does not consider the cranial anatomy from a given beams-eye-view (BEV). BEV-based beam selection, whether it be fixed-port intensity modulated radiotherapy or VMAT, has been shown to be an effective tool for reducing normal tissue doses[24,30,34,35,62,74] because it assists in the selection of beams that do not result in BEV overlap between targets and organs-at-risk (OARs), thus avoiding irradiation of those OARs.

A step between the extremes of patient specific optimization and a fixed-arc template geometry solution like HyperArc™ could be a class solution based on patient anatomy. Class solutions can facilitate radiotherapy treatment planning by giving a template to planners upon which the treatment plan can be further optimized. Templates have the added benefit of reducing variation in the planning process, which can lead to improved efficiency, and reproducibility due to their familiarity to the planner. The HyperArc solution discussed above is an example of such a template, where the planner is removed from the arc selection decision but can also modify it as desired. Class solutions have been used in prostate treatment planning[105,106], for whole brain irradiation[107], and for SBRT of spinal indications[108]. Podgorsak *et al*., and Wilson *et al.*, proposed the utility of noncoplanar class solutions for SRS[90,95], however none of these preceding solutions have used an anatomical approach, such as an overlap-guided methodology, for geometry selection. In an era where treatment plan automation is becoming more prevalent, increasingly sophisticated methods are needed to ensure that OARs are spared as much as reasonably achievable. Moreover, these plans also need to be robust in different geometries. Given that there is a precedent for planners using templates in SRS and SBRT, a natural step forward is to include anatomical information to create such a template. These templates could then be compared with the template of Clark *et al.* and patient specific trajectories. Each of these planning techniques can be considered in terms of a tradeoff between their degree of complexity in geometric arc selection and ability to improve plan quality.

In this study, a novel method was developed to create anatomically informed template trajectories (class solutions) for cranial SRS/SRT by employing 4π optimization methods based on the methods of MacDonald *et al.*[30] to calculate BEV overlap maps for each region of a segmented cranial template. To allow these plans to be optimized in the clinical treatment planning system, navigation methods were restricted to fixed couch (non-simultaneous motion of couch and gantry) optimizations that would allow for VMAT optimization in a clinical treatment planning system (TPS) once optimized arc geometries were determined. This methodology also facilitates ease of clinical translation with minimal change to current practice.

The objectives of our study were as follows:

1. Develop a novel methodology to create anatomically informed template trajectories.
2. Compare an anatomically informed class solution against a patient specific map navigation.
3. Compare methods to the standard arc template used in SRS/SRT.

The methods chosen for fixed-couch navigation optimization is derived from previously published work of MacDonald *et al*.[5] that chooses the best of up to four fixed-couch arcs unconstrained by gantry arc span.

This work serves to investigate whether 4π optimized class solutions would be sufficient when treating single metastases in the brain with SRS/SRT, using increasingly complex methods of arc selection to reduce doses to OARs compared to a four-arc geometric template. Sampling 4π space with an anatomically informed class solution approach will give a better sense of anatomical relevance compared to a standardized geometric arc placement. The class solutions should be anatomically informed to account for relevant anatomies and differential overlap in separate regions of the brain. Anatomically informed class solution templates will also be compared to patient specific arc trajectories to investigate the tradeoff between customization and efficiency in arc selection. Finally, the methodology herein is generalizable to any anatomical location in the body.

4.4 Methodology

4.4.1 Creating an accurate anatomical model for cranial SRS/SRT template trajectories

All work done to create an accurate anatomical model and associated trajectories was performed in MATLAB version 2018b (MathWorks, Natick, MA). To develop template trajectories that were anatomically informed for cranial cases, the Montreal Neurological Institute's (MNI) average brain was used as a generic brain[109]. This anatomy is based on automated co-registration of 305 T1-weighted MRI scans and aligned in Talairach space[109]. Relevant OARs were contoured and merged into a singular avoidance structure, while the normal brain tissue was taken as the outer contour of the MNI brain with the targets subtracted. A singular avoidance structure combining all OARs was chosen to solely focus on amount of BEV overlap with a given target, removing bias between potential region of interest (ROI) combinations. OARs incorporated into this model were: brainstem, chiasm, left and right optic nerves, left and right eyes, and left and right lenses. This methodology was a modified version of the BEV overlap calculation performed by MacDonald *et al.* [30] where fractional overlap is dictated by each OAR individually. Collision zones on the maps were all manually measured as per MacDonald *et al.*[30]

The next step in creating the model was to populate the MNI brain with targets. For each target that was placed inside the brain, an overlap map was calculated based on the method of MacDonald *et al.* [30] for all possible couch and gantry angle combinations at 1-degree resolution. The MNI brain was filled by systematically placing 243 equally sized (2 cm diameter), equally spaced (2 cm apart) targets inside the outer contour (normal brain tissue) (Figure 4.1).

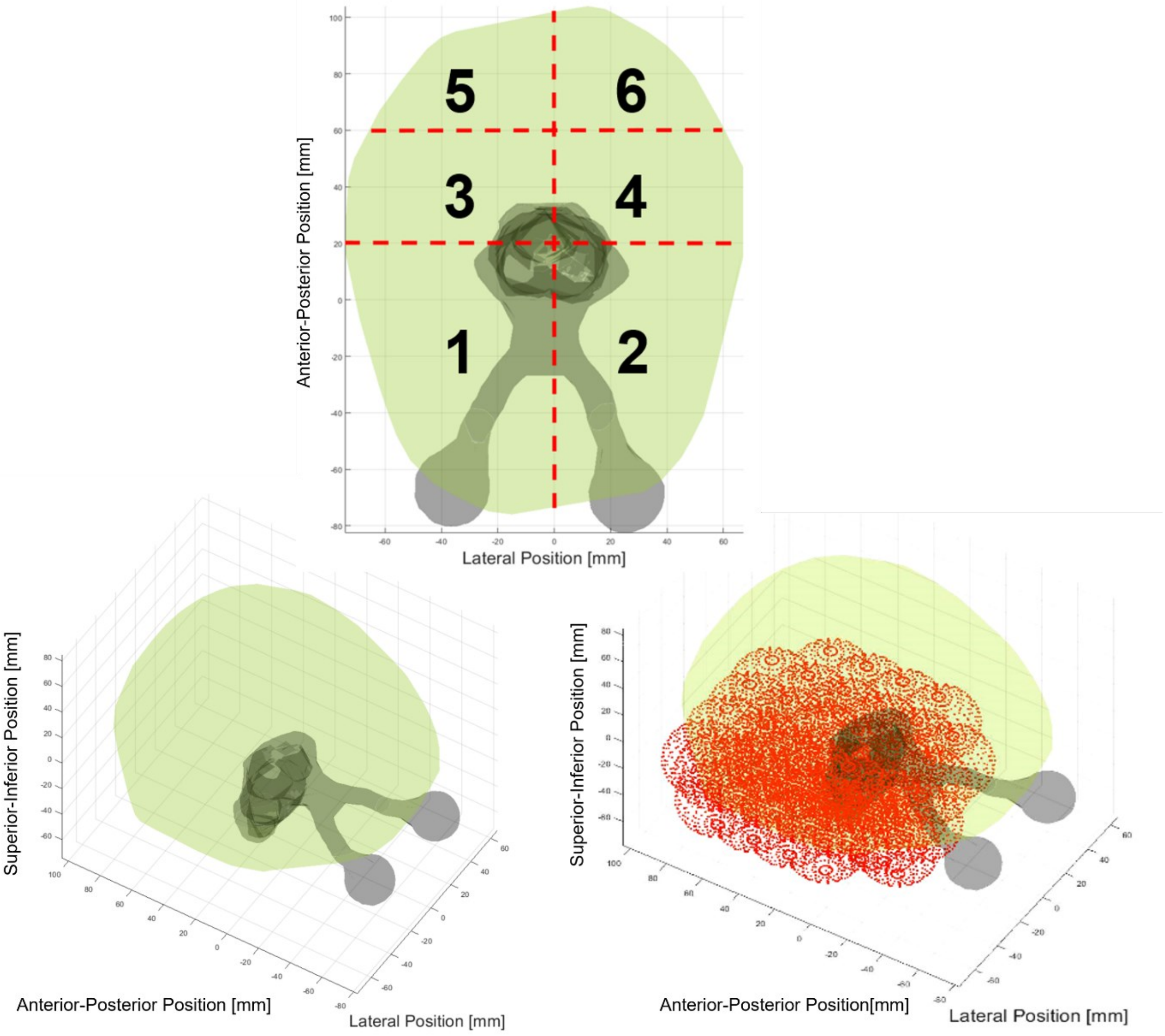

Figure 4.1: (Bottom Left) The MNI brain[109] outer contour (light green), with summed organs-at-risk (OAR) structures (grey). (Bottom Right) Mid-way through the systematic placement of equally spaced, equally sized 2 cm diameter spherical targets, constrained to be inside the normal brain outer contour. (Top) segmentations for the MATLAB simulations: frontal, medial, and posterior segmentations are shown, each with lateral dependence.

The brain was then segmented into six distinct anatomical segments to enable anatomically informed template trajectories to be calculated for each. These segments were: frontal, medial, and posterior, each with lateral dependence. The MNI brain was segmented according to the following rules, measured in accordance with Figure 4.1:

1. Divide left and right hemispheres along the lateral position (x = 0 mm). Right hemisphere was denoted as negative lateral position values, while left hemisphere was denoted as positive lateral position values.
2. Frontal segments spanned from the most negative (~-80 mm) anterior-posterior position of the outer contour to the anterior-posterior position of 20 mm.
3. Medial segments spanned from the 20 mm anterior-posterior to 60 mm anterior-posterior.
4. Posterior segments spanned from 60 mm anterior-posterior to the most positive (~100 mm) anterior-posterior position.
5. Given lateral and anterior-posterior limitations that define a two-dimensional projection, include all superior-inferior values encompassed by these limitations to define three-dimensional segment.

4.4.2 Segmenting the anatomical model to calculate overlap maps

Of the 243 synthetic targets generated during the simulation, an average overlap map was needed for each of the six anatomical segments, which could then be navigated. These were determined by calculating the maximum amount of overlap for every couch and gantry angle combination on a per-anatomical segment basis. This ensured a conservative overestimate of all overlap scores for each anatomical segment's template map.

With these anatomically informed template maps, anatomically informed class solution template trajectories were calculated using methods based on previously published 4π methodologies. The method was proposed by MacDonald *et al.* [5] that uses optimal pathfinding to choose the best fixed-couch arcs given any overlap map. Constrained solely by the Eclipse^{TM} (Varian Medical Systems, Inc., Palo Alto, CA) TPS version 13.6 restrictions that dictate no

VMAT arcs can span less than 30-degrees [110], this optimal fixed-couch (OFIXED) algorithm will automatically choose sub arcs that are not limited to being of equal length with fixed-couch positions that offer the lowest overlap for a given overlap map. In this research, OFIXED was further constrained to match the sub arc limit of four, in agreement with the total number of couch positions used in the standard arc template.

The fixed-couch positions and arc geometries were used in the generation of VMAT plans using Eclipse^{TM} version 13.6.

4.4.3 Generating synthetic cases in Eclipse for planning

Once the anatomically informed template trajectories were calculated, the Eclipse contouring tool was used to create synthetic spherical targets inside a previously treated patient's cranial dataset, different than the MNI brain, which was segmented according to the same method used in the simulations of Section 4.4.1. Three spherical targets (diameters 0.5 cm, 1 cm, and 2 cm) were placed in each segment, one at a time, yielding a total of 18 synthetic cases.

After all the synthetic cases were created, the structure set was exported from Eclipse so patient-specific overlap maps could be calculated in Matlab. Once each of the 18 patient-specific overlap maps was calculated, OFIXED algorithm was used to generate fixed-couch arc trajectories for them.

4.4.4 Eclipse planning procedure

To establish whether dosimetry is impacted by the type of 4π fixed couch sub arc optimization, comparisons were performed between plans that were VMAT optimized after performing fixed-couch optimizations. These optimizations were based on overlap from anatomically informed class solution overlap maps, and patient specific overlap maps.

For all 18 synthetic cases, three for each of the six classes, three plans were created with VMAT optimization, yielding a total of 54 plans. Overall, these three different planning methodologies for comparison were identified in order of increasing complexity as:

1. VMATi = The standard arc template.
2. OFIXEDc = Anatomically informed class solution with fixed-couch trajectory generated from the OFIXED algorithm.
3. OFIXEDi = Patient-specific solution with fixed-couch trajectory generated from the OFIXED algorithm.

Each plan had a prescription dose of 2400 cGy prescribed to the 90% isodose level, to be delivered in a single fraction to the synthetically created spherical planning target volume (PTV). The OARs considered for the VMAT optimization were left and right eyes, left and right lenses, brainstem planning-risk-volume (PRV), optic chiasm PRV, and left and right optic nerve PRVs. The PRV included in these optimizations were 2-mm expansions of their respective OAR, and all OARs were subjected to upper dose VMAT optimization objectives. These optimization objectives instructed the VMAT optimizer to satisfy the objective that no percent of the total volume of an OAR should receive more than a specific dose value. Optimization objectives are inputs to the VMAT optimizer that attempt to drive the optimization into satisfying certain clinical constraints. In this manuscript, we use optimization objectives to first ensure adequate coverage of the PTV with the prescription dose, and then wherever possible to decrease maximum doses to OAR below their clinical tolerances.

To calculate upper dose optimization objectives for each OAR, distances were measured from the synthetic spherical PTV in each case to the OAR in every slice of the CT simulation dataset. Upper dose optimization objectives were taken as the prescription dose (2400 cGy) minus 10%/mm multiplied by the minimum distance of the OAR to the PTV, to systematically consider dose fall off when the PTV was proximal to OAR[111,112]. For example, if the brainstem was 1.7 mm proximal to the PTV, the upper dose optimization objective was set to:

$$100\%Rx - 1.7[mm] * 10\left[\frac{\%Rx}{mm}\right] = 100\%Rx - 17\%Rx = 83\%Rx \tag{4.1}$$

Therefore, in this case, the brainstem PRV upper dose optimization objective would be such that 0% of the brainstem PRV volume could receive more than 83% of the prescribed 2400 cGy dose, 1992 cGy.

In the cases where the OAR was more than 10 mm from the PTV, the upper dose optimization objective was set to a value of 150 cGy, to minimize the dose to the OAR as much as possible without placing unreasonable demands on the VMAT optimizer. Here, we define a "proximity constrained OAR" as any OAR that was less than 10 mm from the PTV, and thus required an upper dose optimization objective to be calculated from Equation 4.1. A table detailing all proximity constrained OARs for each plan can be found in the supporting information (Supplemental Information Table 4.6).

Furthermore, as a tool to try to maximize dose conformity to the target, a surrounding symmetrical tuning ring structure was created for each PTV with an outer diameter of 3 cm and an inner diameter of 1 cm. The tuning ring upper dose optimization objective was set at 0% volume to receive 33% of the 2400 cGy prescription dose (800 cGy).

Finally, when optimizing the PTV, upper and lower dose optimization objectives were applied to ensure that the entire PTV volume (>99%) received the prescription and to ensure that any hotspot was limited to no more than 15% of the prescription.

General VMAT optimization parameters included an automatic normal tissue optimization set to a priority of 175 and VMAT optimization grid set to "fine" (1.25 mm) within the VMAT progressive optimization algorithm version 13.623 [110]. When performing the final dose calculation algorithm (AAA version 13.623) for all plans after VMAT optimization[113], the dose calculation grid size was set to 1.5 mm, the closest option to the VMAT optimization grid.

Moreover, the objective of this research was to create a methodology that could be reproduced through automation. Each plan was optimized only once to ensure we would be comparing effects of only changing arc trajectories based on the method used for arc selection. This was further ensured by maintaining dose optimization objectives between plans and only changing arc geometries.

4.4.5 Dose comparison and plan quality comparison

Following VMAT optimization and dose calculation for all plans, the two categories chosen for comparison were OAR maximum doses and other plan quality metrics. Dosimetric comparison between plans was a comparison of maximum dose as the metric of interest for various OARs, as the brain is a structure comprised of many serial organs. Plan quality comparisons were the volume of the normal brain, excluding the target, that receives 12 Gy (V12Gy); total plan monitor units (MU); plan conformity index (CI)[114]; and plan gradient index (GI)[115]. The definition of CI used in this research was the Paddick conformity index shown in

Equation 4.2[114], while the definition of GI used in this research was the Paddick dose gradient calculation shown in Equation 4.3 [115].

$$CI = \frac{V_{T,ref}}{V_T} * \frac{V_{T,ref}}{V_{ref}} \tag{4.2}$$

In this definition, $V_{T,\,ref}$ is the volume of the target receiving a dose equal to or greater than the reference dose, V_T is the volume of the target, and V_{ref} is the volume receiving a dose equal to or greater than the reference dose[114]. In this work, the reference dose was chosen to be the prescription dose of 2400 cGy.

$$GI = \frac{V_{\left(\frac{Rx}{2}\right)\frac{Rx}{2}}}{V_{Rx}} \tag{4.3}$$

In this definition, the gradient index is defined as the ratio of the volume of half the prescription isodose to the volume of the prescription isodose[115].

Maximum dose comparisons were performed between classes for all the plans corresponding to each anatomical segment. This consisted of averaging over the three targets placed in each segment. This allowed for six sets of maximum dose comparisons to be performed.

Plan quality metrics were compared across each of the three planning techniques by investigating each metric. Each planning technique was performed on the 18 distinct cases described above. This results in a series of multiple independent comparisons of 12 separate plan quality and dose metrics.

To account for this when performing statistical testing, a p-value was calculated via a Wilcoxon-Signed Rank Test for each metric inside a plan technique comparison, as the data were not normally distributed. Each test was two tailed. Comparisons were made for three planning techniques, thus three comparisons (three choose two) to perform for each of the 12 plan quality metrics, yielding 36 comparisons in the dataset. A full Bonferroni correction here would give a corrected significance level of 0.05/36 = 0.00139, which given the comparatively small sample size (N = 18) is extremely conservative. The Bonferroni corrected significance level was taken as 0.05/12 = 0.00417 (Bonferroni corrected significance per comparison). A full table of plan technique comparison as well as a full table of p-values are given in the supporting information (Supplemental Information Table 4.4 and Table 4.5).

4.5 Results

4.5.1 Overlap maps generated from segmenting an anatomical model

Performing calculations described in section 4.4.2 yields the following anatomically informed class solutions and corresponding overlap maps (Figure 4.2).

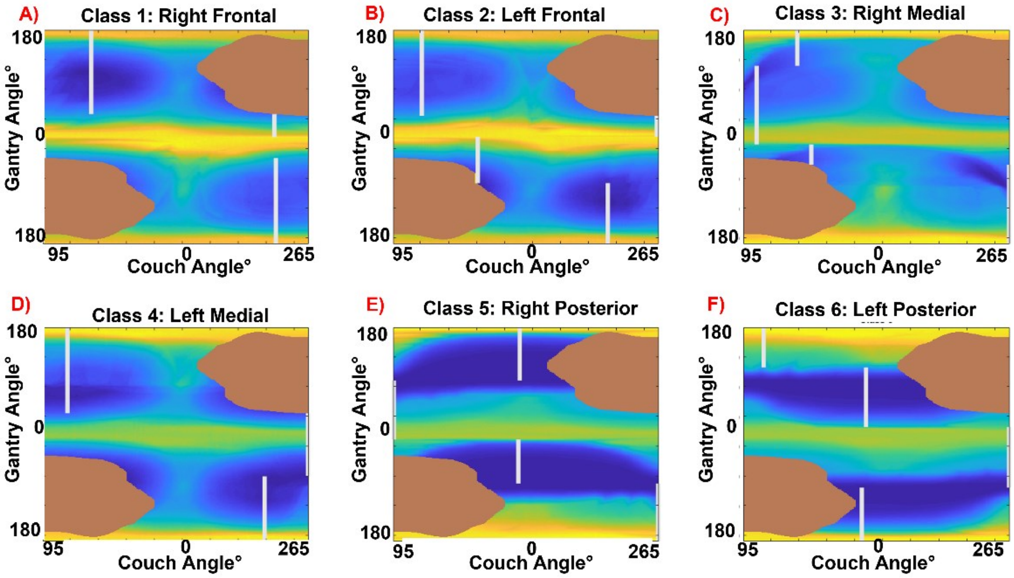

Figure 4.2: Trajectory class solutions for each of the ROI template maps denoted by "Class 1 – 6". Brown regions were manually measured collision zones[30], white lines are fixed couch trajectories measured using OFIXED algorithm. Regions of high BEV overlap between organs-at-risk (OARs) and the target are yellow, while dark blue indicates regions of low overlap.

4.5.2 Intra-class maximum dose comparisons

The following results in Figure 4.3 illustrate the average maximum dose difference relative to the standard arc template, over the three synthetic targets for an example anatomical class. In this case, anatomical "Class 1" was chosen, which corresponds to the "Right Frontal" overlap map of Figure 4.2A. All error bars are the standard error of the mean. A negative value in the bar plot indicates a reduction in average maximum dose as compared to the standard arc template. Results for all other anatomical classes can be found in the supporting material (Supplemental Information 1 – 5, Figure 4.6 – Figure 4.10).

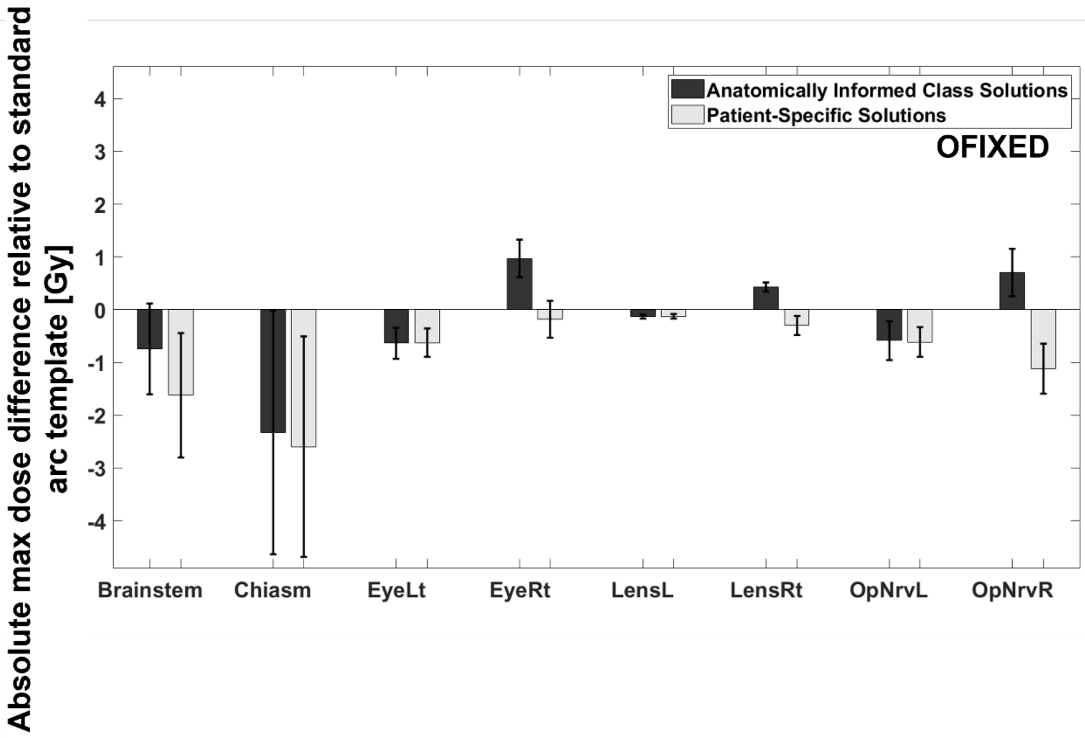

Figure 4.3: The results from anatomically informed class solution (Right Frontal segment). Dark bars indicate the results from the anatomically informed class solution trajectories, while the light bars indicate the results from patient specific trajectories. Dosimetric results are shown when applying trajectories using the OFIXED algorithm.

In the plot of the results from the right frontal segment (Figure 4.3), for five and eight OARs, the OFIXED algorithm generated trajectories lowered maximum dose relative to the standard arc template using the class solution (OFIXEDc) and patient-specific solution (OFIXEDi), respectively.

The results for all anatomical classes are summarized in Table 4.1, where the number of OAR dose reductions is shown based on what planning technique was used.

Table 4.1: Total number of organs-at-risk (OARs) (of the eight considered) that showed maximum dose reductions relative to the standard arc template for the planning techniques used in this work. Mean and standard deviation across classes were rounded to the nearest integer.

	Class 1	**Class 2**	**Class 3**	**Class 4**	**Class 5**	**Class 6**	
OFIXEDc	5	3	5	5	2	2	**4 ± 2**
OFIXEDi	8	3	8	8	7	7	**7 ± 2**

The patient-specific results were almost always at least as good if not better than the class solution, and in approximately 70% of cases, any optimized couch positions outperformed the standard arc template.

4.5.3 Max dose comparisons between arc selection techniques

To perform the multiple independent comparisons that arise from the trajectory selection techniques used in this research, a table was created that accounts for the three comparisons for the 18 specific cases. This table of planning metrics and associated significance values can be found in the supporting material (Supplemental Information Appendix 4.6 – 4.7) but will be summarized based on the objectives of this research.

To compare fixed-couch arc selection to the standard arc template comparisons were performed with the standard arc template, detailed in Table 4.2:

Table 4.2: Number of organs-at-risk (OARs) maximum dose reductions when comparing every planning technique with the standard arc template (N = 18). Significance level Bonferroni corrected to p = 0.00417.

Technique	Number of Max Dose Reductions to OAR	Number of Significant Max Dose Reductions to OAR
OFIXEDc	4	0
OFIXEDi	8	3

When compared to the standard arc template averaging over the 18 independent cases, significant reductions are found for the patient-specific optimization (OFIXEDi). These techniques also reduce maximum dose for each OAR, while class solutions (OFIXEDc) reduced maximum dose to four OARs (not statistically significant).

When comparing the class solution method to a patient specific method, eight OARs achieved maximum dose reductions for the OFIXED comparison but were not statistically significant.

4.5.4 Plan quality metric comparisons between arc selection techniques

Like the max dose metrics shown in Section 4.5.3, the plan quality metrics of V12 Gy, plan MUs, conformity index, and gradient index were compared for all planning techniques independently. In line with the comparison with the standard arc template (Table 4.2), Table 4.3 shows the summary of plan quality.

Table 4.3: Effect on plan quality when comparing every planning technique with the standard arc template (N = 18). Significance level Bonferroni corrected to p = 0.00417. Checkmark indicates meeting the criteria of improvement, X indicates worsening. * Indicates significance threshold met for either improvement or worsening.

Technique	V12 Gy Reduced	Monitor Units Reduced	Conformity Improved	Gradient Improved
OFIXEDc	X	X	√	X*
OFIXEDi	X*	X	√	X

Figure 4.4 summarizes this comparison with the absolute values from each plan.

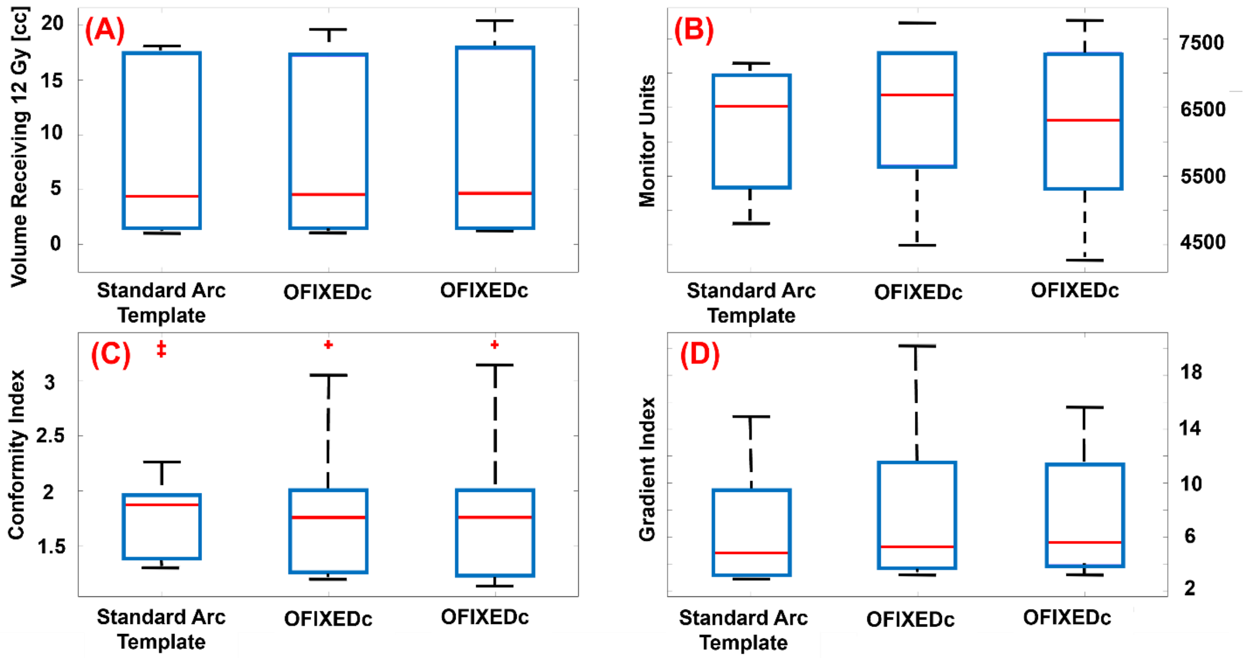

Figure 4.4: The absolute values for each planning technique (Standard Arc Template, OFIXEDc, and OFIXEDi) for V12Gy (a), total plan monitor units (b), conformity index (c), and gradient index (d). Median values are denoted by the solid red lines, while interquartile range is denoted by the surrounding blue box. Upper and lower quartiles are denoted by the dashed lines.

When compared to the standard arc template, conformity index improved in both planning techniques, while all other plan quality metrics favoured the standard arc template, the majority of which were not statistically significant. A significant favouring for the standard arc template was found for V12 Gy compared to OFIXEDi and for the gradient index compared to OFIXEDc.

When considering the comparison between class solution methods and patient-specific methods, class solutions demonstrate superior conformity and V12Gy at the expense of inferior gradient indices. The majority of plan quality comparisons were not statistically significant.

4.5.5 Impact of OAR proximity on class solution effectiveness

An example comparison between two independent plans with considerably different proximity considerations on their respective OARs is shown in Figure 4.5, where a case with many proximal OARs was compared next to a case with no proximal OARs (class 1 versus class 6).

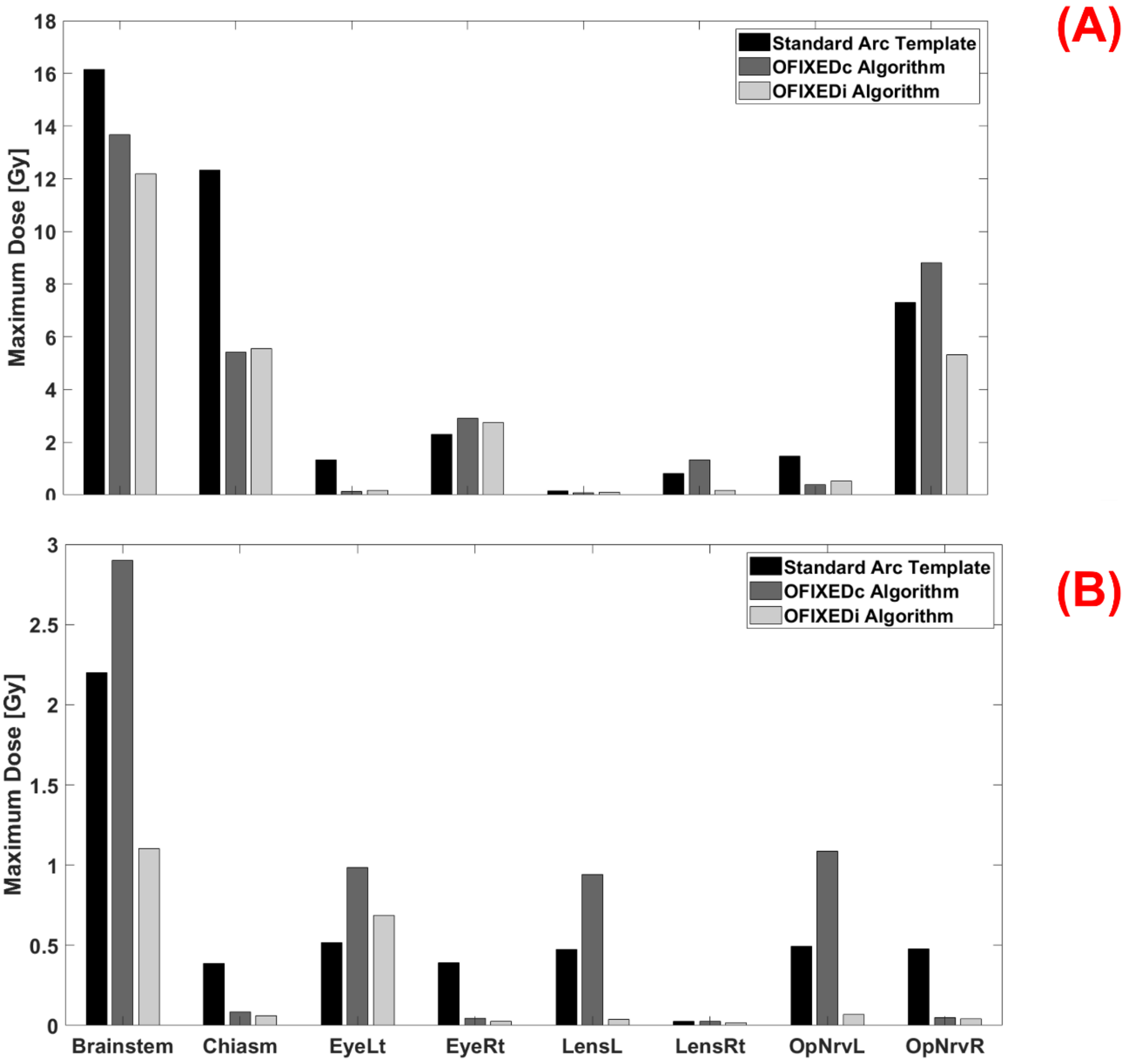

Figure 4.5: A) The raw maximum dose results from a case placed in anatomical class 1 (2 cm diameter spherical synthetic target, right frontal) proximal to brainstem, chiasm, and right optic nerve for all planning techniques. B) Shows a similar plot but from a case placed in anatomical class 6 (1 cm diameter spherical synthetic target, left posterior) not proximal to any organs-at-risk (OARs).

In Figure 4.5A, trajectory optimization relative to the standard arc template reduces maximum dose to OARs brainstem, chiasm, left eye, and left optic nerve. Both brainstem and chiasm were considered as proximal OAR based on Equation 4.1, while only patient-specific trajectory optimizations allow for the reduction of right optic nerve dose. This is contrasted with

Figure 4.5B where various plan optimization techniques yield higher maximum doses to OARs than the standard arc template, that are not proximity constrained.

A table is included in the supporting material that summarizes all maximum dose differences and new significance values based on filtering cases that had proximity constraints (Supplemental Information Table 4.7). Of the 18 independent cases, 11 required considerations of proximity of the PTV to one or multiple OAR. Nine of these were brainstem constraints, four were optic chiasm constraints, and two constraints each for right and left optic nerves respectively. These yielded larger average maximum dose differences for all OAR where proximity was considered respectively but did not change significance.

4.6 Discussion

The aim of this research was to perform a comparison of trajectories from non-coplanar (4π) optimization in the context of developing anatomically informed class solution template trajectories for cranial SRS/SRT. These trajectories were compared to our institutional standard arc template geometry. The purpose here was to demonstrate dosimetric and plan quality differences that arise from variations in arc selection, not planner quality. Therefore, a robust repeatable procedure was used to highlight these differences.

Fixed-couch arc trajectories that conformed to the restrictions of the Eclipse™ TPS were calculated for the dosimetric comparisons. The method for arc selection has been previously compared to the standard four-arc cranial template[5]. Moreover, this comparison was performed using the framework of anatomically informed class solution template overlap maps for six cranial anatomical segments and patient-specific overlap maps. These comparisons provide insight into whether an anatomically informed class solution template informed by optimized fixed-couch arcs is sufficient for cranial SRS/SRT planning.

Synthetic cases simulating single metastases that occur in various parts of the brain were taken as a starting point for developing the anatomically informed class solutions. The aim of this research was not to examine multiple metastases cases, which would involve more complex considerations in the overlap calculations. Comparing arc selection techniques between different regions of interest was facilitated with the flexibility to randomly place a synthetic target inside a known anatomical segmentation, thus allowing for consistent statistics (six classes each with three synthetic spherical targets).

First, when considering Figure 4.1, although the MNI average brain was not completely symmetric, it seemed reasonable to expect mirrored behavior from the lateral dependence of anatomical segments. For example, the overlap maps for classes 1, 3, and 5 (right hand side) should be approximately the flipped versions of classes 2, 4, and 6, respectively. However, the optimized arc trajectories were not simply the flipped versions between classes, implying that there could be differences when performing dosimetric comparisons, and thus a limitation to this method. This could be owing to the nature of the arc selection algorithm navigating the separate overlap maps.

In all cases, dosimetric comparison relative to the standard arc template were calculated as the maximum absolute dose difference. One aspect that this comparison does not account for is the tolerance doses of the OARs used in this research. However, when comparing planning methodologies strictly in terms of maximum absolute dose differences, tolerance doses were not deemed essential to consider. For example, whether a four-arc cranial template plan yielded OARs whose maximum doses were higher or lower than accepted tolerance doses, the comparison with a planning technique that was able to reduce those maximum doses would still be considered relevant for this research.

Evidenced by the example in Figure 4.3 and the summary in Table 4.1, the 4π optimized arc trajectories lead to plans that on average outperformed the standard cranial four-arc template. However, no differences inside each class were significant according to a Wilcoxon signed rank test. Exceptions were found within the standard error for some OARs, indicated by positive values whose error bars did not cross below the zero line. These exceptions were also prevalent in classes 5 and 6 for trajectories generated using the anatomically informed template maps of Figure 4.2E and 4.2F, which occupied the posterior anatomical segment, including the occipital lobe, of the brain (Table 4.1, Supplemental Information Figure 4.9 and Supplemental Information Figure 4.10). Without many OARs to overlap in the BEV due to the larger distances between OARs and targets in these cases (demonstrated by the dark blue bands of Figures 4.2E and 4.2F), it is feasible that the standard arc template would outperform the class solution in both segments. However, the patient specific solutions in these classes all outperformed the standard arc template and the anatomically informed template trajectories (Table 4.1 and Supplemental Information Figure 4.9 and Supplemental Information Figure 4.10). Conversely, as noted in Figure 4.1, there is more potential for BEV overlap when placing a synthetic target in classes 1, 2, 3, and 4 due to increased proximity of OARs and targets.

Classes 1 and 2 occupy the largest segmentations in the frontal region of the brain, where there is more potential for BEV overlap with the optic nerves, eyes, and lenses, and this is reflected by high-intensity yellow bands in Figure 4.2A and Figure 4.2B. Nevertheless, in both cases, trajectories were chosen that aimed to avoid these regions. Classes 3 and 4 occupy the medial regions of the brain where there is more potential for brainstem and optic chiasm overlap. Asymmetries exist between the overlap maps of Figure 4.2C and 4.2D due to differences in the amount of brainstem and chiasm volumes included in the MNI segmentation.

Various levels of maximum dose reduction were measured, however the anatomically informed template trajectories and patient specific trajectories of classes 3 and 4 yielded similar maximum dose reductions compared to the standard arc template (Table 4.1, Supplemental Information Figure 4.7, and Supplemental Information Figure 4.8). This implies that class solutions in the medial anatomical segments could be sufficient for cranial SRS/SRT planning if fixed-couch optimization is performed. This comparison is further evaluated in Figure 4.5, where a case with many proximal OARs was compared next to a case with no proximal OARs (class 1 versus class 6). In this case, class 6 did not require any specialized techniques to lower OAR doses, but class 1 did for all proximal OAR in question.

The amount of maximum dose reduction is also important; taking note of the limits on the vertical axes of Figure 4.3, we see a range of approximately -3 Gy to +1 Gy. The closer to zero that these maximum dose reductions are (e.g., left lens in Figure 4.3), the less consequential it is to choose optimized fixed-couch trajectories, irrespective of whether a patient specific optimization or class solution optimization is being performed. The doses in most cases are already low; however the management of cranial metastases is moving to a situation of retreatment and chronic management; thus any improvement in dose to OARs is advantageous. Whether it's clinically significant in one treatment is not important as the cumulative dose incurred by an OAR is more important.

A limitation of this methodology in comparison to HyperArc$^{\text{TM}}$ [80] concerns the inability for the anatomically informed template to account for multiple targets. This was outside of the scope of this research and would require modification to the initial simulation. Instead of taking the maximum intensity from each overlap map to construct the anatomically informed overlap map, a method would be required to find the most conservative estimate for an overlap map comprised of multiple targets in the same anatomical region. The HyperArc$^{\text{TM}}$ technology[80] does not consider cranial anatomy in its solution, instead it relies more heavily on the VMAT optimizer.

Another possible limitation in our methodology concerns the creation of the class solution overlap maps that use a single (summed) OAR structure that comprised all OARs. This facilitated the calculation for total overlap in a BEV by significantly reducing the computation time compared to an overlap calculation for each OAR separately. With this method, only 243 overlap maps needed to be calculated, while the individual overlap calculation comprised 243 x

8 = 1944 overlap maps, thus increasing computation time from on the order of hours to on the order of days. The number 243 arises from the maximum allowable number of spherical targets that were able to fit in the MNI brain given a diameter of 2 cm, each spaced by 2 cm, and constrained to be entirely contained within the outer contour. Despite this, the individual overlap method of MacDonald *et al.* [30] was used to completely replan and analyze one test case to justify the single OAR methodology, and this yielded similar results to the same case using the single OAR structure methodology (results not shown). It was thus concluded that in general, optimal trajectories for a class solution would be found in similar low-cost regions of an overlap map constructed from a single summed OAR structure or from an overlap map constructed from all the OARs measured separately. Thus, the overlap calculation methodology here differed from MacDonald *et al.* [30] and no individual OAR weightings were applied. For the purposes of developing a set of anatomically informed template trajectories for cranial SRS/SRT, these weightings were not needed, but could be applied in the future to modify the navigation procedures.

Another limitation was this research did not consider how to deal with edge cases in the MNI segmentation. These cases would be where a spherical target could lie across two or more anatomical segments. When performing the segmentation of the MNI brain after filling it with spherical targets, the overlap calculation would be performed only on the portion of the target inside the specified segmented anatomy. However, if the patient-specific target did occupy multiple anatomical segments, it would be unclear what class solution to use. This limitation is readily addressed by performing a 4π optimization on the patient specific map for that case, potentially implying that there is clinical utility in having the option for both an anatomically informed class solution and a patient specific solution. Alternatively, an anatomically informed class solution could be chosen based on which segment the target occupied the most.

A final limitation of the research is that all comparisons to the standard cranial four-arc template[79] begin at a disadvantage in terms of how many control points are given to the Eclipse VMAT optimizer. The OFIXED trajectories were constrained to find at most the best four fixed-couch arcs that spanned an overlap map from top to bottom only once (360 control points where each span 1° of gantry rotation), whereas the standard arc template is not limited in being able to resample gantry angles in 4π space. We are handicapping ourselves in the sense that we are not sampling the space as thoroughly as the template, therefore we expect improvements in conformity and gradient indices if we create other navigation approaches that account for better sampling. This is reflected in the statistically significant superiority of the metrics in favour of the standard arc template in Figure 4.4 and Table 4.3. Nonetheless, the purpose of this research was to compare fixed-couch trajectory optimization in the context of a class solution methodology, which was VMAT optimized with 360 control points, to the standard arc template. Plans that can be optimized with less control points that maintain plan quality while reducing maximum dose, will inherently be delivered more efficiently.

4.7 Conclusion

This research served to present and evaluate a novel methodology for creating anatomically informed class solution template trajectories for cranial SRS/SRT and comparing them with patient specific trajectories. The class solutions were created using the MNI average brain[109], with anatomically informed template trajectories calculated using a modified non-coplanar optimization framework[5]. The arc selection techniques compared in this research vary in terms of their complexity. In approximately 70% of all cases, maximum doses to OAR were reduced relative to the standard-arc template by only changing the arc geometry based on an optimization method. Improvements in maximum dose reduction were further realized when comparing the more complex patient specific optimizations to the anatomically informed class solutions. Furthermore, the most complex method for arc selection (OFIXEDi) showed the largest number of statistically significant differences when compared to the least complex method (VMATi). This could imply a tradeoff between the efficiency and familiarity of a class solution, and the potential for plan quality improvement offered by patient specific arc selection.

4.8 Chapter 4 Appendix

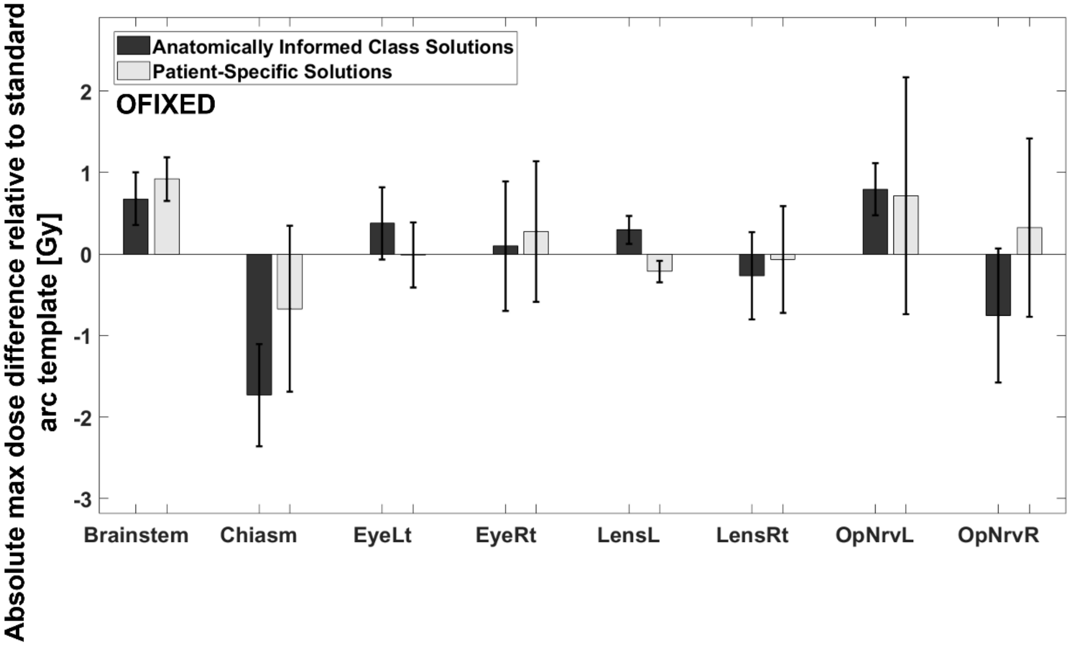

Figure 4.6: Supplemental Information 1: The results from anatomically informed class solution 2 (Left Frontal Segment). Dark bars indicate the results from the anatomically informed class solution trajectories, while the light bars indicate the results from patient specific trajectories. Dosimetric results are shown when applying trajectories using the OFIXED algorithm.

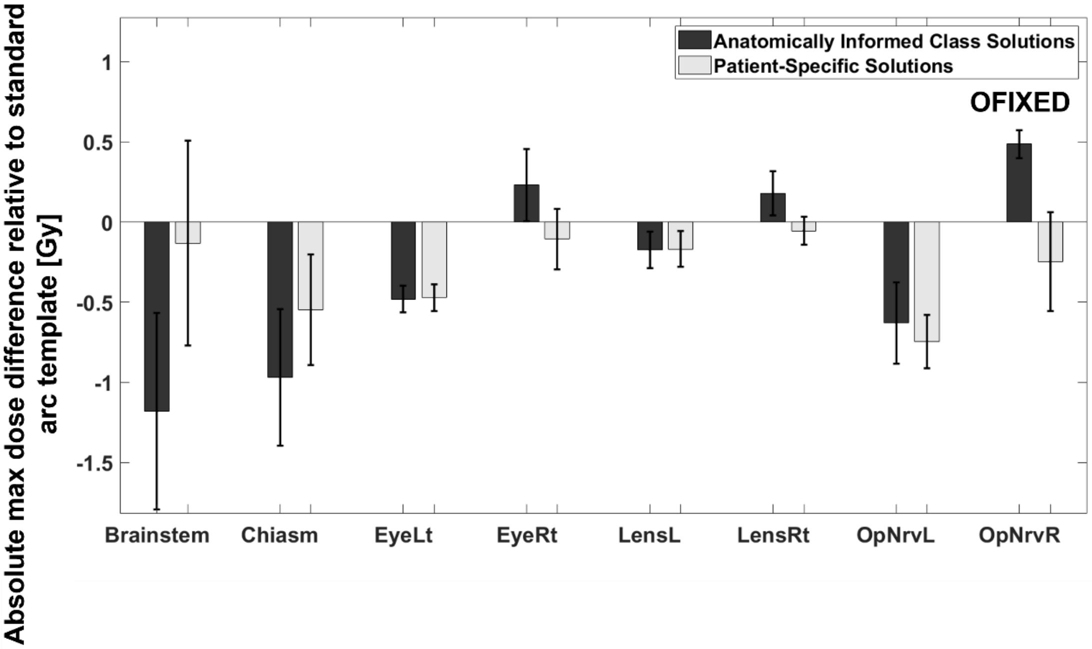

Figure 4.7: Supplemental Information 2: The results from anatomically informed class solution 3 (Right Medial segment). Dark bars indicate the results form the anatomically informed class solution trajectories, while the light bars indicate the results from patient specific trajectories. Dosimetric results are shown when applying trajectories using the OFIXED algorithm.

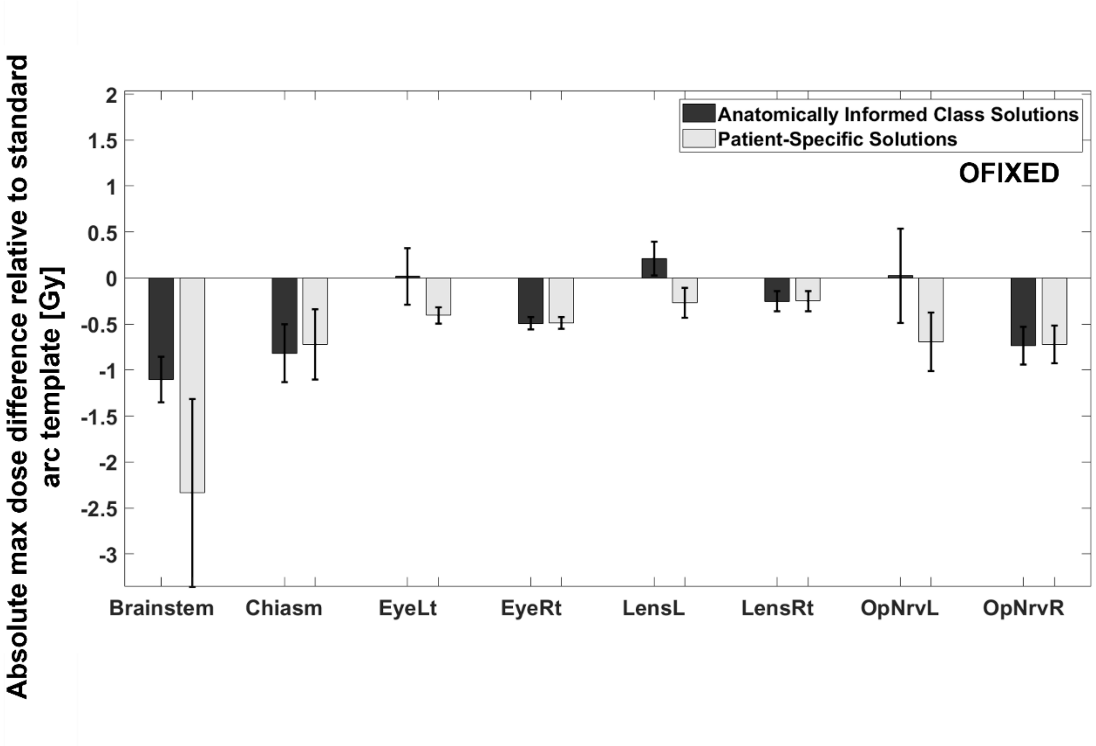

Figure 4.8: Supplemental Information 3: The results from anatomically informed class solution 4 (Left Medial segment). Dark bars indicate the results from the anatomically informed class solution trajectories, while the light bars indicate the results from patient specific trajectories. Dosimetric results are shown when applying trajectories using the OFIXED algorithm.

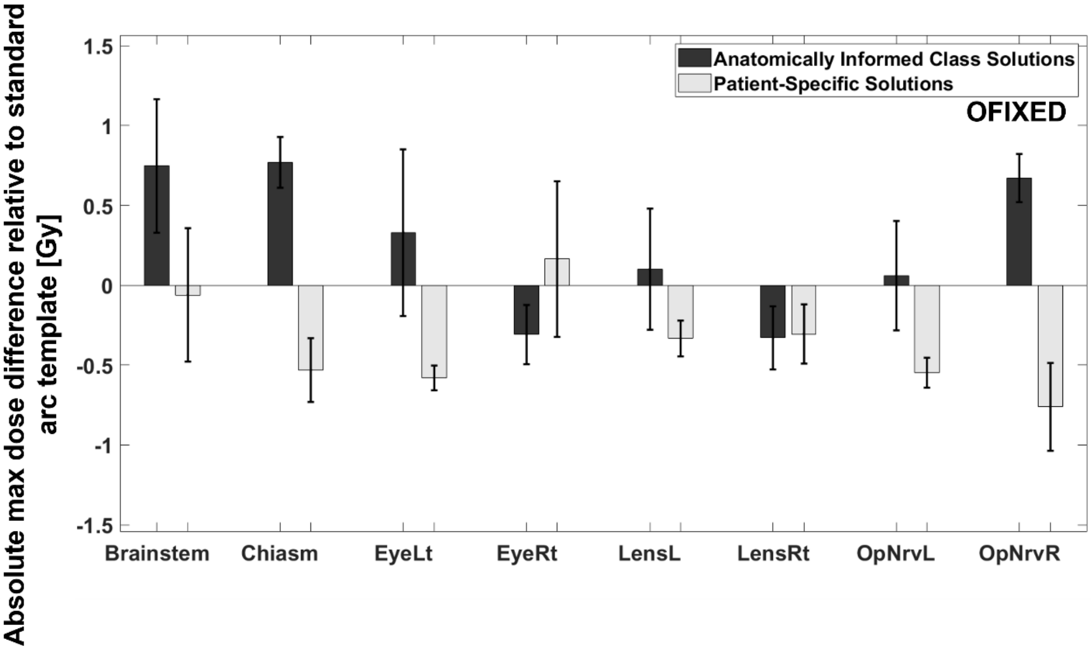

Figure 4.9: Supplemental Information 4: The results from anatomically informed class solution 5 (Right Posterior segment). Dark bars indicate the results from the anatomically informed class solution trajectories, while the light bars indicate the results from patient specific trajectories. Dosimetric results are shown when applying trajectories using the OFIXED algorithm.

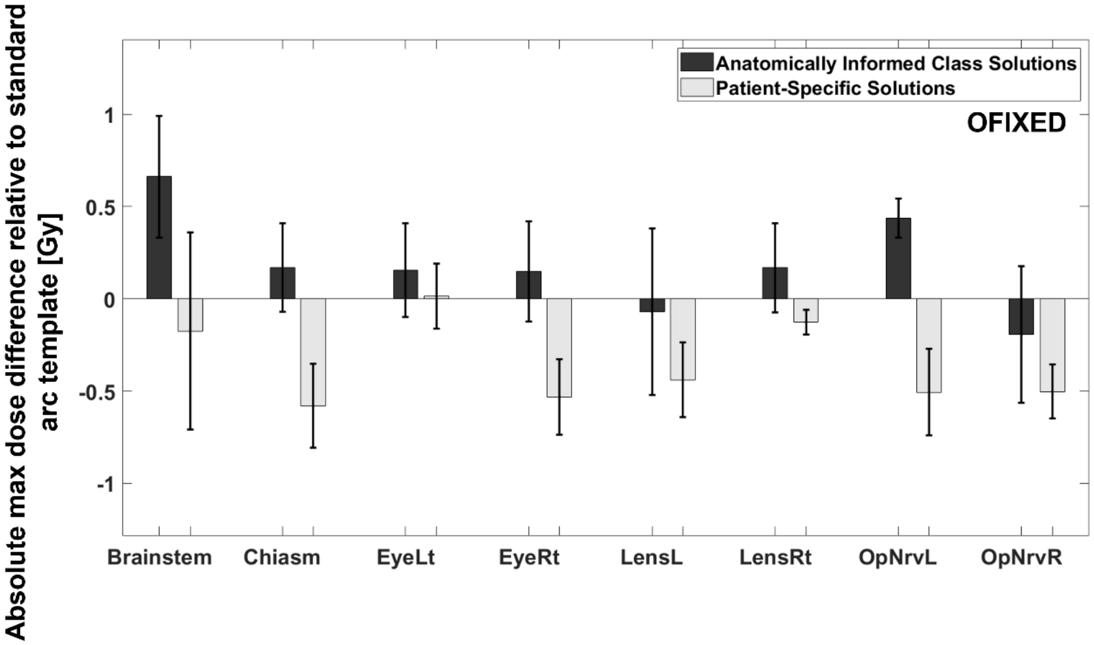

Figure 4.10: Supplemental Information 5: The results from anatomically informed class solution 6 (Left Posterior segment). Dark bars indicate the results from the anatomically informed class solution trajectories, while the light bars indicate the results from patient specific trajectories. Dosimetric results are shown when applying trajectories using the OFIXED algorithm.

Table 4.4: Supplemental Information 6: All plan technique comparisons for all metrics (max dose for all OARs) and plan quality metrics. Colour coding is as follows: all differences are calculated in Gy as (Technique 1 - Technique 2), where blue is positive, and amber is negative. Significance according to the Bonferroni corrected Wilcoxon Signed Rank test accounting for multiple independent comparisons is shown in green for positive significance and red for negative significance.

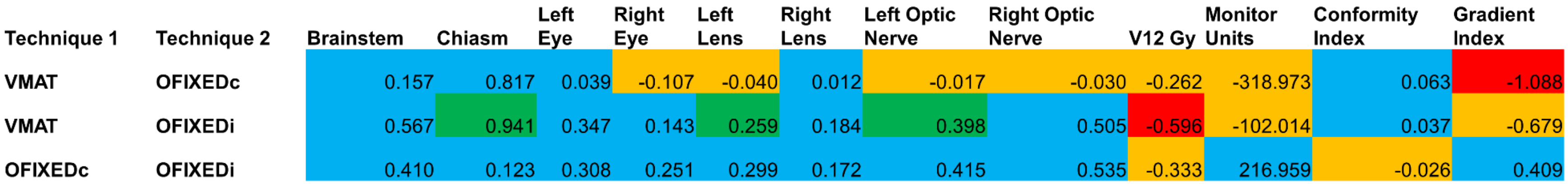

Technique 1	Technique 2	Brainstem	Chiasm	Left Eye	Right Eye	Left Lens	Right Lens	Left Optic Nerve	Right Optic Nerve	V12 Gy	Monitor Units	Conformity Index	Gradient Index
VMAT	OFIXEDc	0.157	0.817	0.039	-0.107	-0.040	0.012	-0.017	-0.030	-0.262	-318.973	0.063	-1.088
VMAT	OFIXEDi	0.567	0.941	0.347	0.143	0.259	0.184	0.398	0.505	-0.596	-102.014	0.037	-0.679
OFIXEDc	OFIXEDi	0.410	0.123	0.308	0.251	0.299	0.172	0.415	0.535	-0.333	216.959	-0.026	0.409

Table 4.5: Supplemental Information 7: All plan technique comparisons averaged for all metrics (max dose for all OARs) and plan quality metrics. Raw significance p-values calculated from a Wilcoxon Signed Rank Test on each of multiple independent comparisons

Technique 1	Technique 2	Brainstem	Chiasm	Left Eye	Right Eye	Left Lens	Right Lens	Left Optic Nerve	Right Optic Nerve	V12 Gy	Monitor Units	Conformity Index	Gradient Index
VMAT	**OFIXEDc**	0.913	0.112	0.647	0.500	0.711	0.983	0.948	0.811	0.029	0.006	0.044	0.002
VMAT	**OFIXEDi**	0.306	0.002	0.005	0.372	0.000	0.012	0.003	0.005	0.001	0.420	0.112	0.016
OFIXEDc	**OFIXEDi**	0.102	0.396	0.215	0.170	0.022	0.071	0.022	0.016	0.006	0.102	0.744	0.679

Table 4.6: Supplemental Information 8: OAR to target proximity information for each plan used in this research. Plan labels are given in the left most column (6 classes each with 3 Targets). Proximity of each target to all OARs in question is given in centimeters.

Plan	Brainstem	Chiasm	Left Eye	Right Eye	Left Lens	Right Lens	Left Optic Nerve	Right Optic Nerve
C1T1	0.17	0.27	>1	>1	>1	>1	>1	0.58
C1T2	>1	>1	>1	>1	>1	>1	>1	>1
C1T3	>1	>1	>1	>1	>1	>1	>1	>1
C2T1	>1	0.38	>1	>1	>1	>1	0	>1
C2T2	>1	>1	>1	>1	>1	>1	>1	>1
C2T3	>1	0	>1	>1	>1	>1	0	0.83
C3T1	0	>1	>1	>1	>1	>1	>1	>1
C3T2	0	>1	>1	>1	>1	>1	>1	>1
C3T3	0.02	0.03	>1	>1	>1	>1	>1	>1
C4T1	0	>1	>1	>1	>1	>1	>1	>1
C4T2	>1	>1	>1	>1	>1	>1	>1	>1
C4T3	0.05	>1	>1	>1	>1	>1	>1	>1
C5T1	0.03	>1	>1	>1	>1	>1	>1	>1
C5T2	0.63	>1	>1	>1	>1	>1	>1	>1
C5T3	>1	>1	>1	>1	>1	>1	>1	>1
C6T1	0.3	>1	>1	>1	>1	>1	>1	>1
C6T2	>1	>1	>1	>1	>1	>1	>1	>1
C6T3	>1	>1	>1	>1	>1	>1	>1	>1

Table 4.7: Supplemental Information 9: All plan technique comparisons for all metrics (max dose for all OARs) and plan quality metrics, filtered by OARs that had proximity consideration given in Supplemental Information 8. The number of plans remaining with a proximity consideration are given in the numbers below the respective OAR columns (e.g.- 9 plans have proximal brainstems according to Supplemental Information 8). Colour coding is as follows: All differences are calculated as (Technique 1- Technique 2), where blue is positive, and amber is negative. Significance according to the Bonferroni corrected Wilcoxon Signed Rank Test accounting for multiple independent comparisons is shown in green for positive significance and red for negative significance.

Technique 1	Technique 2	Brainstem	Chiasm	Left Eye	Right Eye	Left Lens	Right Lens	Left Optic Nerve	Right Optic Nerve	V12 Gy	Monitor Units	Conformity Index	Gradient Index
VMAT	OFIXEDc	0.632	3.324	0.039	-0.107	-0.040	0.012	-0.696	0.240	-0.262	-318.973	0.063	-1.088
VMAT	OFIXEDi	1.059	2.279	0.347	0.143	0.259	0.184	-1.502	-0.248	-0.596	-102.014	0.037	-0.679
OFIXEDc	OFIXEDi	0.427	-1.046	0.308	0.251	0.299	0.172	-0.806	-0.488	-0.333	216.959	-0.026	0.409
		9*	4*					2*	2*				

5 Chapter 5: Static Couch Non-Coplanar Arc Selection Optimization for Lung SBRT Treatment Planning

5.1 Prologue

This manuscript is the result of the extending the cranial algorithms from Chapter 3.2 to extracranial sites described by the methods of Chapter 3.3 and evaluating them in the context of dose reductions to extracranial OARs. This chapter introduces a surrogate dose metric to quantify cost in 4π space and is referred to in this manuscript as "4π cost". The work also presents a novel method for choosing arc trajectories based on a stochastic search, and balances optimization of the trajectory sampling metric mean arc distance (MAD) and 4π cost. VMAT treatment planning was performed on a cohort of 18 patients where optimized non-coplanar arcs were compared with arcs from a clinical arc template. This research serves as the first automated non-coplanar arc optimization methodology for patient specific lung SBRT to our knowledge that is compliant with current regulatory cleared treatment planning systems.

This work has been published in *Physics in Medicine and Biology*.

"Lincoln JD, MacDonald RL, Syme A, Thomas CG. *Static Couch Non-Coplanar Arc Selection Optimization for Lung SBRT Treatment Planning.*" *Phys. Med. Biol.* 2023; 68(15). https://doi.org/10.1088/1361-6560/ace23f.[116]

See Appendix A.2 for copyright permission.

5.2 Abstract

Objective: Non-coplanar arc geometry optimizations that take advantage of beam's eye view (BEV) geometric overlap information have been proven to reduce dose to healthy organs-at-risk (OARs). Recently, a metric called mean arc distance (MAD) has been developed that quantifies the arc geometry sampling of 4π space. The purpose of this research is to combine improved BEV overlap information with MAD to generate static couch lung stereotactic body radiotherapy (SBRT) treatment plans deliverable on a C-arm linear accelerator.

Approach: An algorithm utilizing the Moller-Trumbore ray-triangle intersection method was employed to compute a cost surrogate for dose to overlapping OARs using distances interpolated onto a PDD. Cost was combined with MAD for 100,000 random combinations of arc trajectories. A pathfinding algorithm for arc selection was created, balancing the contributions of MAD and 4π cost for the final trajectory. This methodology was evaluated for 18 lung SBRT patients. Cases were also planned with arcs from a clinical treatment template protocol for dosimetric and plan quality comparison. Results were evaluated using dose constraints in the context of RTOG0915.

Main Results: Five of six OARs had maximum dose reductions when planned with the arc trajectory optimization algorithm. Significant maximum dose reductions were found for esophagus (7.41 ± 0.91 Gy, $p = 0.00019$), trachea (5.56 ± 1.55 Gy, $p = 0.0025$), spinal cord (2.87 ± 1.13 Gy, $p = 0.039$), large bronchus (3.47 ± 1.49 Gy, $p = 0.0075$), and aorta (3.13 ± 0.99 Gy, $p = 0.012$). Mean dose to contralateral lung was also significantly reduced (0.50 ± 0.06 Gy, $p = 0.00019$). There were two significant increases in OAR doses: mean dose to ipsilateral lung (0.40 ± 0.09, $p = 0.00086$) and $V5_{Gy}$ to ipsilateral lung (1.95 ± 0.70 %, $p =$

0.011). Paddick conformity index increased by 0.03 ± 0.02 (p = 0.14), remaining below a limit of 1.2 for both techniques.

Significance: Static couch non-coplanar optimization yielded maximum dose reductions to OARs while maintaining target conformity for lung SBRT.

5.3 Introduction

Stereotactic body radiation therapy (SBRT) is commonly delivered using specialized techniques to facilitate ablative doses to targets, while minimizing dose to surrounding normal tissues. Historically, radiotherapy (RT) techniques have improved due to advances in treatment methodologies from conformal apertures [117] to intensity modulated radiotherapy (IMRT) [118], and subsequently volumetric modulated arc therapy (VMAT) [4]. Upon each of these advances, treatments were better able to reduce maximum doses to organs at risk (OARs) [119-122], increase delivery efficiency (Bortfeld *et al.,*1994; Otto, 2008) or both – in the case of VMAT.

In the last decade, there have been significant developments in expanding the capabilities of RT to further improve OAR sparing while also improving delivery efficiency [22-25,30,35,61,74,123]. In trajectory radiotherapy, or more colloquially known as 4π or non-coplanar radiotherapy, the underlying assumption is that OAR sparing, and delivery efficiency can be improved by choosing optimized trajectories with minimal geometric overlap, and increased sampling of the delivery space. OAR sparing has been correlated with choosing optimized couch and gantry combinations based on geometric overlap scores [22-25,30,100] . When 4π methods are applied, OAR sparing has been realized with IMRT [22,23,123], static couch VMAT [5,100], and dynamic couch and gantry VMAT [24,25,30,74] for a variety of anatomical sites and fractionation schemes. The principal efficiency improvements come from the nature of simultaneously rotating the couch and gantry together, thus covering more 4π sampling in less time [24,25,30,31,74]. Moreover, when there is less overlap with OARs, more conformal apertures can be used which leads to efficiency gains [31].

The framework for our 4π optimization involves cataloguing cost inside the radiation delivery space. For multi-leaf collimators (MLCs) on C-arm linear accelerators our approach is to evaluate cost incurred for using a specific beams-eye-view (BEV) aperture. The measure of overlapping areas of PTV and OARs in 2D projections of the BEV proved preferable in cranial SRS applications [30,124], where maximum dose reductions to the serial OARs are of the utmost importance. However, some OARs in the thoracic and abdominal regions are parallel in their biological response to radiation, where dose-volume quantities must be considered. In addition, the OARs in these disease sites may have larger volumes than those found in the cranium. Considering a cost equation where the cost of overlap relies on a ratio to projected OAR areas, such as that used by MacDonald & Thomas and Yu *et al.* [30,124], may give misleading information for large OARs, such as the lung where the projected area is much larger than the target. In this research, we build on raytracing methods of Meyer *et al*. and Smyth *et al.* [61,74] in combination with the overlap method of MacDonald and Thomas[30] to compute a cost associated with a surrogate for dose through a BEV projection that has overlap with a PTV and OARs. For the purposes of this research, this cost will be called “4π cost”.

Quantification of the degree of 4π sampling has recently been reported in the literature. MacDonald *et al.* proposed a metric called mean arc distance (MAD), that was then used to quantify the relationship with isodose level compactness in the context of stereotactic radiosurgery (SRS) [12]. They found that MAD was able to reliably predict reductions in isodose volumes as a function of decreased MAD in the range of 10% to 100% of the prescription dose.

The purpose of this research is to extend the use of MAD to an extracranial setting, specifically for lung SBRT. Furthermore, it will be combined with a geometric overlap raytracing methodology to ensure the priority of OAR sparing and combined with patient specific collision zones.

5.4 Methods

5.4.1 Overview

The methodology herein follows the structure of the flow-chart shown in Figure 5.1.

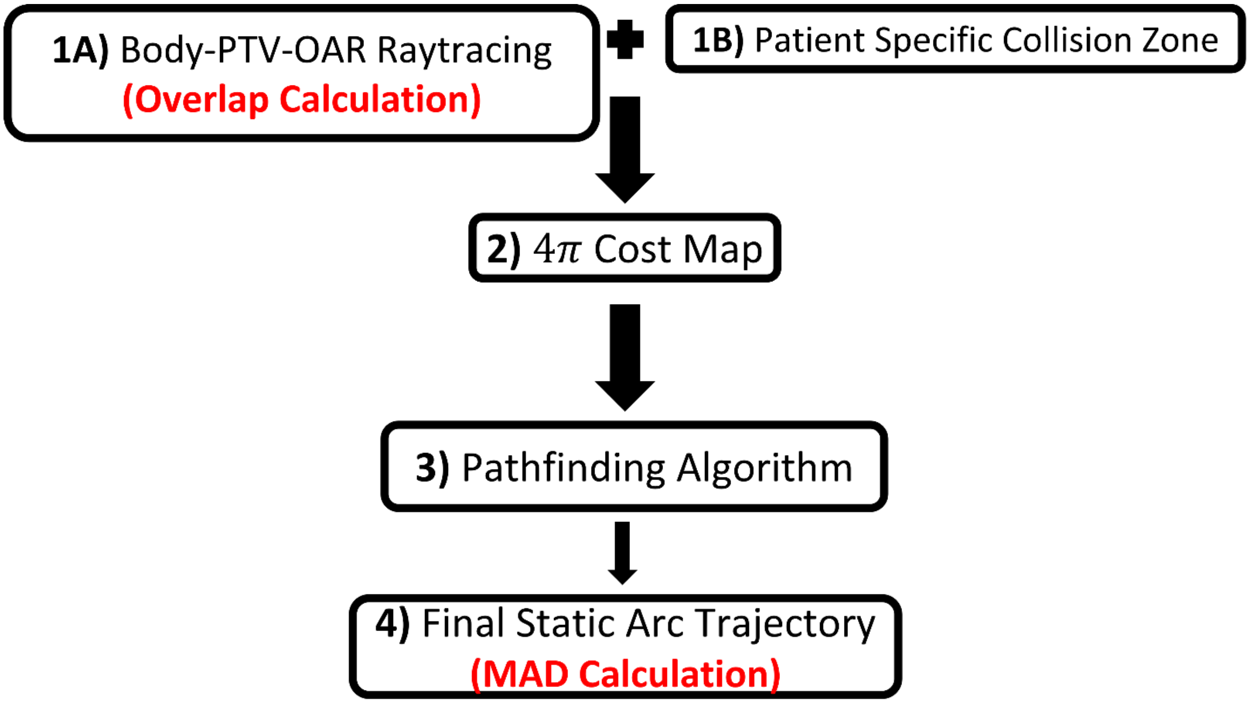

Figure 5.1: A flow chart illustrating the general order that non-coplanar arc selection follows. Labelled in red are workflow locations where geometry and sampling are considered by calculating overlap and MAD, respectively.

1) Body, PTV, and OAR structures are extracted from a treatment planning system (TPS)
    a. These structures are also used to measure a cost metric associated with overlap.
    b. These structures are then used to create patient specific collision zones.
2) Combining the patient specific collision zone with the cost metric, creates a 4π cost map based on overlap.
3) A pathfinding algorithm is applied to generate static couch arc trajectories.
4) For any static couch arc trajectory generated, MAD can be calculated.

5.4.2 Raytracing surrogate dose overlap map generation.

The first step in the workflow was to use a raytracing methodology to compute an overlap-based cost map. The Moller-Trumbore ray-triangle intersection methodology [99] is a computationally efficient way of raytracing that allows apertures containing a broad number of large OARs to be calculated simultaneously. Figure 5.2 summarizes a generalized method for raytracing to compute a cost score in the presence of an overlapping OAR.

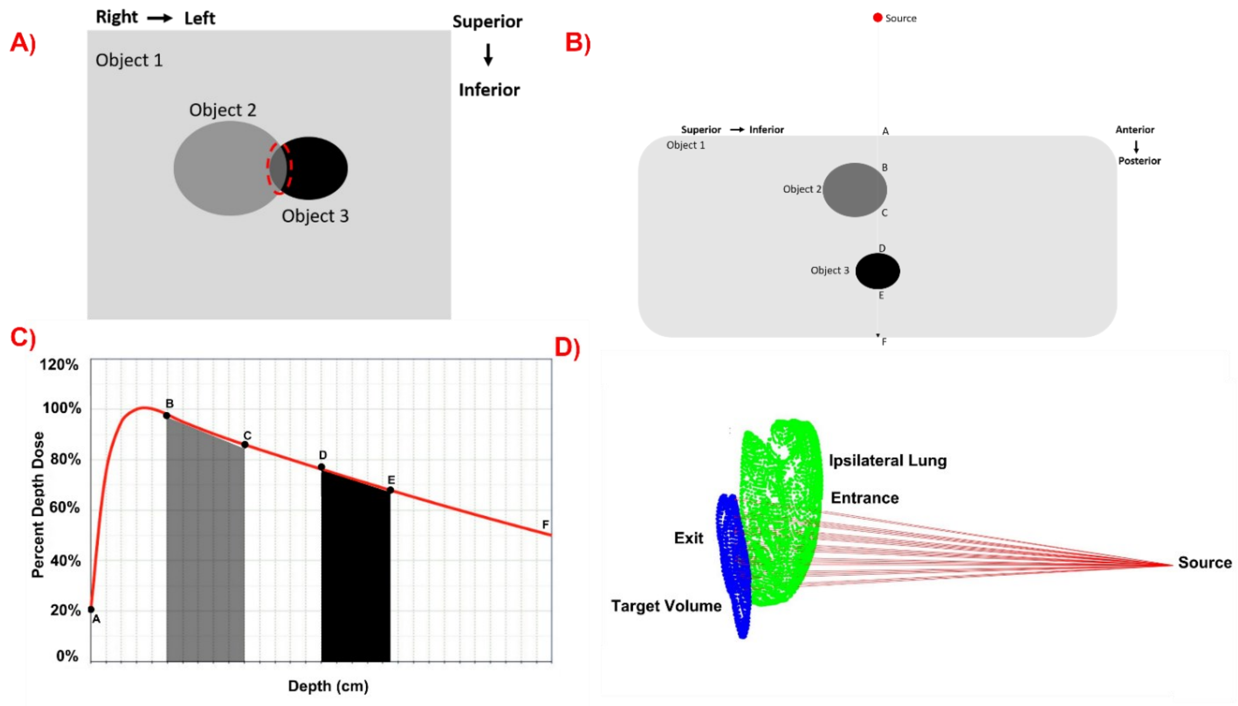

Figure 5.2: Raytracing methodology to calculate a cost associated with every aperture in 4π space. (A) the BEV where there is overlap, object 1 in this case is the body, object 2 could be either PTV or OAR, and object 3 could be the opposite structure. In this example, object 2 is an OAR and object 3 is a PTV. Geometric overlap is indicated by the red dashed line region. (B) is the same scenario as (A) however with the superior-inferior and anterior-posterior views to give 3D context. (C) a percent depth dose curve upon which points of interest were used to calculate a cost score. (D) An example of the methodology applied to a case where the PTV (blue) intersects an OAR (green).

Figure 5.2B shows objects 2 and 3 in a surrounding third (body) structure (object 1). The line from the radiation source through all structures represents a single ray traced. We can then label all ray intersections with each structure, noting that the internal structures can be thought as OAR and PTV in either order. In this example, object 2 is an OAR and object 3 is a PTV:

A. Ray – body entrance point
B. Ray – OAR entrance point
C. Ray – OAR exit point
D. Ray – PTV entrance point
E. Ray – PTV exit point
F. Ray – body exit point

Using these calculated intersection distances, our cost value can be estimated as a crude dose surrogate by interpolating these points on the PDD of Figure 5.2C.

In these experiments, a PDD for a 6 MV photon beam measured at 100 cm SSD with a field size of 10x10 cm^2 was used. This approximation does not account for field size and SSD variability throughout the treatment geometry; however, this simplifying assumption was deemed acceptable as the impact on the calculated dose surrogate will be minimal (< 10%). Figure 5.2C shows corresponding intersection points of Figure 5.2B (A – F). The shaded area under the PDD spanning from point B to point C is given in grey, while the shaded area under the PDD spanning from D to E is given in black. A simplified surrogate for the dose from a single ray irradiation of objects in the BEV overlap region can be thought of as the average dose through the depth of the structures, or the area under the PDD curve. For example, in an anatomical cross section where there is overlap of a large OAR (e.g., lung) relative to a PTV, this will be reflected by a larger area under the curve (AUC) for the larger overlapping structure. Mathematically, a metric was constructed from the information in Figure 5.2C, the raytraced dose surrogate of Equation 5.1.

$$\widetilde{D_R} = \frac{1}{\widetilde{D_R}max}\left(\sum_{i=1}^{n}\sum_{j=1}^{m}\left[\frac{(AUC)_i}{AUC_T}\right]_j\right) \tag{5.1}$$

Where the variables are defined as follows:

- $D_R$max is the maximum value of the raytraced dose surrogate used for normalization.
- n is the total number of rays to be traced.
- i is the index of an individual ray.
- m is the total number of structures.
- j is the index of an individual structure.
- AUC is the area under the PDD curve that has been intersected by the ith ray for the jth structure.
- AUC_T is the total area under the PDD curve.

This quantity was calculated for every combination of couch and gantry position, thus the raytraced dose surrogate can be mapped to a point in 4π space.

Eclipse structures were exported as 3D point clouds as a result of exporting the DICOM structure set. All structures needed to be triangulated to perform the ray triangle intersection. All OARs and PTV were triangulated in MATLAB (R2021a, MathWorks, Natick, MA); and body contours were triangulated using the MeshLab Software [96] due to limitations from the beginning and ending of the CT set leaving holes in the triangulation, especially when a patient's arms were raised. Meshlab was used to close the body surface and make it contiguous. These triangulations were then directly imported into MATLAB to be used for raytracing. An example of the triangulations in both software packages is given in the supplemental information (Supplemental Information Appendix 5.1).

Once all structures were triangulated, 4π cost maps for each OAR were calculated and normalized. Seven OARs were chosen for priority avoidance based on departmental constraints for standardized lung SBRT planning. These constraints are based on clinical end-points described in RTOG 0915 [18] that are used in our clinic. The choice of OARs included in the cost map generation will affect the information in that map and subsequently the arc selection algorithm. However, the methodology is agnostic to the number and types of OARs. Since the PTV is embedded within the ipsilateral lung, the ipsilateral lung was not included in the raytracing 4π cost calculation as it could lead to misleading cost values due to overlap at every couch-gantry angle combination.

In the same way that individual OAR maps were weighted in previous cranial non-coplanar optimizations [29] using QUANTEC dose tolerances [125], weights were applied to each map in this study. The rationale for these weightings concerns increasing the cost of OARs with lower tolerance doses. For this research, each map was weighted according to its lowest dose-volume constraint from RTOG 0915 [18] (see Table 5.1), ensuring a more conservative weighting compared to their maximum dose constraints.

Table 5.1: Weights for individual OARs based on RTOG 0915 dose volume constraints.

Organ-at-Risk	RTOG0915 Constraint	4π Weight
Aorta	V43 Gy < 10 cc	1/43
Esophagus	V18.8 Gy < 5 cc	1/18.8
Contralateral Lung	*Parallel Organ*	1
Heart	V28 Gy < 15 cc	1/28
Proximal bronchial tree / Large Bronchus	V15.6 Gy < 4 cc	1/15.6
Spinal Cord	V13.6 Gy < 1.2 cc	1/13.6
Trachea	V15.6 Gy < 4 cc	1/15.6

Next, the individual cost maps were summed to produce a normalized total map based on Equation 1. Finally, the patient's specific collision zone, using the method previously described [77], was added to the normalized total map.

5.4.3 Novel trajectory generation method to combine MAD and Overlap

Following cost map generation, a pathfinding algorithm was used to generate a final static couch arc trajectory for a given total cost map.

Candidate arcs were generated on each cost map for every couch position by checking for the longest gantry span between collision zones (values of infinity). Choosing the longest gantry span allows the longest possible arcs to be included in the candidate arc set. To expand the candidate arc set to include shorter arcs, virtual collision zones were created to shrink the available space. These virtual collision zones were created iteratively by thresholding, with unique candidate arcs added at each iteration.

By increasing the threshold value to elongate arc lengths, we are necessarily including shorter candidate arcs with lower 4π cost at the lower threshold values. This provides the arc selection algorithm the flexibility to balance short arcs with low cost (which will provide lower

4π sampling) with longer arcs that possibly include slightly higher cost (but higher 4π sampling).

Beginning at a threshold of 5%, any cost greater than or equal to 5% of the cost map maximum value was set as a virtual collision (value of infinity). In this space where the available space had been shrunk, candidate arcs were generated for every couch position by checking for the longest gantry span between virtual collision zones (values of infinity). The number of candidate arcs in the list was expanded iteratively by scaling the maximum cost value threshold from 5% to 100% in increments of 5% and recomputing longest gantry span between virtual collisions for each couch position. This yielded approximately 5000 unique candidate arcs for each cost map at an angular resolution of one degree for both couch and gantry. Unique candidate arcs were determined by excluding any arc that had the same gantry start angle, gantry stop angle, and couch angle.

In the case where the threshold was set to 100% of the cost map's maximum value, the virtual collision zone is equal to the physical collision zone. Figure 5.3 shows an example of the candidate arc selection methodology using increments of 25%.

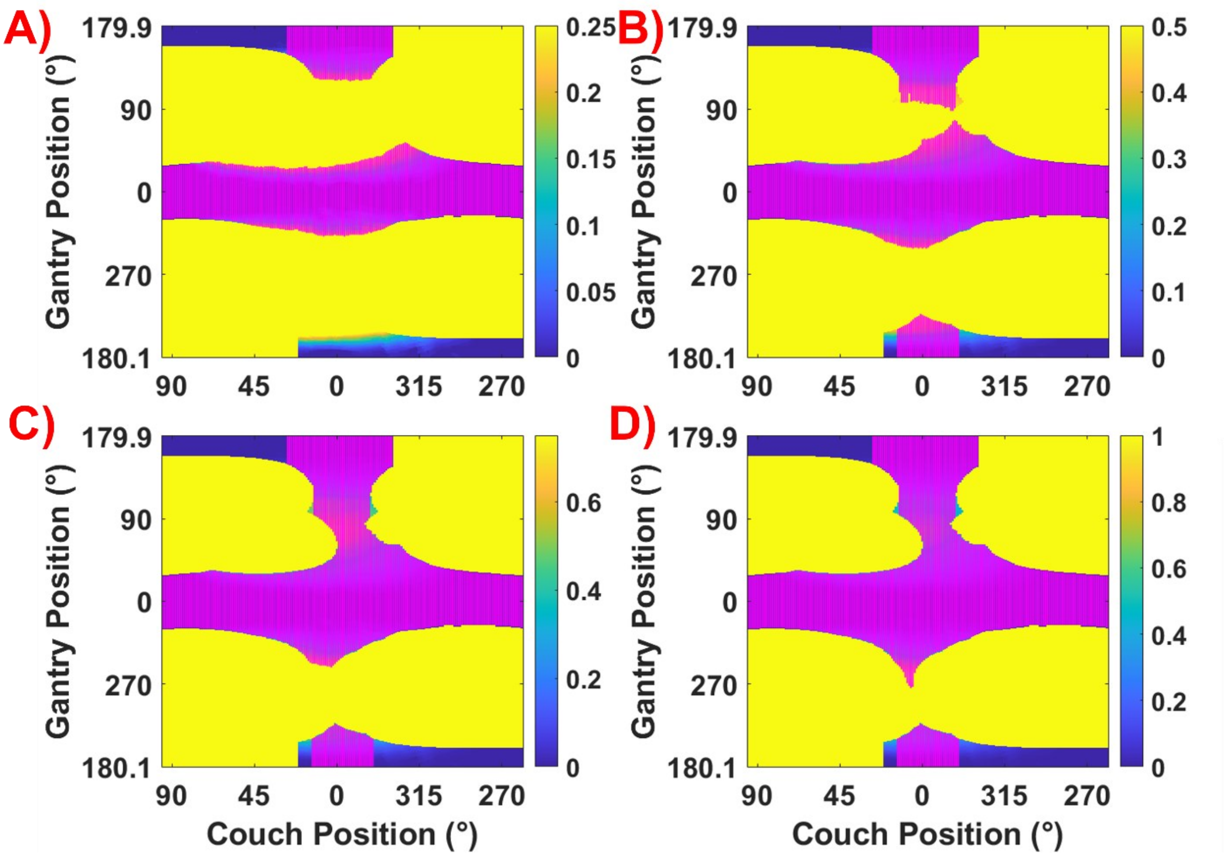

Figure 5.3: Example of thresholding a 4π cost map to infinity at 25% (A), 50% (B), 75% (C), and 100% (D) of the maximum value. Magenta lines represent potential candidate arcs, while yellow regions represent infinite cost. Candidate arcs are plotted at a resolution of 1°.

By thresholding in this way, unique arcs were continuously added to the candidate arc pool until they were generated for the true 4π cost map at 100% of the maximum cost value (Figure 5.3D). Five percent was chosen as the number to increment by in this work to ensure the solution space was adequately sampled while also considering computational efficiency. To make the candidate arcs compliant with the Eclipse TPS any arc less than 30 degrees in gantry span was removed from candidacy. This is a specific limitation of the Eclipse TPS and not necessarily of the proposed methodology. In theory, the concept could benefit from removing the 30°, 10 arc limitation as the number of candidate arcs would expand, giving the stochastic search more opportunity to find trajectories. However, very short arcs may add time to deliver without adding significant sampling.

An optimized solution was calculated by means of a stochastic simulation methodology. For each permutation in the simulation, a random number of sub-arcs was chosen between 1 and 10 (10 being the maximum number of VMAT arcs allowed in Eclipse TPS v.15.6). This number of arcs was then chosen at random from the candidate arc set. The MAD for this arc trajectory was calculated and catalogued with the number of control points (2° per control point) and the 4π cost incurred from that choice of arcs. This method was repeated for 100,000 random permutations which yielded a spectrum of arc trajectories. To achieve a range of control points comparable to the number used in the clinical arc template, an empirical calculation was performed to filter out arc trajectories based on the standard deviation of the number of control points for the 100,000 permutations. The empirical calculation was performed to permit the algorithm to search for high quality solutions with a small number of control points (lower bound) but permit the algorithm to search the higher control point range of the solution space (upper bound). Furthermore, the solution must be clinically feasible, thus requiring that the upper bound is reasonable in attempt to avoid excessively long beam on time and treatment times. This resulted in final arc solutions with an overall number of control points that ranged from 157 to 418 across the entire patient cohort in this study.

The empirical calculation is summarized in Equations 5.2 and 5.3.

$$N_{Lower} = N_{clinical} - \frac{\sigma}{2} \tag{5.2}$$

$$N_{Upper} = N_{clinical} + 2\sigma \tag{5.3}$$

where N_{Lower} is the lower limit of the range, N_{Upper} is the upper limit of the range, $N_{clinical}$ is the number of control points for the clinical arc template equal to 190 (2° sampling), and σ is the standard deviation of the number of control points found across all 100,000 permutations of the simulation.

To choose the optimized arc trajectory from this filtered set, a method herein described as "percentile searching" was performed. The minimum and maximum values of both MAD and 4π cost were used to establish a range in which integer percentiles of corresponding MAD and 4π scores can be calculated. An example considering the problem on a number line is illustrated in Figure 5.4.

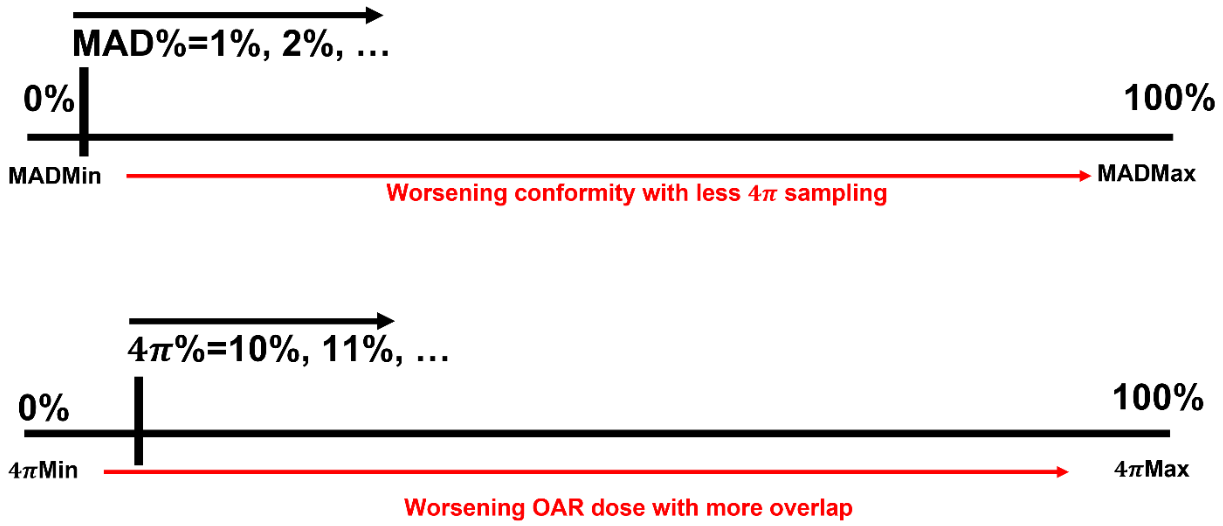

Figure 5.4: Illustration of percentile searching method to balance minimization of MAD and 4π cost.

Starting with all MAD values in the first percentile, the algorithm searches a range of percentiles of 4π scores. An initialization parameter α was chosen to allow the search to be expanded from a specific amount, allowing greater flexibility in the choice of 4π score. The value of the parameter used in this study was 10%. Using this value, the algorithm searches a range of 4π scores from the first to tenth percentiles given the corresponding MAD values in the first percentile. These percentile ranges are defined by Equations 5.4 and 5.5.

$$\text{MAD Range} = \left\{\frac{n}{100}\text{MAD}_{\text{max}} | n \in [1..100]\right\} \tag{5.4}$$

$$4\pi \text{ Range} = \left\{\frac{k+\alpha}{100} 4\pi_{\text{max}} | k \in [1..100]\right\} \tag{5.5}$$

The search range then widens by one percentile for each quantity until a solution was found. There could have been a solution with lower values which might not have been selected, but it would not have a corresponding low enough value for the other quantity. In this way, both MAD and 4π score were minimized together with respect to each other. In the final step of the optimization, if there were multiple solutions found at the same final percentiles, the solution that minimized MAD was chosen. This final patient-specific 4π arc solution was manually imported into the TPS.

5.4.4 Treatment planning procedure

Treatment planning was performed retrospectively for 18 SBRT lung patients (Table 5.2) based on proximity to OARs. Both treatment plans for each patient follow the identical method outlined in this section, with the only difference being the arc geometry.

Table 5.2: Target locations for each of the 18 test patients used in this study including target laterality and target volume.

Test Patient ID	Target Location	Target Volume (cc)
1	Right Upper Lobe	69.0
2	Right Upper Lobe	7.1
3	Right Lower Lobe	9.3
4	Right Upper Lobe	6.4
5	Right Upper Lobe	29.4
6	Right Upper Lobe	65.8
7	Left Upper Lobe	32.9
8	Right Upper Lobe	70.7
9	Left Upper Lobe	53.9
10	Right Upper Lobe	54.7
11	Left Upper Lobe	21.8
12	Right Upper Lobe	20.4
13	Left Lower Lobe	21.1
14	Right Upper Lobe	31.9
15	Right Lower Lobe	26.5
16	Right Upper Lobe	18.6
17	Left Upper Lobe	17.9
18	Left Upper Lobe	12.7

To compare treatment planning techniques using patient-specific 4π solutions, a geometric arc template solution was used as a comparator and is described in Table 5.3.

Table 5.3: Clinical template arc geometry.

Target Laterality	Couch Position (^{o})	Gantry Start Position (^{o})	Gantry Stop Position (^{o})	Arc Direction	Collimator Angle (^{o})
Left Sided	0	350	179.9	CW	15
		179.9	350	CCW	345
Right Sided	0	10	180.1	CCW	345
		180.1	10	CW	15

Independent of target laterality, the arc template spans 190 control points (380^o at 2^o per control point). This provides a rationale for filtering the candidate arc solutions in a range containing that value.

Treatment planning was performed by two medical physicists with extensive experience of clinical SBRT planning. Eclipse treatment planning system version 15.6 was used with versions 15.6 of photon optimizer (PO) and dose calculation algorithm Acuros [126]. Each plan had a prescription dose of 48 Gy prescribed to the 90% isodose level to be delivered in four fractions. VMAT optimizations included normal tissue optimization (NTO) and a final dose grid resolution of 1.5 mm. The OARs evaluated post VMAT optimization were as listed in section 5.4.1. For OARs requiring a PRV (esophagus, trachea, spinal cord), a 5 mm expansion was applied to the respective OAR. These same PRVs were included in the 4π cost map calculation. No OAR dose objectives were used for either planning technique to ensure that differences in dose metrics were due to differences in arc geometry, instead of due to intervention of the VMAT optimizer. The same PTV objectives, optimization objective weights, and plan tuning rings were used for both planning techniques to ensure consistency and reproducibility. A summary of PTV optimization objectives is shown in Table 4.

Table 5.4: PTV optimization objectives used for both planning techniques for standardization purposes with normal tissue (NTO) set to automatic and priority 175.

Structure	Limit	Volume (%)	Dose (%Rx)	Priority
ITV	Upper	0.0	110	200
ITV	Lower	100.0	108	400
ITV	Lower	99.9	108	400
Tuning Ring 1	Upper	0	65	200
Tuning Ring 1	Lower	10	45	200
Tuning Ring 2	Lower	0.0	33	400
PTV minus ITV	Upper	0.0	107	300
PTV minus ITV	Upper	0.1	107	300
PTV minus ITV	Lower	100.0	105	400
PTV minus ITV	Lower	99.9	105	400

The inner and outer dimensions of the tuning rings were defined for Tuning Ring 1 as distances from the edge of the PTV: 1.5 cm to 3 cm, and for Tuning Ring 2 as: 3 cm to 4 cm.

Priorities on PTV and/or tuning rings were modified if needed to assist with low dose spread and target coverage, depending on local anatomy.

5.4.5 Dosimetric and plan quality comparison

Maximum dose metrics and specific dose-volume objectives were evaluated for all OARs. Target metrics of Paddick conformity index (CI) [114] (Equation 5.6), Paddick gradient index [115] (GI) (Equation 5.7), and maximum dose inside the target were also evaluated.

$$CI = \frac{V_{T,ref}}{V_T} * \frac{V_{T,ref}}{V_{ref}} \tag{5.6}$$

where $V_{T,ref}$ is the volume of a target (T) receiving a dose that is equal or greater than a reference dose., where V_T is the volume of the target, and V_{ref} is the reference isodose volume. In this case, the prescription isodose volume was chosen as the reference dose of 48 Gy.

$$GI = \frac{V_{50\%Rx}}{V_{Rx}} \tag{5.7}$$

where the GI is defined as the ratio of the volume of half of the prescription isodose, to the volume of the prescription isodose. In this case, it was the ratio of the volume receiving 24 Gy to the volume receiving 48 Gy.

All metrics were taken from RTOG0915 [18] and are the same as used clinically. An in-house developed ESAPI script was used to extract the relevant DVH metrics from the TPS to a tabular format, with final analysis and statistics performed in MATLAB. Notably, all maximum doses calculated were to 0.03 cc instead of point doses.

Statistical testing was performed by means of the Wilcoxon Signed-Rank test (two-tailed). Comparisons were made between the two planning techniques with a significance level set at $p<0.05$ [127].

5.5 Results

5.5.1 Raytracing surrogate dose overlap map generation

Using the method described in section 5.4.1 the cost maps for an example patient is shown in Figure 5.5. This patient was chosen as it represented a case with a high degree of overlap with OARs implying it was a challenging case where non-coplanar arc trajectories could make a difference.

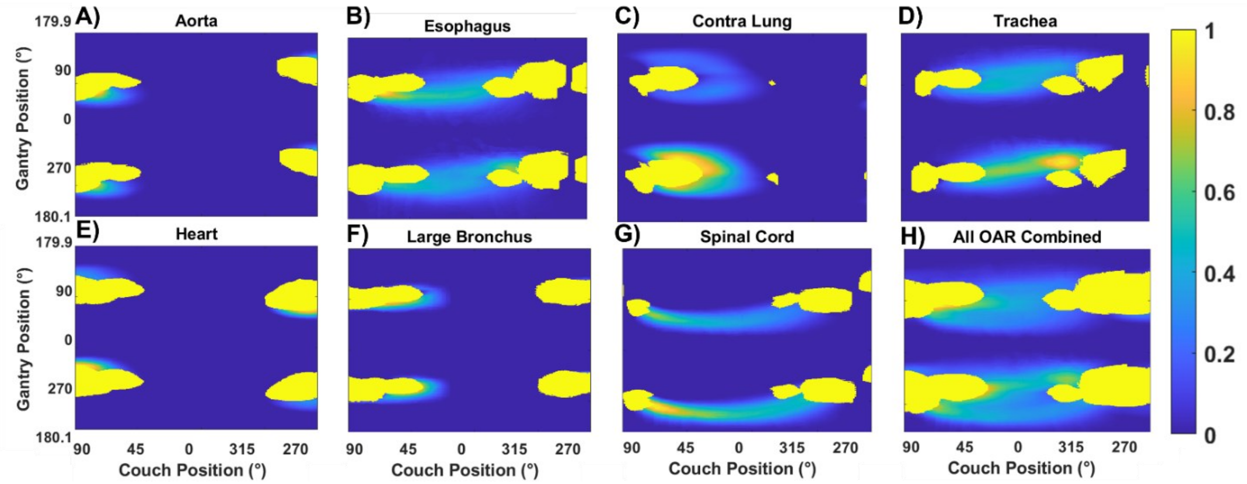

Figure 5.5: All OAR considered during the 4π cost map generation are shown from (A) to (G) with the total map with all OAR combined shown in (H). Gantry angular position is plotted on the verticla axis in IEC 61217 coordinates, while couch angular position is plotted on the horizontal axis in IEC 61217 coordinates. The yellow regions on the map represent the end of the CT set, where delivery cannot occur.

Dark blue regions on the map represent areas of zero overlap. All other colours are representative of non-zero cost values as defined in Equation 5.1.

Once the collision zones are added onto the total 4π cost map of Figure 5.5H, the arc trajectory generation algorithm is applied.

5.5.2 Novel trajectory generation method to combine MAD and overlap

Applying the methodology of section 5.4.2 to the example raytraced 4π cost map of Figure 5H gives the resulting static couch arc trajectory in Figure 5.6.

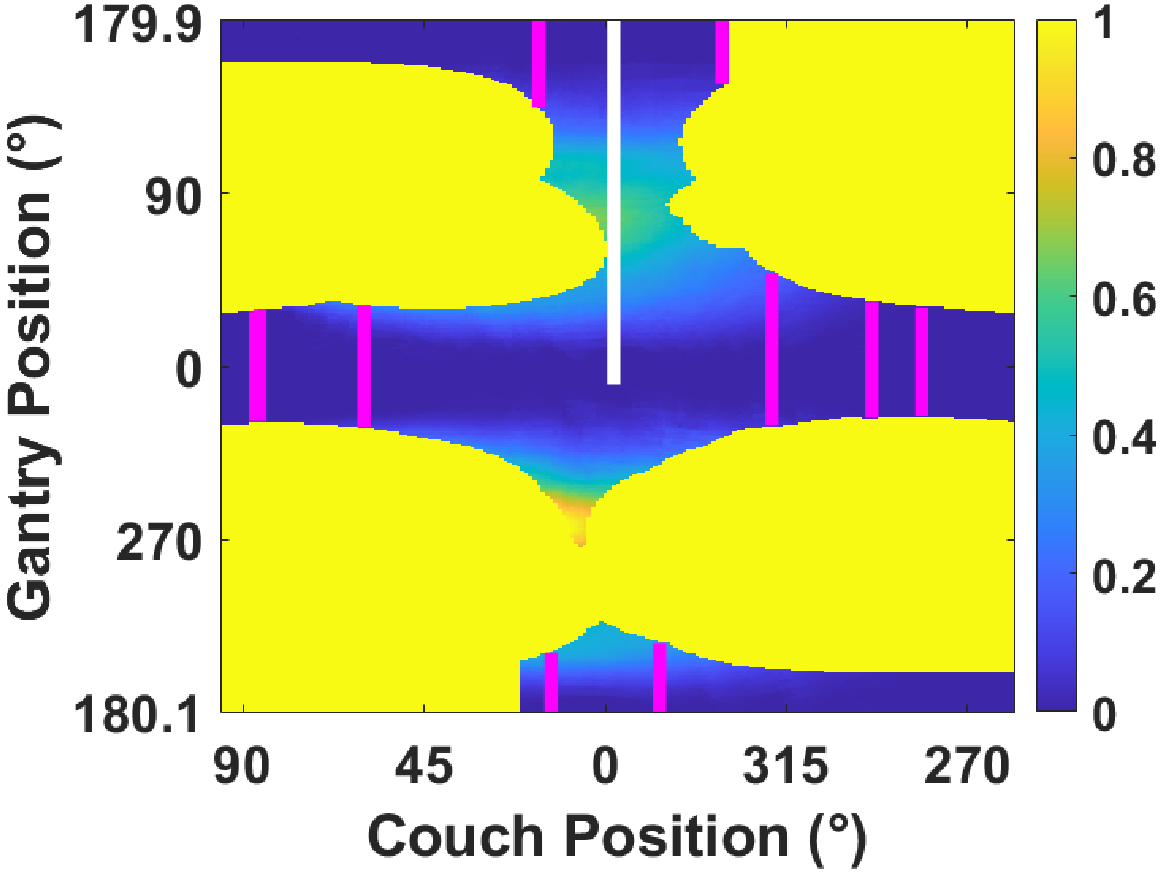

Figure 5.6: Static couch arc trajectory for example patient of Figure 5.5H. Collision zones have been added in yellow with a 3cm safety buffer. The white line shows the clinical arc trajectory, where there are two coplanar arcs of 190 each, one clockwise rotation and one counterclockwise rotation. The magenta lines are the arc trajectory resulting from the combination and balancing between 4π and MAD.

Repeating this optimization procedure for each of the 18 patients yielded unique 18 patient specific solutions (see Table 5.5) which could then be compared against the clinical arc template.

Table 5.5: Summary of patient specific solutions in terms of number of control points, number of arcs with static couch positions, the solutions chosen MAD percentile and the corresponding 4π cost percentile.

Test Patient ID	Number of Control Points	Number of Static Couch Arcs	MAD Percentile	4π Cost Percentile
1	186	7	6	16
2	231	10	5	15
3	157	7	6	16
4	320	9	3	13
5	249	9	3	13
6	256	8	6	16
7	204	8	6	16
8	225	8	6	16
9	266	10	5	15
10	351	10	3	13
11	368	9	3	13
12	418	10	4	14
13	228	9	3	13
14	400	10	3	13
15	240	9	3	13
16	235	8	2	12
17	309	9	3	13
18	291	10	2	12

5.5.3 Plan quality comparison

Table 5.6 presents means and standard errors of the various dose and plan quality metrics used to evaluate the 18 lung SBRT plans in accordance with RTOG0915 acceptance criteria [18]. Plan quality improvements are characterized as reductions in dose relative to the clinical arc template.

Table 5.6: All plan quality metric means and associated standard error, with statistical significance in technique comparison according to a Wilcoxon Signed-Rank test ($p<0.05$) indicated by bold font and the * symbol (N = 18).

Metric	Clinical Arcs	4π Arcs	RTOG 0915 Acceptance Criteria
Conformity Index	1.10 ± 0.16	1.13 ± 0.02	< 1.2
Gradient Index	4.37 ± 0.13	4.67 ± 0.25	n/a
***D$_{max}$ Target [%]**	99.48 ± 0.56	102.49 ± 0.92	< 108.0%
***Monitor Units**	4404 ± 154	5144 ± 157	n/a
Aorta V$_{43\ Gy}$ [cc]	0.00 ± 0.00	0.00 ± 0.00	< 10 cc
***Aorta D$_{max}$ [Gy]**	7.19 ± 1.80	4.06 ± 1.94	< 49 Gy
Bronchus V$_{15.6Gy}$ [cc]	1.03 ± 0.56	0.23 ± 0.15	< 4 cc
***Bronchus D$_{max}$ [Gy]**	14.18 ± 3.35	10.71 ± 3.63	< 34.8 Gy
Esophagus V$_{18.8Gy}$ [cc]	0.86 ± 0.57	0.03 ± 0.03	< 5 cc
***Esophagus D$_{max}$**	13.61 ± 2.37	6.20 ± 2.20	< 30 Gy
Heart V$_{28Gy}$ [cc]	0.49 ± 0.49	0.48 ± 0.48	< 15 cc
***Heart D$_{max}$ [Gy]**	6.20 ± 2.88	7.63 ± 2.99	< 34 Gy
Lung Ipsilateral V$_{11.6Gy}$ [cc]	247.77 ± 25.52	242.47 ± 25.36	< 1500 cc
Lung Ipsilateral V$_{12.4Gy}$	231.96 ± 24.97	226.85 ± 24.47	< 1000 cc
Lung Ipsilateral V$_{20Gy}$ [%]	6.03 ± 0.80	6.21 ± 0.81	< 10%
***Lung Ipsilateral V$_{5Gy}$ [%]**	22.48 ± 1.91	24.43 ± 2.29	n/a
***Lung Ipsilateral D$_{mean}$ [Gy]**	4.30 ± 0.38	4.70 ± 0.42	< 6 Gy
***Lung Contralateral D$_{mean}$ [Gy]**	0.85 ± 0.11	0.35 ± 0.09	< 6 Gy
Spinal Cord V$_{20.8Gy}$ [cc]	0.00 ± 0.00	0.06 ± 0.05	< 0.35 cc
Spinal Cord V$_{13.6Gy}$ [cc]	0.56 ± 0.30	0.74 ± 0.42	< 1.2 cc
***Spinal Cord D$_{max}$ [Gy]**	10.50 ± 1.09	7.63 ± 1.83	< 26 Gy
Trachea V$_{15.6Gy}$ [cc]	3.20 ± 1.61	0.66 ± 0.45	< 4 cc
***Trachea D$_{max}$ [Gy]**	14.37 ± 3.04	8.81 ± 3.05	< 34.8 Gy

The table is organized beginning with target metrics, followed by all OAR metrics in alphabetical order. Averaging the data provides useful information concerning whether the arc selection technique yields an acceptable metric according to RTOG 0915 but may be biased due to variations in target volume of the individual patients. However, a box plot analysis adds further insight to the spread of the data for more detailed comparison.

Figure 5.7 shows maximum doses to 0.03 cc for all OARs and both techniques.

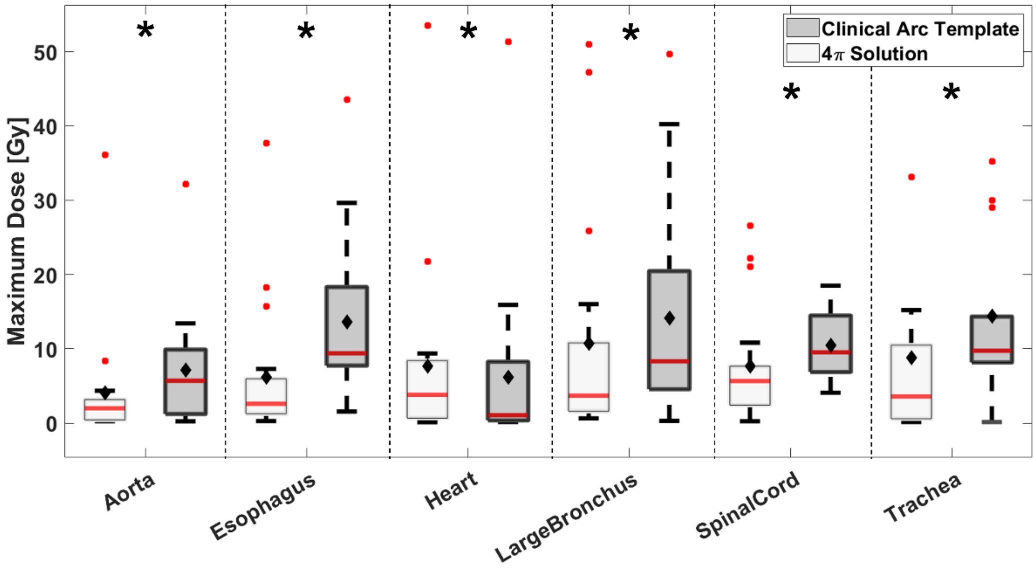

Figure 5.7: Maximum dose to 0.03 cc for six of the OARs considered. Light grey boxes represent the 4π solution, while dark grey boxes represent the clinical arc template. The median is given as the red line inside each box, while the average is denoted as filled black diamonds. Outliers are illustrated with filled red circles. Statistically significant differences are denoted with black stars.

From Figure 5.7, on average the 4π solution reduced maximum dose in five of the six OARs considered. Each of these reductions were statistically significant (see Table 5.6), with the largest reduction seen on average for the esophagus being reduced by an average of 7.41 Gy. The 4π solution increased the maximum dose to heart by an average of 1.44 Gy (7.63 Gy compared to 6.19 Gy), and although this increase was statistically significant, both techniques had maximum doses below the 34 Gy maximum dose constraint for heart. On average, all maximum dose values for both techniques met the acceptance criteria for RTOG 0915.

Figure 5.8 displays the ipsilateral and contralateral lung dose-volume values for each technique.

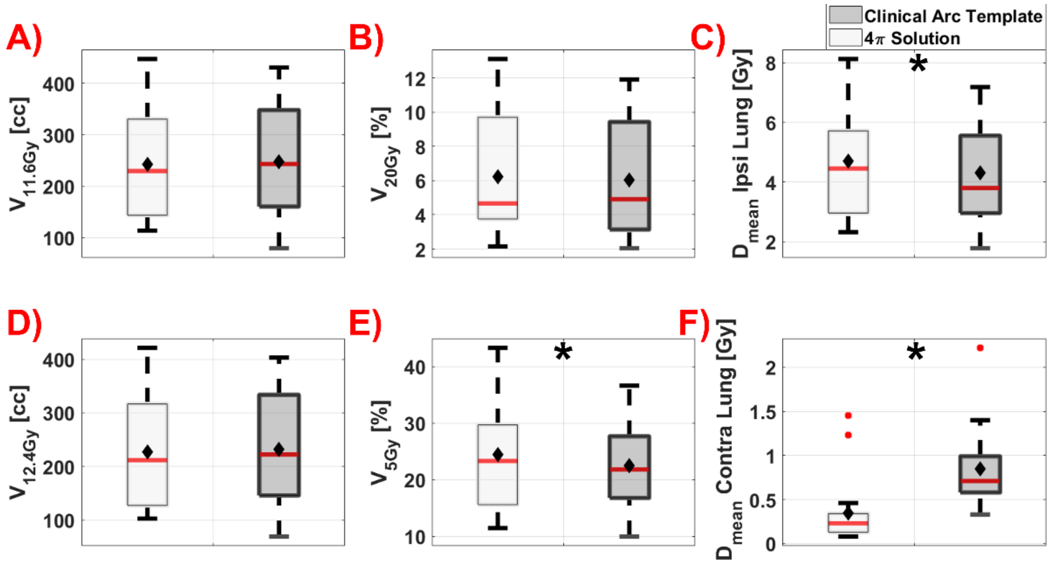

Figure 5.8: Ipsilateral lung dose-volume results for 11.6 Gy (A) and 12.4 Gy (D), with percentages of lung volumes receiving 20 Gy (B) and 5 Gy (E). Mean dose reported for the ipsilateral (C) and contralateral (F) lungs. Light grey boxes denote the 4*π* solution, while dark grey boxes represent the clinical arc template. The median is given as the red line inside each box, while the mean is denoted as filled black diamonds. Outliers are illustrated with filled red circles. Statistically significant differences are denoted as black stars.

From Figure 5.8A and Figure 5.8D, on average the 4*π* solution decreased the volume receiving 11.6 Gy and 12.4 Gy by approximately 5 cc respectively. This difference between techniques, clinical and 4*π*, was not statistically significant according to the Wilcoxon Signed-Rank test (see Table 5.6). From Figure 5.8E, a statistically significant result was found for the 4*π* solution increasing V5 Gy by 1.95%. This will be discussed in further detail in section 6.4. Finally, from Figure 5.8C and Figure 5.8F two statistically significant opposing results were found for the mean dose to ipsilateral and contralateral lungs, respectively. Mean dose to ipsilateral lung increased by 0.40 Gy, while mean dose to contralateral lung decreased by 0.50 Gy.

Non- statistically significant reductions in trachea V15.6Gy, large bronchus V15.6Gy, and esophagus V18.8Gy were realized for the 4*π* solution. Non-statistically significant increases in spinal cord V20.8Gy and V13.6Gy, were found for the 4π solution. The box plot for these results is shown for completeness in the supplemental information (Supplemental Information 5.2).

Figure 5.9 shows an example dose volume histogram (DVH) for the PTV and three selected OARs.

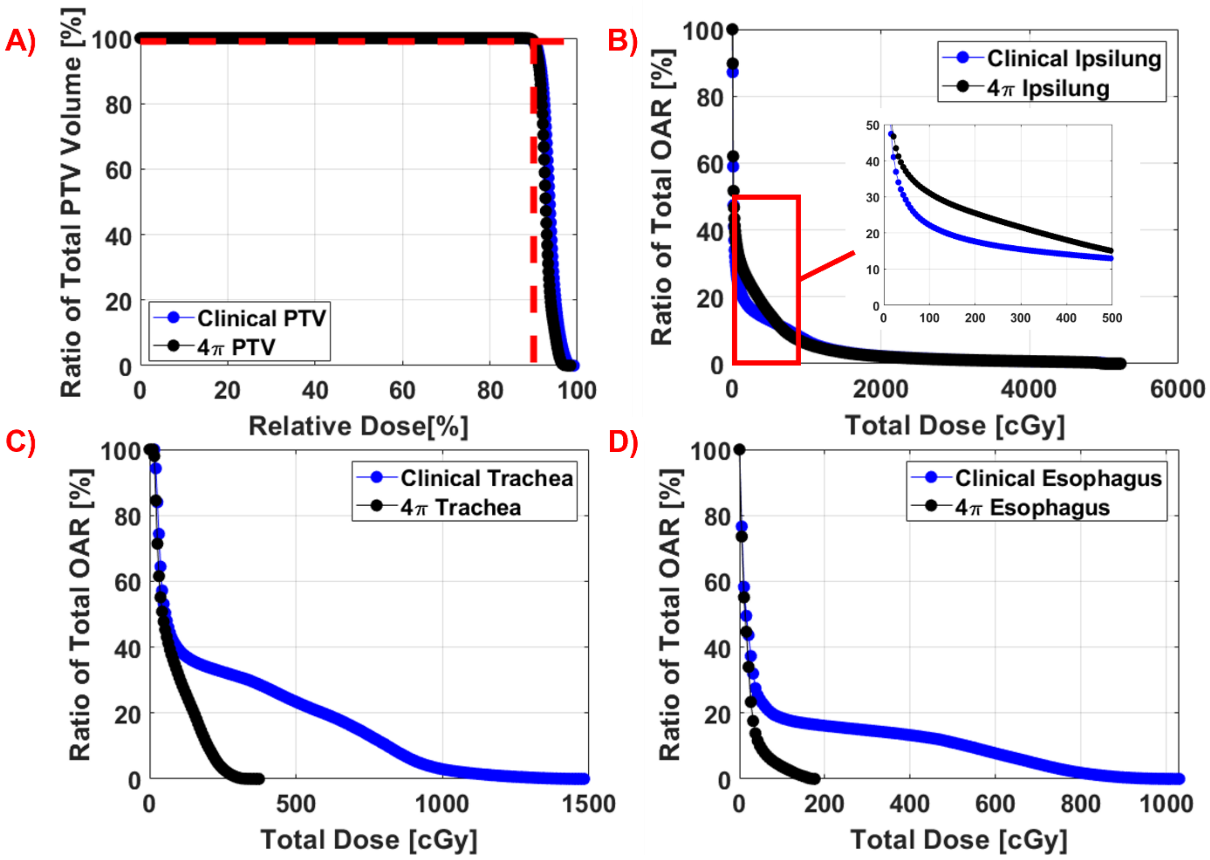

Figure 5.9: Example DVH for PTV (A), ipsilateral lung (B), trachea (C), and esophagus (D). Blue filled dots connected with a blue line denote the DVH for the clinical arc template, while filled black dots connected with a black line denote the DVH for the 4π solution. The red dashed line of (A) shows the normalization point of the prescription dose at 99% volume covered by the 90% isodose. The red box of (B) shows a zoomed in view of the DVH for low doses less than or equal to 5 Gy.

From Figure 5.9A it is readily apparent that comparable PTV coverage was found for this case where blue and black DVH curves effectively overlap. The DVH of Figure 5.9B is also similar between arc selection techniques, except at low doses approximately less than or equal to 5 Gy where the 4π solution is higher. Larger dose differences were found in trachea and esophagus DVH curves for this case, shown in Figures 9C and 9D, where dose reductions were realized for both OARs using the 4π solution.

Figure 5.10 demonstrates the 3D dose distribution for the example case shown in Figure 5.9. Figure 5.10A shows the 15% isodose splaying into both trachea and esophagus contours. Figure 10B shows this same 15% isodose concentrated away from medial OARs. The same behaviour is seen in both coronal and sagittal views comparing Figure 5.10A with Figure 5.10B.

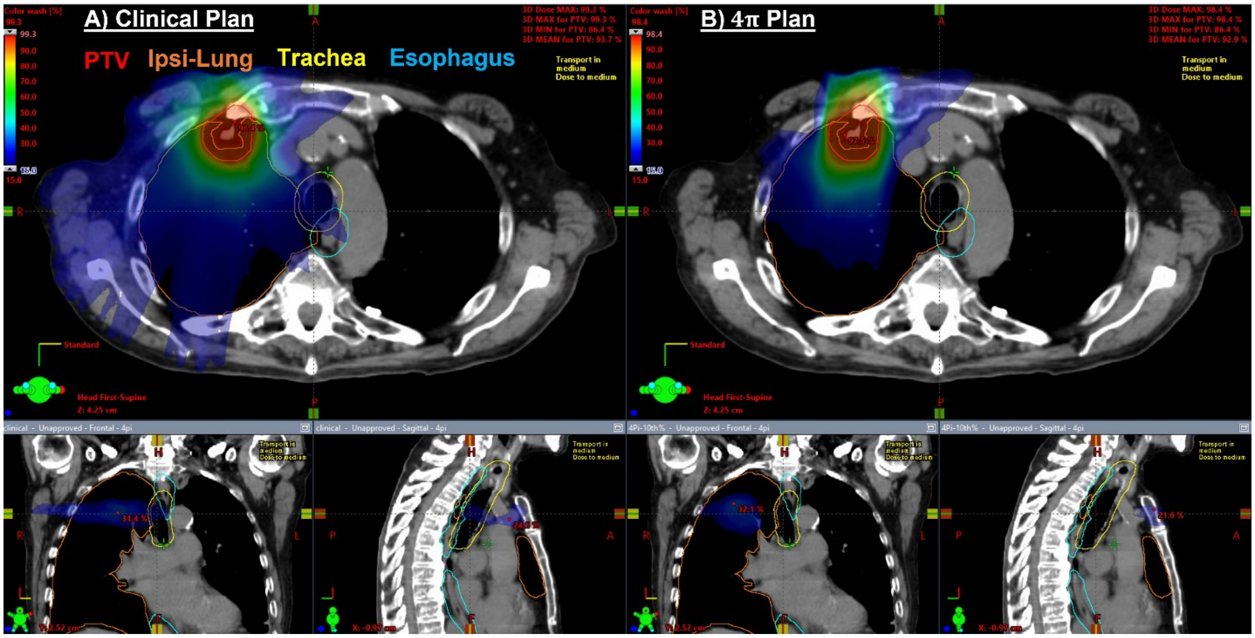

Figure 5.10: Dose distribution for the example case. The clinical plan (A) is shown on the right-hand side and the 4π plan (B) is shown on the left-hand side for the same slices. The same structures as in Figure 5.9 are shown for consistent comparison, with their labels corresponding to their contour colours in the TPS. PTV was contoured in red, ipsilateral lung was contoured in orange, trachea was contoured in yellow, and esophagus contoured in cyan. The lower limit of each dose wash was set to 15%.

Finally, target metrics are presented in Figure 5.11. Two metrics from Figure 5.11 were determined to be statistically significant according to the Wilcoxon Signed-Rank test (see Table

5.6). First was the maximum dose inside the target with an average of 3.00% higher for the 4π solution. Second was the monitor units that averaged approximately 9% higher for the 4π solution. The CI and GI remained comparable between techniques, except for a single outlier for the 4π solution in Figure 5.11A.

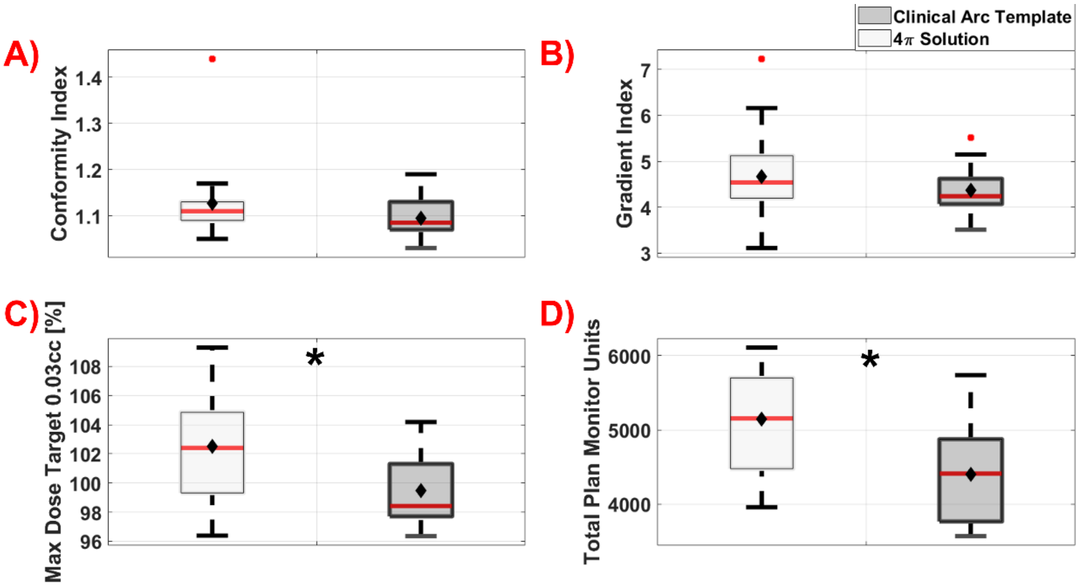

Figure 5.11: Conformity index of target (A), gradient index (B), maximum dose inside target (C), and total plan monitor units (D). Light grey boxes denote the 4π solution, while dark grey boxes represent the clinical arc template. The median is given as the red line inside each box, while the average is denoted as filled black diamonds. Outliers are illustrated with filled red circles. Statistically significant differences are denoted as black stars.

5.6 Discussion

This research presents a method of creating 4π cost maps to be used in extracranial trajectory radiotherapy applications. Specifically, this method was combined with a novel pathfinding procedure and patient specific collision zones for lung SBRT treatment. This method was compared to an arc template that is currently used in our clinic for treating lung SBRT. One of the main purposes of this research was to offer a methodology that can be easily translated into clinical practice. Moreover, the method is generalizable to any anatomical site by modifying the OARs considered and their respective dose tolerance weighting factors.

Although a generic PDD was used, the impact on the dose surrogate is not strongly dependent on SSD or field size. An experiment was performed using a 6 MV beam incident on a homogeneous water phantom inside the TPS to generate various PDDs. PDDs were created at 75 cm and 95 cm SSD with field sizes of 4 x 4 cm^2 and 20 x 20 cm^2. All PDDs were extended to the same depth to ensure the PDD integration was unbiased. Three depth ranges of 5 cm to 10 cm, 10 cm to 15 cm, and 15 cm to 20 cm were examined for a 5 cm thick target. 4π cost scores were then calculated resulting in a maximum discrepancy of 7.3%. These discrepancies represent an upper limit on the impact since other factors are included in the 4π cost function. Moreover, these are raw value discrepancies that may be reduced further when the overall 4π cost map is normalized. This implies that there is unlikely to be a significant impact of SSD and field size on the final arc selection.

The impact of tissue specific heterogeneities (e.g., lung, bone) were not considered to maintain computational efficiency, however they could be incorporated into a future version of the algorithm. The impact of such a correction on arc selection is not known.

Furthermore, the 4π cost map sums the cost for several intersecting rays. There is a dependence on the geometrical shape of the structures in the overlapping region and the number of rays used. Larger overlap regions will have more rays traced through them and thus a potentially higher 4π cost. To ensure the number of rays did not bias the solution, the 4π cost score was normalized by the maximum value on the 4π cost map before applying the OAR specific weighting factors. These weights were implemented without dose-volume considerations, and instead the most conservative dose constraint for each OAR were applied to its entire map.

Literature on non-coplanar lung SBRT includes Dong *et al.* (2013a) who showed significant max dose reductions to OARs using 7 to 9 field IMRT. On average with a cohort of 12 patients, they were able to reduce doses to heart, esophagus, trachea, bronchus, and spinal cord relative to coplanar eight field IMRT. In that study, VMAT (RapidArc) with two full coplanar arcs was also studied and found to be dosimetrically comparable to the clinical IMRT plans. This supports our maximum dose data from Figure 5.7. Moreover, the lung volume metrics cited in that work were lower than what was found in Figure 5.8 of our research. These authors also quote improved target coverage by means of improved minimum dose to the PTV. Upon escalation to 70 Gy, they were able to cover 95% of the treatment volume with at least 68 Gy. On average in our work, Figure 5.11A shows a comparable CI to the clinical arc template, with conformity defined by 100% of the prescription dose covering 99% of the target volume, proving OAR sparing is possible while maintaining conformity.

The balancing of MAD and 4π cost in the navigation optimization was a trial-and-error process to ensure that neither dominated the optimization. If the 4π cost was weighted higher than the MAD cost, we found superior maximum dose sparing to OARs at the expense of poorer CI (results not shown). Conversely, if the MAD cost was weighted higher, excellent target conformity was achieved at the expense of increased maximum doses to OARs (results not shown). Therefore, a balance between minimizing both at the same time was needed and found for an α value of 10%. The pathfinding arc trajectory optimization presented in this research is the result of these findings: a method to balance the trade-off between target conformity and OAR sparing in a patient-specific manner.

As discussed in the methodology, OAR constraints were not applied to the treatment planning in general to ensure that plan quality metric statistics were biased as little as possible by the VMAT optimizer. The objective was to quantify the dose reductions as a result of only changing arc geometry. Previous research where OAR objectives were included yielded dose reductions for optimized geometries in realistic conditions [5,30,100,128]. In this research, we aim to demonstrate the potential gains made due to arc geometry alone for the entire patient cohort. On average for the cohort of this study (N = 18), all plan metrics were deemed clinically acceptable. In cases where this did not occur for a specific OAR, it was found that putting optimization constraints on the OAR in question during VMAT optimization was able to bring the constraint below tolerance as would be done in clinical practice. An example is given for the spinal cord as an OAR which had failing plan quality metrics for the 4π solution in three cases. As would be done in institutional specific clinical practice, a tuning structure was created for the spinal cord for each case, with an upper objective on the dose constraint. Here the upper objective was 0% of the tuning structure volume could receive no more than 1300 cGy. For unbiased comparisons of these three cases, the 4π solution and clinical standard solutions were both replanned using a tuning structure created with the same methodology to observe effects on plan quality even if the case had not failed for both planning techniques.

Table 5.7: Spinal cord metrics before and after applying OAR objectives to VMAT optimization in cases where no objectives yielded failing dose metrics.

Patient	Dose Metric	4π No Objective	4π With Objective	Clinical No Objective	Clinical With Objective
1	D_{max} (0.03 cc) < 26 Gy	26.56	14.27	18.50	14.51
	$V_{20.8}$ Gy < 0.35 cc	0.94	0.00	0.00	0.00
	$V_{13.6}$ Gy < 1.2cc	5.96	0.42	4.79	0.39
	Conformity Index	1.17	1.13	1.07	1.05
5	D_{max} (0.03 cc) < 26 Gy	22.15	15.89	14.47	13.86
	$V_{20.8}$ Gy < 0.35 cc	0.15	0.00	0.00	0.00
	$V_{13.6}$ Gy < 1.2cc	2.78	1.00	0.11	0.06
	Conformity Index	1.17	1.13	1.15	1.06
9	D_{max} (0.03 cc) < 26 Gy	21.07	13.87	18.16	12.40
	$V_{20.8}$ Gy < 0.35 cc	0.06	0.00	0.00	0.00
	$V_{13.6}$ Gy < 1.2cc	4.65	0.07	1.61	0.00
	Conformity Index	1.11	1.10	1.09	1.10

When both techniques were reoptimized with additional OAR constraints, the gains in sparing were comparable with the tuning structure objective contributing to dose reductions for almost all metrics. With a comparison like this it is difficult to discern the extent to which differences in plan quality occurred due to modulation or arc geometry.

The lung metrics shown in Figure 5.8 illustrate comparable plan quality between the 4π solution and clinical arc template. As the contralateral lung was included in the 4π cost maps, it is feasible to assume that reductions relative to the clinical arc template should be realized. This result was found in Figure 8F with a reduction on average of 0.50 Gy to the contralateral lung, potentially important when considering the importance of dose reduction to avoid radiation pneumonitis [18]. Conversely, the ipsilateral lung was not considered in the 4π cost maps, and an increase in mean dose was found on average of 0.40 Gy. In future studies, it may be important to incorporate methodologies that may also reduce dose to ipsilateral lung.

On average, the spread of dose volume and maximum dose values to OARs was reduced through our methodology as compared to the clinical template. This indicates that the 4π and MAD balanced solution results in a more consistent final plan across patients than the clinical template. In other words, a patient-specific solution produces a more consistent result than a general solution.

A limitation of this study is a lesser focus on the efficiency of delivery of the 4π solution. Like previous studies involving many-port IMRT plans, [22,23,123,124] the current work would add additional time to a treatment due to the number of arcs. A future clinical environment may reduce this limitation using automated couch motions between arcs. To make treatments more efficient, literature has proposed continuous couch motion [24,25,30,35,74], and methods to reduce the total number of monitor units [31]. Further studies will investigate efficiency, which must also be weighed with OAR sparing and target conformity.

However, the purpose of this research was to present a methodology for 4π non-coplanar optimizations in lung SBRT by creating a cost associated with arc spacing (MAD) and overlap (4π cost). The combination of these metrics allows for the balance between target conformity and dose sparing to be considered in the plan geometry stage of treatment planning. Although all optimizations in this research were limited to static couch, extending this framework for dynamic axes is the subject of future work.

5.7 Conclusion

This research presented and evaluated a methodology for the treatment of lung SBRT using static couch non-coplanar arcs. A raytracing method was developed to account for the cost of considering large OAR in extracranial radiotherapy and was combined with MAD to create a stochastic arc trajectory pathfinding algorithm. Overall, maximum dose to OARs was reduced, in some cases significantly, while maintaining similar target conformity to a geometric template that is used in clinical practice. The solutions presented have been purposefully created to facilitate ease of clinical translation.

5.8 Chapter 5 Appendix

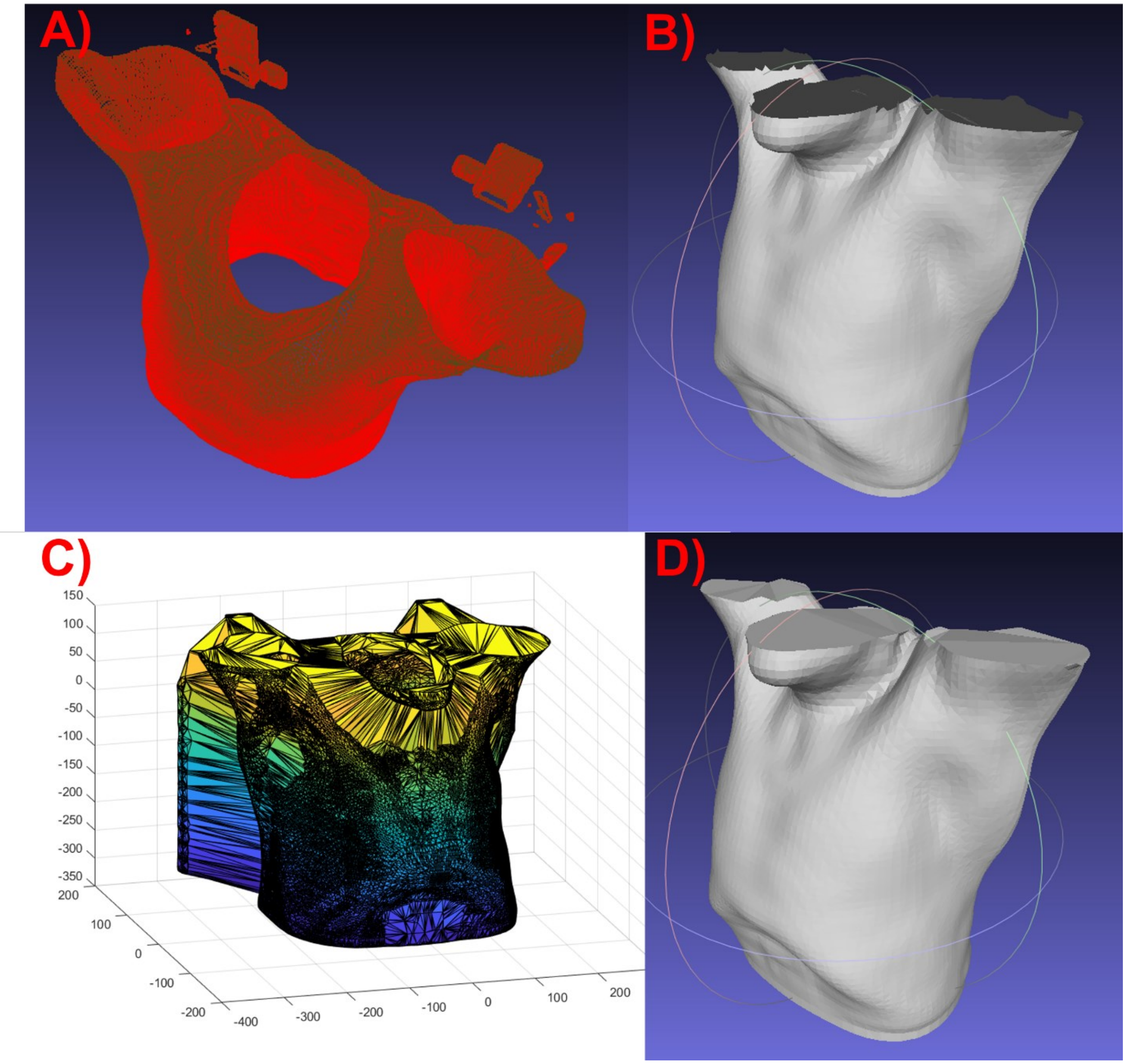

Figure 5.12: Supplemental Information 5.1: (A) Shows the vertices requiring preprocessing which can be manually removed in MeshLab. (B) Shows the reconstructed faces after down sampling with poisson surface reconstruction. (C) Shows the reconstruction with MATLAB's boundary function where manually removing the vertices shown in (A) was deemed a limitation of only the body contour and not the PTV and OAR contours. (D) The final reconstructed triangulation using MeshLab's ability to fill holes in specific regions.

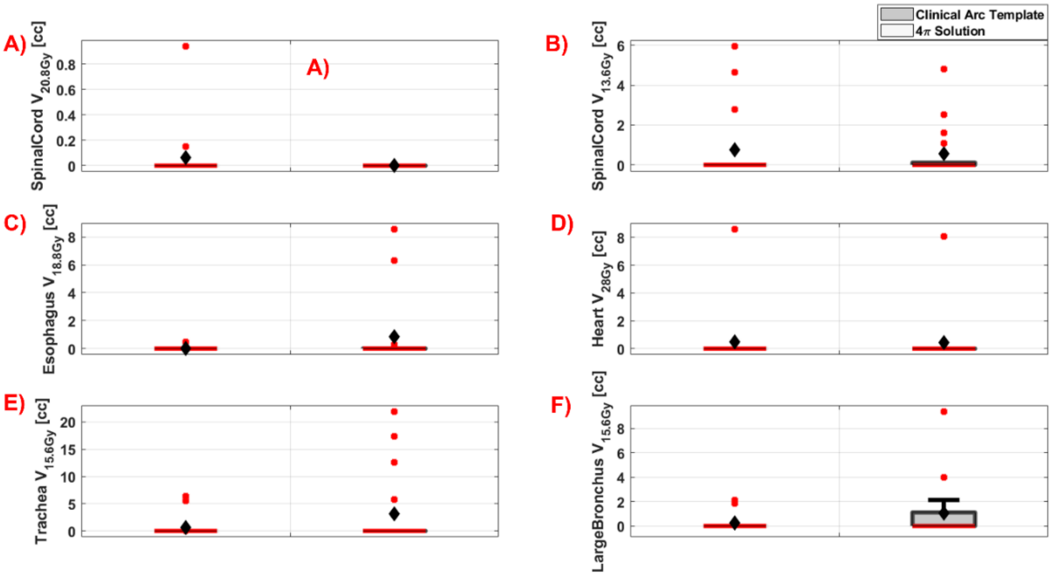

Figure 5.13: Supplemental information 5.2: Additional dose volume results for spinal cord (A and B) esophagus (C), heart (D), trachea (E), and large bronchus (F). Light grey boxes denote the 4π solution, while dark grey boxes represent the clinical arc template. The median is given as the red line inside each box, while the mean is denoted as filled black diamonds. Outliers are illustrated with red circles.

6 Chapter 6: Biologically Optimized Non-Coplanar Arc Selection for Small vs. Large Target Volumes in Liver SBRT

6.1 Prologue

This manuscript is an extension of the extracranial methodologies of Chapter 3.3 and Chapter 5 to the liver, which is another common site for SABR. Biological considerations are made to OARs specific to their serial or parallel nature. Specific considerations are also made for the liver that encompasses the PTV at every BEV as overlap will always occur. Furthermore, delivery efficiency limitations are addressed as a trade-off in the stochastic arc selection process to choose high quality arc solutions with a low number of arcs, high degree of arc spacing (MAD), and low BEV cost. VMAT treatment planning was performed retrospectively on a cohort of 16 liver SBRT patients stratified by small and large target volumes to compare optimized non-coplanar arcs to a clinical arc template. Significant dosimetric sparing of the liver was found for all but one RTOG1112 metric using an average of four arcs. This work shows that non-coplanar geometries can spare dose to healthy liver without an excessive number of IMRT fields or sub-arcs.

This work has been submitted to *Medical Physics* and is under review.

"Lincoln JD, MacDonald RL, Ward L, Johnston S, Syme A, Thomas CG. *Biologically Optimized Non-Coplanar Arc Selection for Small vs. Large Target Volumes in Liver SBRT.*"

6.2 Abstract

Purpose: Non-coplanar arc optimization has the potential to identify VMAT arcs that can perform similar dose reductions to published IMRT results, while leveraging delivery efficiency and trajectory sampling. The purpose of this research is to generate optimized static-couch arcs that consider OAR biology and arc delivery efficiency, along with the trajectory sampling metric mean arc distance (MAD).

Methods: Separate BEV cost maps were created for parallel, and serial OARs by means of a fast ray-triangle intersection algorithm. An additional BEV cost map was created for the liver which, by definition, encompasses the liver tumors. The individual costs of these maps were summed and 100,000 random combinations of arc trajectories were derived. A search algorithm was applied to find an arc trajectory solution that satisfied BEV cost and MAD minimization, while also ensuring an efficient delivery was possible with a low number of arcs. This method of arc selection was evaluated for 16 liver SBRT patients characterized by small and large target volumes. Comparisons were made with a clinical arc template of coplanar arcs. Dosimetric plan quality was evaluated using published guidelines and metrics from RTOG1112.

Results: Four of five plan quality metrics for the liver were significantly reduced when planned with optimized non-coplanar arcs. The effective liver volume was reduced on average by 34.8 ± 59.2 cc ($p = 0.049$). Volume receiving 10 Gy, 18 Gy, and 21 Gy were reduced by 7.8 ± 8.7 % ($p = 0.001$), 60.9 ± 85.5 cc ($p = 0.0023$) and 28.4 ± 52.9 cc ($p = 0.0386$), respectfully. A significant increase in mean dose to the right kidney of 0.2 ± 0.9 Gy ($p = 0.03$) was also found using optimized non-coplanar arcs, which was below tolerance of 10 Gy for all cases. The average number of arcs chosen was 4 ± 1.

Conclusions: Biologically optimized static couch non-coplanar arc selection significantly reduced dose to the liver during SBRT using a moderate number of arcs.

6.3 Introduction

Non-coplanar optimization methodologies are a subset of trajectory optimization techniques that aim to leverage additional degrees of freedom in radiotherapy (RT) treatment settings [11]. C-arm linear accelerators have great potential for trajectory optimization due to the many axes available for manipulation. Advances in the last decade of research have progressed from beam angle optimization (BAO) that automatically selects ports for intensity modulated radiotherapy (IMRT) [22,23,62,129], to efficiently choreographed non-isocentric dynamic couch translation and rotation techniques where almost all possible axes are optimized [7]. Throughout this time, retrospective comparisons between these increasingly complex techniques and the clinically accepted reliability of volumetric modulated arc therapy (VMAT) [4] have not been significant enough to realize widespread clinical adoption of these technologies.

In one prospective clinical trial, non-coplanar IMRT beams were used in a cohort of 11 high grade glioma patients and showed equal or lower maximum and mean doses to organs-at-risk (OARs) compared to VMAT arcs chosen by an experienced dosimetrist [72] . A separate prospective phase II trial performed automated planning using HyperArc$^{\text{TM}}$ (Varian Medical Systems, Palo Alto, CA) non-coplanar VMAT arcs for recurrent head and neck cancers with a cohort of 15 patients [82]. This research concluded statistically significant increases in dose conformity with increases to maximum doses to OARs that were well below desired planning constraints. This work examined moving from two coplanar VMAT arcs to four non-coplanar arcs at couch angles defined by Clark *et al.* [130] where it was found an increase in delivery time of approximately two minutes was not clinically significant [82].

Clinical adoption of trajectory optimization has primarily used Varian's HyperArc^{TM} (Varian Medical Systems, Palo Alto, CA), where a specific geometry defined by a clinical class solution of VMAT arcs [130] is given to begin the treatment planning process for cranial indications. Evaluating this cranial class solution (though not using HyperArc commercial product) compared to patient-specific non-coplanar VMAT arc optimizations has shown favourable OAR sparing for the latter [5,29,30,100].

According to a recent review of non-coplanar radiotherapy optimization, there have been few efforts to perform comparisons between coplanar VMAT arcs with non-coplanar VMAT arcs in sites outside of the cranium [11]. This is supported by earlier work finding non-coplanar VMAT arcs chosen by a human were more efficient to deliver than static non-coplanar IMRT ports for liver stereotactic body radiation therapy (SBRT)[83]. However, it is impractical to ensure a human operator consistently and optimally selects non-coplanar arcs due to the vast degrees of freedom that must be considered [83].

Previous non-coplanar optimizations have catalogued geometric suitability of delivering specific BEVs based on the amount of overlap with the PTV in a volumetric projection at isocenter [22,23,29,30,83,100]. To build in dosimetric tolerance of individual OARs, maximum dose weighting factors have been applied based on published maximum dose tolerance values [29,30]. This is suitable for the use case of OARs inside the cranium due to their serial biology and maximum dose constraints. For example, every beams-eye-view (BEV) that contains brainstem overlap can be equally weighted by its maximum dose constraint as the biological response should be the same if any functional subunit of the brainstem receives a dose larger than its maximum tolerance. However, in extracranial radiotherapy such as liver SBRT, considerations must be made for the serial nature of abdominal OARs such as the bowel, stomach, and duodenum, while also considering the parallel nature of the liver and kidneys.

In this research we propose a methodology for automatically optimizing the selection of non-coplanar arcs for liver SBRT that considers extracranial biology and preliminary considerations for delivery efficiency. The method considers OARs in three categories and uses geometric raytracing to calculate distinct costs using overlap with the PTV in the (BEV) for each category. This is then combined with the trajectory sampling metric, mean arc distance (MAD)[12], to generate non-coplanar arc trajectories. Considering these geometry metrics with the delivery efficiency metrics of number of arcs and arc length allows a stochastic algorithm to choose optimized arc trajectories bound by patient specific collision zones.

Although generalizable to any anatomical site in the body and extendable to dynamic axes optimization, the aim of this research study was to propose a methodology that would introduce minimal changes to current clinical workflows. In this way, future clinical trials with non-coplanar methodologies can be facilitated.

6.4 Methods

6.4.1 Raytracing through BEV projection

To calculate a cost associated with the overlap in the BEV between PTV and OARs, the ray-triangle intersection method [99] offers an efficient methodology to trace through many large OARs for each unique aperture. This methodology requires data in the form of meshes / triangulations. Clinical structures (body contour, PTV, OARs) were exported from the treatment planning system as 3D point clouds. The body contour was pre-processed to remove discontinuities and triangulated in MATLAB (R2022a, The Mathworks Inc., Natick MA).

Overlap was tested for every unique BEV by projecting the PTV and OAR contours to a plane at isocenter. If there was no overlap, the BEV was assigned a cost score of 0, however if there was overlap, the assigned cost calculation was dependent on the biology of the OAR being considered.

6.4.2 Encompassing OARs

Encompassing OARs were defined for the purposes of this work as the OARs which contain the PTV, in this case the liver. Previous literature using BEV cost calculations has not explicitly considered these OARs as there is overlap with every BEV [5,29,30,100]. To overcome this, we assign a depth cost specifically to the liver minus GTV OAR. Rays were traced from the source to a gridded 2D projection of the PTV at isocenter with a fixed resolution of 1 ray per 5 mm. Depth was calculated by measuring intersection distances along ray lines traced from the source through each point on the projection grid. The average PTV entrance depth was subtracted from the average OAR entrance depth, yielding a BEV specific cost of delivering radiation through depths in the liver. This is summarized by:

$$L(C,G) = \left(\frac{1}{N} \sum_{i=1}^{N} (l-p)_i \right) \tag{6.1}$$

where *L (C, G)* is the cost of delivering radiation to the liver at the BEV unique to couch angle *C* and gantry angle *G*. This equation contains *l,* the entrance depth to the liver along a ray *i,* and *p*, the entrance depth to the PTV at the depth along the same ray. Here, *N* denotes averaging the differences between entrance depths and corresponds to the total number of rays. This yields a 2D cost map with each pixel corresponding to a depth informed cost of delivering to the PTV through the liver.

A calculation was then performed to broaden the solution space, while ensuring geometric regions of large depths (thus high cost) were considered for avoidance. The mean value of this 2D cost map was chosen as a threshold, and all values below the threshold were set to zero. This ensured cost was attributed to paths with long lengths through the liver that exceeded the mean depth calculated for all apertures, while paths that did not exceed the mean depth were attributed zero cost to allow a greater solution space to be sampled. Finally, the map was normalized to its maximum value to facilitate combining with cost from all other OARs.

6.4.3 Parallel OARs

The parallel OARs used in these optimizations were the heart, left kidney, and right kidney. These parallel structures did not contain the PTV and do not have maximum dose constraints according to RTOG1112 [17]. To calculate the BEV cost when these OARs overlap with the PTV, the same raytracing methodology was applied to a different calculation than the encompassing liver OAR. The calculation followed the methodology of Lincoln *et al.*[116]

This is summarized for a single ray by:

$$P(C,G) = \frac{AUC_p}{AUC_T} \tag{6.2}$$

$$AUC_p = \int_{d_1}^{d_2} PDD(x)dx$$

$$AUC_T = \int_{d_1}^{\infty} PDD(x)dx$$

Where the BEV cost for a parallel OAR *P,* at the BEV unique to couch angle *C* and gantry angle *G* depends on the ratio of the partial area (AUC_p) defined by OAR entrance distance d_1 and exit distance d_2 to the total area under the PDD curve (AUC_T) The cost is summed over all rays and then normalized for each parallel OAR.

6.4.4 Serial OARs

The serial OARs used in these optimizations were the stomach, duodenum, and spinal cord. They each have maximum dose constraints according to RTOG1112 [17]. Before exporting from the TPS, each OAR was expanded with a 5 mm margin to create a planning risk volume (PRV) which was used in the BEV optimization. As serial OARs differ biologically from parallel and parallel encompassing OARs, a separate BEV cost was calculated using the same raytracing algorithm.

The degree to which serial OAR BEV overlap with the PTV necessitates dose sparing effort depends on the spatial proximity between the two structures. Ensuring rapid dose fall off outside the PTV is a characteristic of SBRT treatment planning, therefore cost was only calculated for serial OARs if they fell within a fall-off region specified by considering the OARs specific dose constraint (D_{OAR}) relative to the prescription dose (D_{Rx}). This is summarized by:

$$A_{fall}[mm] = \frac{100[\%] * \left(1 - \frac{D_{OAR}[Gy]}{D_{R_x}[Gy]}\right)}{G\left[\frac{\%}{mm}\right]} \tag{6.3}$$

where A_{fall} is the necessary fall off distance for inclusion in the cost function at an achievable gradient G. In this work G was set equal to 5% per mm, a more conservative estimate of an achievable gradient than previous work[100]. Thus, only points on a serial OAR less than or equal to A_{fall} are included in the BEV cost calculation. The closest distances between the PTV and each serial OAR were measured before raytracing. All points less than or equal to A_{fall} were triangulated to create an avoidance structure corresponding to the serial OAR. Any point in an OAR greater than A_{fall} was not considered in the calculation of cost. The cost of avoiding this structure followed Equation 6.2 and was repeated for each serial OAR.

6.4.5 Constructing the Total BEV Cost Map

Combining all OARs to create the total BEV cost map is as follows:

$$E(C,G) = L(C,G) + P(C,G) + S(C,G) \tag{6.4}$$

where the total cost is the sum of the normalized encompassing liver depth cost L (Equation 6.1), the parallel OARs overlap cost P (Equation 6.2), and the serial OAR avoidance cost S (application of Equation 6.2 to serial OARs). This total BEV cost map underwent a final normalization, and then patient specific collision zones were added in a modification to previously published techniques[77].

An example case undergoing all steps of BEV cost map construction is shown in Figure 6.1.

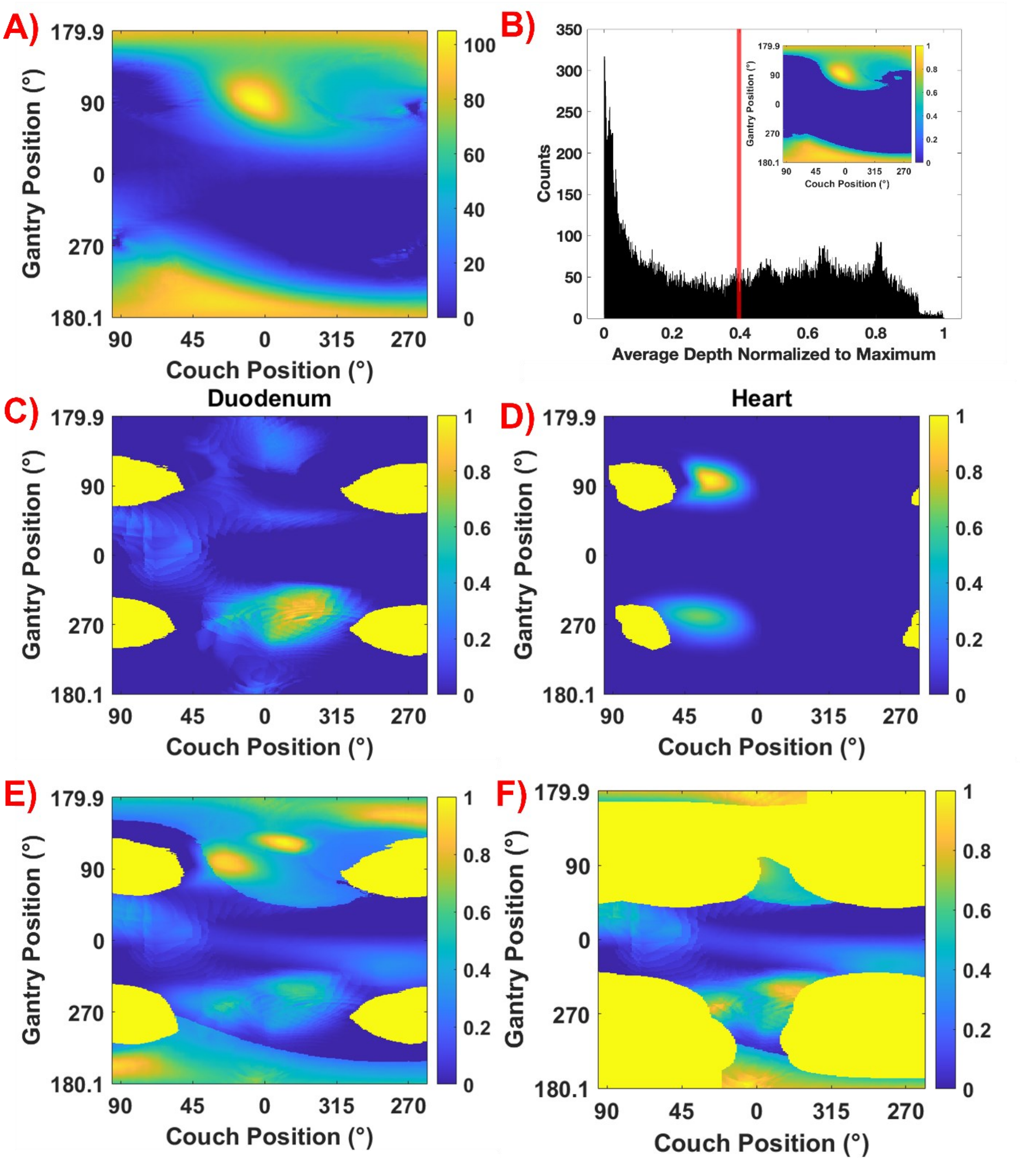

Figure 6.1: (A) The raw depth cost values extracted for the liver minus GTV OAR with colourbar scale measured in millimeters [mm]. (B) Histogram of depth in (A) normalized to the maximum, with red line denoting the mean depth value. The top right-hand corner of (B) shows how thresholding (A) based on the mean depth values changes the map in (A). (C) shows an example serial OAR BEV cost map for the duodenum PRV of the same case. (D) shows an example parallel OAR BEV cost map for the heart of the same case. (E) shows the resulting combination of all OARs without collision zones. The brightest yellow regions of (C-E) indicate raytracing through holes in the CT set. (F) the final BEV cost map showing the combination of all OARs with patient specific collision zones.

The dark blue regions on the map of Figure 6.1A represent areas of shallow PTV depth inside the liver while lighter yellow demonstrates deeper PTV depths as calculated by Equation 6.1. In Figures 6.1C – 6.1F, dark blue regions correspond to lower normalized BEV cost scores as calculated with Equations 6.2 – 6.4, while the lighter yellow regions are higher normalized BEV cost scores.

6.4.6 Patient specific arc trajectories

The BEV cost maps that quantify priority avoidance of OARs were used to create patient specific arc trajectories by first creating a candidate pool of deliverable arcs, and then performing a stochastic search to find optimized arcs[116]. It was deemed important that the candidate pool contain a mix of long and short arcs. This gives the arc selection algorithm flexibility in balancing lower spatial sampling if short arcs with low cost are used with longer arcs that will increase spatial sampling at the expense of potentially higher BEV cost[116].

Approximately 5000 candidate arcs were created for each BEV cost map by the method of Lincoln *et al.*[116] and the stochastic search was subjected to 100,000 permutations, yielding a spectrum for each trajectory metric for simultaneous optimization.

An optimized trajectory of high quality should have sufficient geometric sampling (low MAD), minimal overlap with OARs in the BEV (low BEV cost) and consider delivery efficiency (low number of arcs and reasonable number of control points). To allow the algorithm to search for high quality solutions that contain a small number of control points while also searching a clinically feasible higher control point range, lower and upper bounds on control point number were created to filter the solutions. In the same method as Lincoln *et al.*[116] the lower and upper bounds were empirically calculated by combining the standard deviation of the number of control points for the 100,000 random arc trajectories with the number of control points used for a clinical liver SBRT arc template (200).

The empirical calculation is summarized in Equations 6.5 and 6.6.

$$N_{Lower} = N_{clinical} - \frac{\sigma}{2} \tag{6.5}$$

$$N_{Upper} = N_{clinical} + 2\sigma \tag{6.6}$$

where N_{Lower} is the lower limit of the range, N_{Upper} is the upper limit of the range, $N_{clinical}$ is the number of control points for the clinical arc template equal to 200 (2° sampling), and σ is the standard deviation of the number of control points found across all 100,000 permutations of the simulation.

To choose optimized arcs from the candidate set, the percentile searching method of Lincoln *et al.*[116] was modified to incorporate number of arcs. Instead of iteratively searching through the lowest percentiles of MAD and BEV cost the following sorting methodology was applied:

1. For each potential number of arcs (2 to 10), find solutions that have a MAD score within the bottom 5% (empirically chosen) of that subset.
2. Sort the entire subset found in (1) by the quadrature sum of BEV cost and MAD.
3. The optimized arc trajectory minimizes the value found in (2).

Therefore, each contribution to a high-quality trajectory arc set was considered in the optimization. This method will inherently prioritize solutions with a lower number of arcs that are correlated with a lower BEV cost, and thus a lower quadrature sum. Figure 6.2 shows an example of the arc trajectory chosen based on the spectrum of solutions for the example case shown in Figure 6.1.

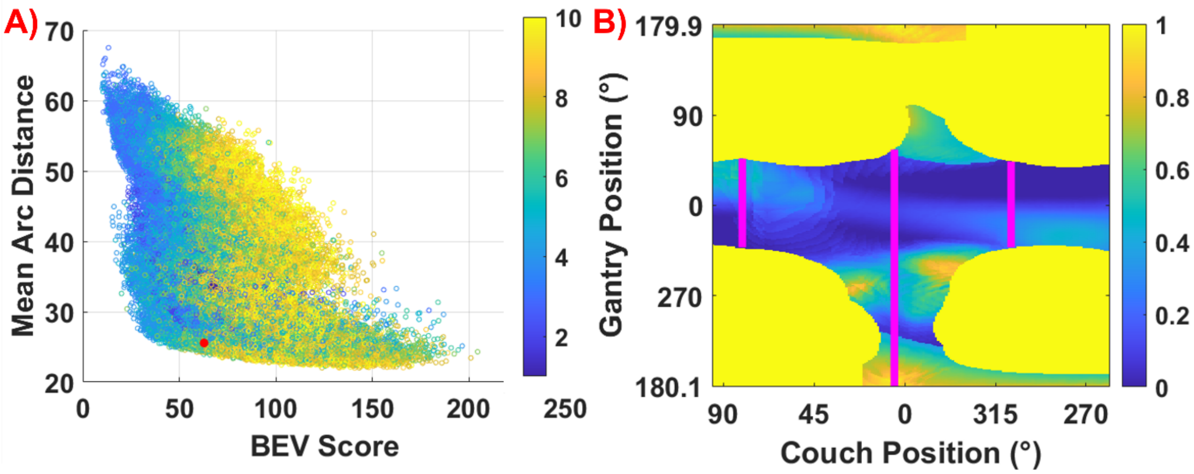

Figure 6.2: (A) BEV score plotted against Mean Arc Distance for 100,000 random arc trajectories. Dots denoted by the colourbar indicate the number of arcs in the solution ranging from 2 to 10. The red dot shows the scores for the optimized arc trajectory that was chosen. (B) The example BEV cost map with collision zones from Figure 6.1F with the optimized arc trajectory from 6.2A shown in magenta lines.

6.4.7 Treatment planning

Treatment planning was performed retrospectively on 16 patients selected randomly who previously received liver SBRT at our institution. Patient cases were anonymized, and their use was approved by the Research Ethics Board of Nova Scotia Health. Of these 16 patients, 8 were designated small targets (PTV < 50 cc) while 8 were designated large targets (100 cc < PTV < 500 cc). See Table 6.1 for volume and prescription information for each case.

Table 6.1: Target volume descriptions for the 16 patients used in this study including prescription dose and fractionation.

Patient ID	Target Volume (cc)	Prescription (Gy) / fractions
1	47.8	54 / 5
2	35.7	35 / 5
3	38.7	45 / 5
4	20.6	45 / 5
5	5.7	50 / 5
6	43.3	50 / 5
7	47.9	45 / 5
8	13.9	50 / 5
9	432.8	30 / 5
10	115.1	54 / 5
11	171.5	40 / 5
12	278.8	45 / 5
13	145.1	50 / 5
14	167.1	30 / 5
15	263.5	27.5 / 5
16	217.59	40 / 5

As the OARs included in VMAT optimization for liver SBRT treatment planning are at the discretion of the prescribing radiation oncologist based on proximity to the PTV, the number can vary between patients. Introducing non-coplanar arcs has the potential to include OARs that were not originally considered. Therefore, a standardized set of OARs were contoured by two expert dosimetrists with extensive experience contouring OARs for liver SBRT. These OARs were contoured for each patient corresponding to the OARs used in the BEV cost map construction described in sections 6.4.2 – 6.4.4. Prescription doses varied across the patient population due to the variation in target size.

Each patient was replanned with two VMAT plans differing only by arc geometry used. The first used a clinical arc template of two coplanar arcs at couch position 0° spanning 200° from gantry position 20° to 180° in both clockwise and counterclockwise directions, with complementary collimator angles (15° and 345° respectively). The second plan used the optimized arcs described in Section 6.4.6.

VMAT optimization was performed for all plans by two medical physicists with considerable experience planning clinical liver SBRT. The Eclipse treatment planning system (Varian Medical Systems, Palo Alto CA) version 15.6 was used with photon optimizer (PO) version 15.6 and the Acuros External Beam (AXB) algorithm version 15.6 for dose calculation[66]. As per institutional standards, the prescription dose for each plan was prescribed to the 90% isodose. Standardized VMAT optimization parameters were normal tissue optimization (NTO = 175) and an AXB dose calculation grid resolution of 1.5 mm. Specific priorities on the PTV, OARs and/or tuning structures were modified by the same amount on clinical and optimized arcs, as needed to aid with target coverage, OAR sparing and low dose spread. These priorities were adjusted depending on local anatomy. Each plan was normalized such that the prescription isodose covered 99% of the PTV.

6.4.8 Plan comparison

The plan metrics found in RTOG1112 [17] were used as the basis for comparison between arc geometries. These guidelines are used in clinical institutional practice for treating lung SBRT. Maximum dose (to 0.03 cc) metrics and specific dose-volume objectives were evaluated for the OARs considered in the treatment planning process. Target metrics of the Paddick conformity and gradient index (CI, GI) [114,115] were evaluated according to Equations 6.7 and 6.8 respectively. Target coverage was also evaluated in terms of the maximum dose to 0.03 cc and mean dose to the target.

$$CI = \frac{V_{T,ref}}{V_T} \times \frac{V_{T,ref}}{V_{ref}} \tag{6.7}$$

where $V_{T,ref}$ is the volume of the target (T) that receives a dose greater than or equal to a reference dose. V_T is the volume of the target, and V_{ref} is the reference isodose volume. In this work, V_{ref} is equal to the prescription isodose volume given in Table 6.1.

$$GI = \frac{V_{50\%R_x}}{V_{R_x}} \tag{6.8}$$

where the GI is defined as the ratio of the volume receiving half of the prescription isodose, to the volume receiving the prescription isodose.

An in house developed ESAPI script extracted the relevant DVH metrics inside the TPS to a tabular format. The table was then exported into MATLAB to perform final analysis and statistical testing. The Wilcoxon Signed – Rank test (two – tailed) is a non-parametric statistical test that has been used throughout the literature comparing non-coplanar arc selection [5,29,30,100]. Comparisons between plan quality metrics of the two arc selection methods were made with a significance level set at $p < 0.05$ [127].

6.5 Results

On average, the stochastic optimization chose 4 ± 1 arcs for the optimized solution.

Figure 3 shows a boxplot of the liver metrics used for both methods of arc selection. The OAR used for measurements of these metrics was “Liver – GTV” (liver minus GTV).

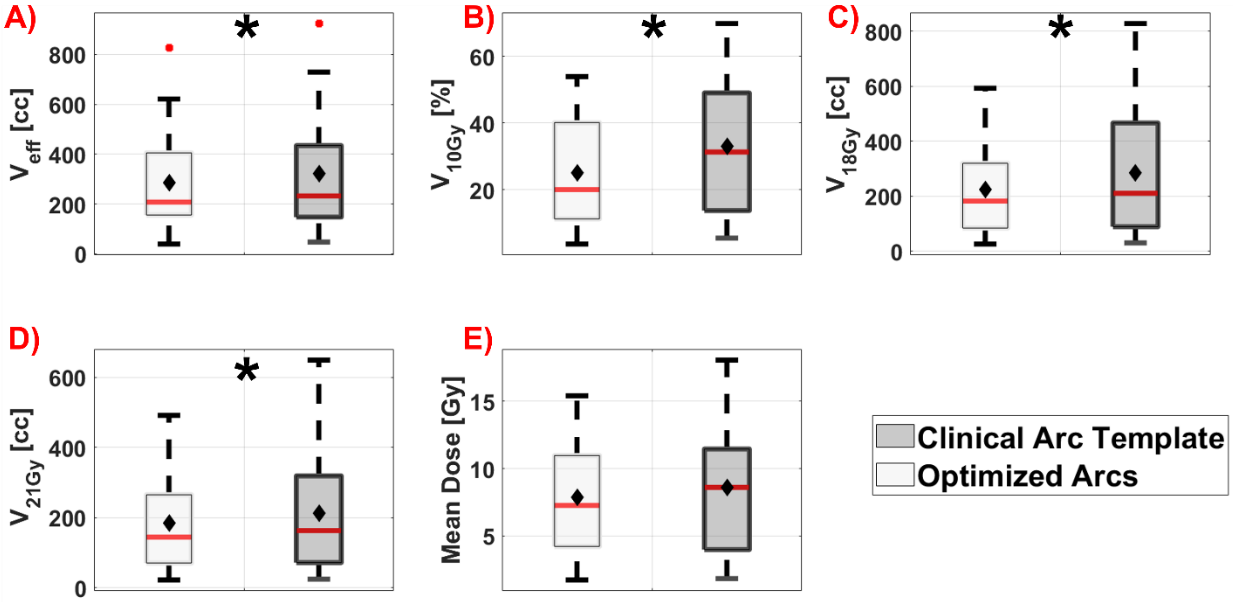

Figure 6.3: (A) Liver metric results shown for effective liver volume (V_{eff}). Percentage of the liver volume receiving 10 Gy is shown in (B). The dose volume results are shown for 18 Gy (C), 21 Gy (D) and mean dose (E). Light grey boxes denote the optimized arc solution while dark grey boxes represent the clinical arc template. The median is given as the red line inside each box, while the mean is denoted as filled black diamonds. Outliers are illustrated with filled red circles. Statistically significant differences are denoted with black stars.

As seen in Figure 6.3A – Figure 6.3E, all liver metrics considered in this study were reduced using optimized arcs, with one reduction not meeting the criteria for statistical significance: the mean dose to liver reduction of 0.8 Gy ($p = 0.0556$). Figure 6.3A demonstrates that using optimized arcs results in a statistically significant reduction in effective liver volume of 34.3 cc on average ($p = 0.04942$). Figure 6.3B shows a statistically significant average reduction in V10Gy expressed as a percentage of the Liver – GTV of 7.8% (p = 0.001). From Figure 6.3C and Figure 6.3D, on average the optimized arcs decreased the volume receiving 18 Gy and 21 Gy by 60.9 (p = 0.0023) and 28.4 cc (p = 0.0386) respectively compared to the clinical arc template.

Figure 6.4 expands on the differences in the liver metrics by displaying the quantitative differences between arc selection methods as a function of target volume. All points below the red line indicate where the clinical arcs offered superior liver sparing, while the points above the red line indicate where optimized arcs offered superior liver sparing.

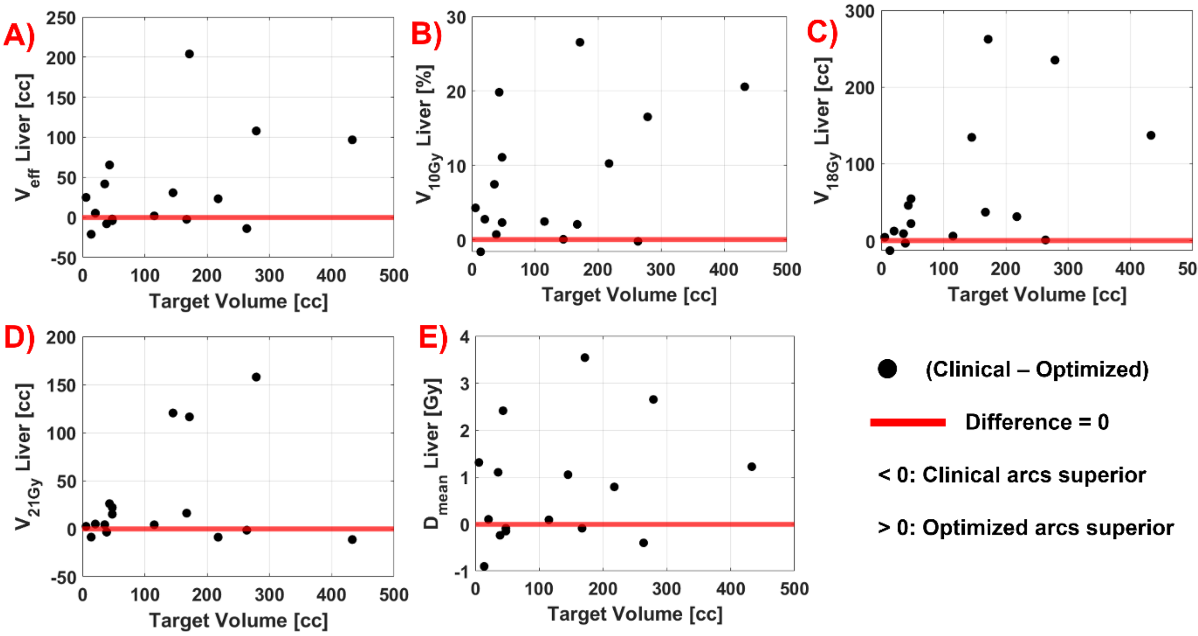

Figure 6.4: Difference between clinical and optimized arcs for each metric corresponding to Figure 6.3A - Figure 6.3E was plotted as a function of target volume. Black dots indicate the difference in subtracting the metric using clinical arcs from the same metric using the optimized arc solution. Red lines indicate the baseline difference equal to zero where there would be no quantifiable difference in metric based on the method for geometric arc selection.

Greater numbers of points above the red line for all metrics demonstrated by Figures 6.4A – 6.4E give insight to the significant reductions in liver metrics shown in Figures 6.3A –

6.3E. The largest comparative reduction in liver volume using optimized arcs is shown in Figure 6.4C where V18Gy was reduced by 262.2 cc in one case for a target volume of 171.5 cc. Conversely, the largest comparative increase in liver volume using optimized arcs is shown in Figure 6.4A where V_{eff} was increased by 21.2 cc for a target volume of 13.9 cc. Pearson correlation coefficients were computed for each metric yielding weak correlations, each below a signficance threshold of 0.7. The strongest correlation was found for V18Gy at R = 0.54.

Figure 6.5 shows the 3D dose distribution for an example case (test patient 12, R_x = 45 Gy / 5 fx). Figure 6.5A shows the 25% isodose splaying throughout the majority of the liver minus GTV volume. Figure 6.5B shows the same 25% isodose concentrated into a smaller volume inside the the liver.

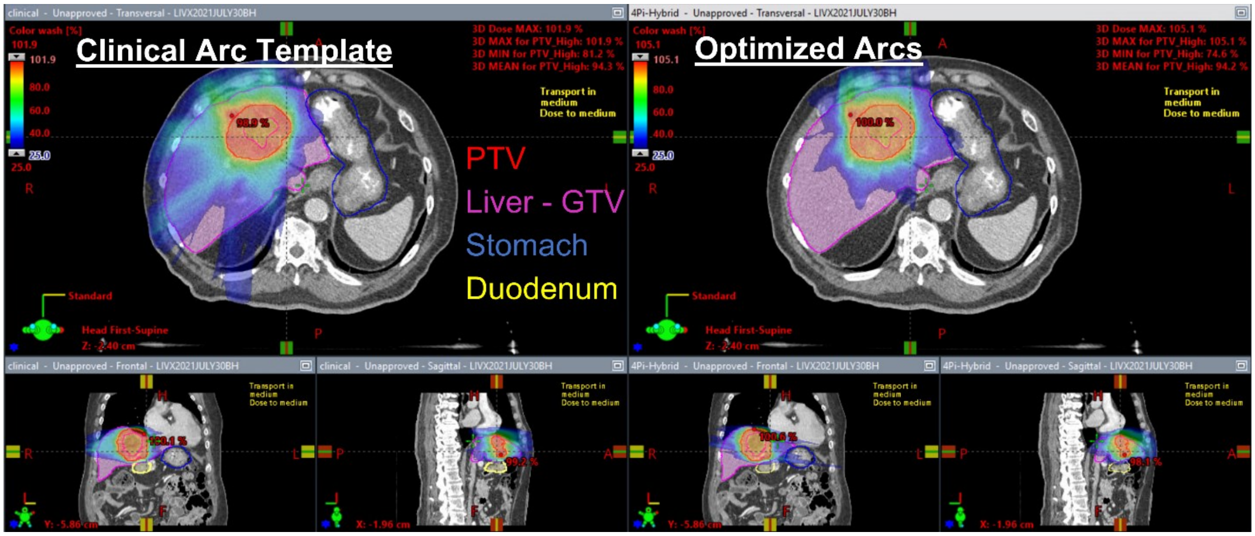

Figure 6.5: Dose distribution for an example case. The plan using the clinical arc template is shown on the left-hand side and the plan using the optimized arcs is shown on the right-hand side for the same slices. Contoured structures correspond to their contour colours in the TPS are shown. The PTV was contoured in red, liver minus GTV was contoured in magenta, PRV stomach was contoured in blue, and PRV duodenum was contoured in yellow. The lower limit of each dose wash was set to 25%.

Figure 6.6 displays the example dose volume histogram (DVH) for the case of Figure 6.5, with the same OARs.

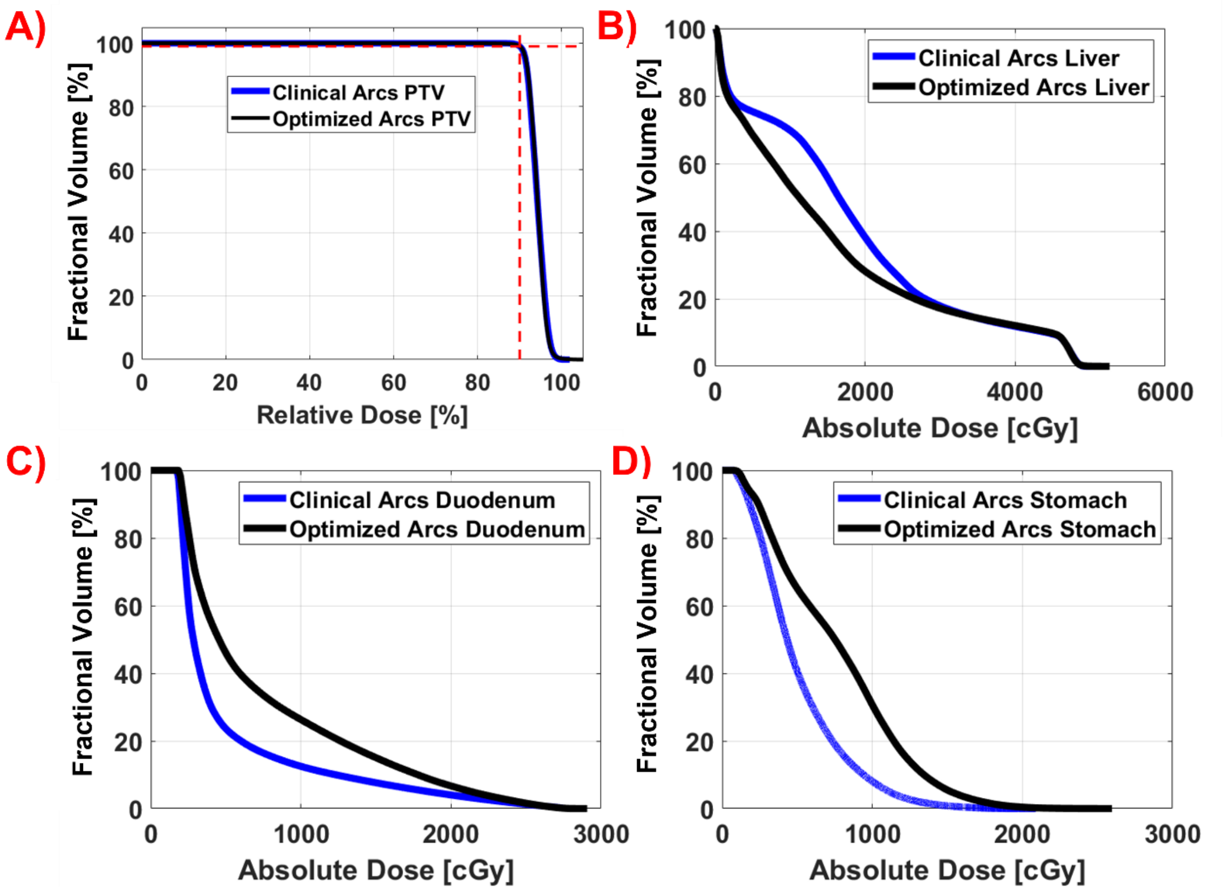

Figure 6.6: Example DVH for PTV (A), liver minus GTV (B), PRV duodenum (C), and PRV stomach (D). Blue lines denote the DVH for the clinical arc template, while black lines denote the DVH for the optimized arcs solution. The red dashed line of Figure 6.6A shows the normalization point of the prescription dose at 99% volume covered by the 90% isodose (100% of the Rx).

As can be seen in Figure 6.6A comparable PTV coverage was found for this example case where blue and black DVH curves are approxiamtely equal. The DVH of Figure 6.6B shows similarities between methods of arc selection except at doses approximately below 2500 cGy where the optimized arcs demonstrate lower volume irradiated. This correspoonds to the results seen in Figures 6.3B, 6.3C, and 6.3D. Conversely, larger irradiated volumes using the optimized arcs were found for both PRV stomach and PRV duodenum, however each remained below their respective dose constraints.

Target metrics are shown in Figure 6.7. Three metrics from Figure 6.7 were statistically signficant. Figure 6.7A shows the conformity index that increased by an average 0.009 using optimized arcs (p = 0.0059). Figure 6.7C shows the maximum dose inside the PTV which also increased on average by 0.7% (p = 0.0386) when using optimized arcs. These differences were statistically significant, however, both techniques on average were well below the acceptable values of 1.2 for CI and 108% for PTV D_{max}, respectively. As shown in Figure 6.7D, using optimized arcs results in an increase in the mean PTV dose on average of 0.4%, which was not deemed statistically significant. Figure 6.7B shows that the gradient index was statistically significantly reduced using optimized arcs by an average of 0.2 (p = 0.0278).

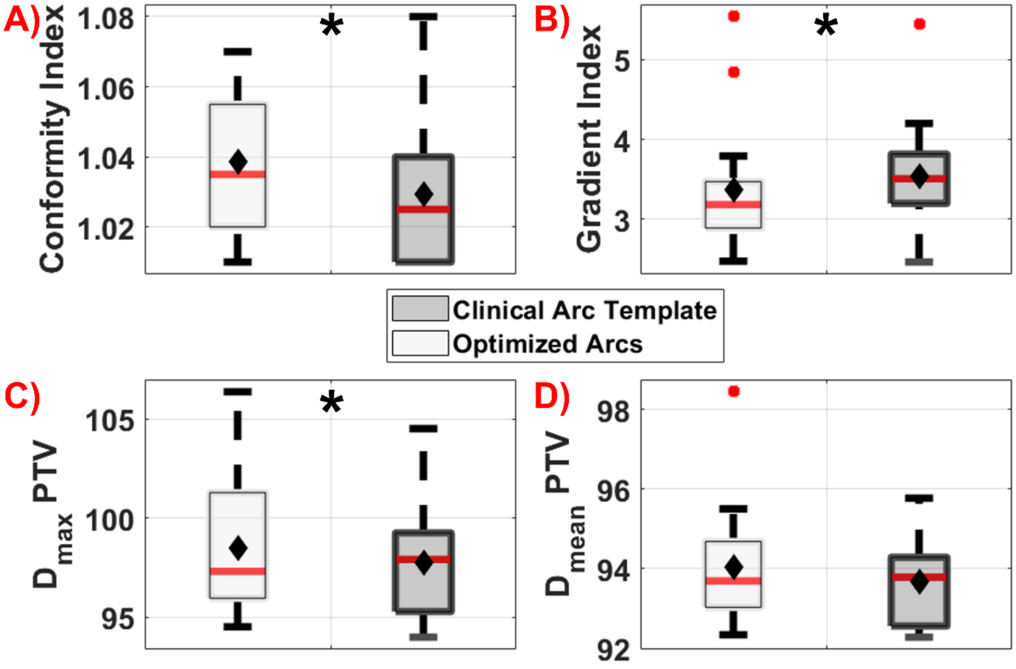

Figure 6.7: Conformity index of the target volume (A), gradient index (B), maximum dose inside the target (0.03 cc) (C), and mean dose inside the target (D). Light grey boxes denote the optimized arc solution, while dark grey boxes represent the clinical arc template. The median is given as the red line inside each box, while the average is denoted as filled black diamonds. Outliers are illustrated with filled red circles. Statistically significant differences are denoted with black stars.

Figure 8 shows dose increases on average for the heart and PRV stomach of 0.82 and 0.99 Gy, respectively, from using optimizd arcs. Dose reductions were found on average for the PRV duodenum and PRV spinal cord max dose of 0.55 Gy and 0.28 Gy, respectively. None of these reductions were statistically significant.

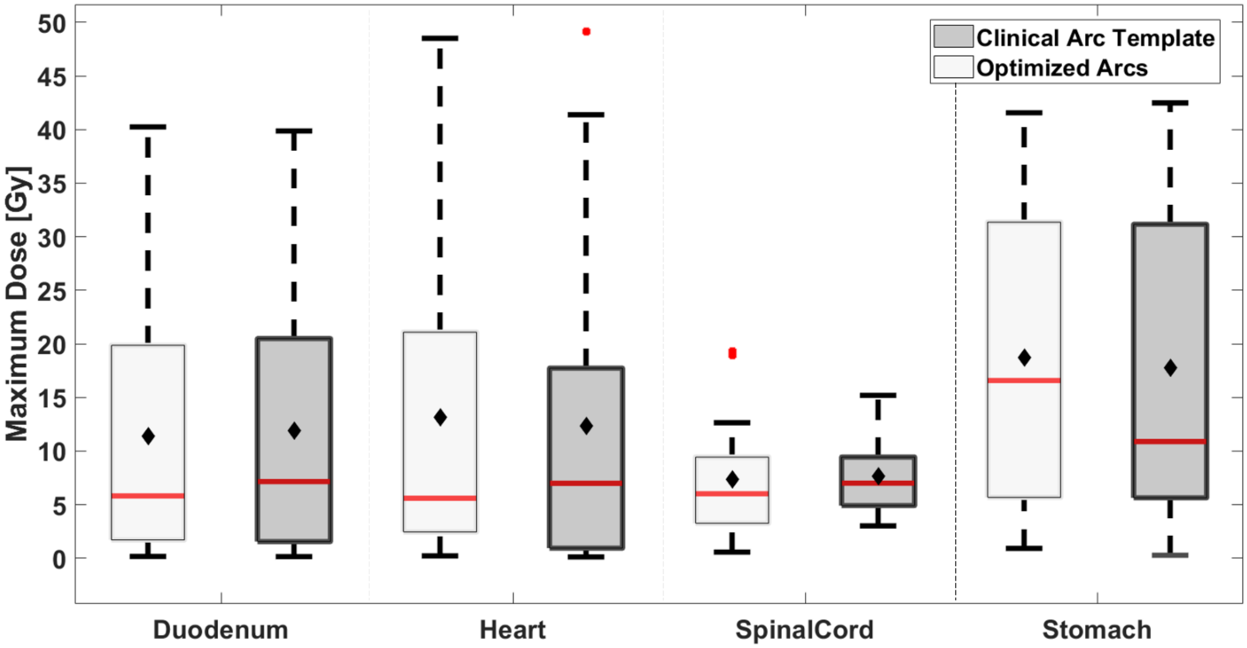

Figure 6.8: Maximum dose to 0.03 cc for OARs considered in the optimization with maximum dose constraints. Light grey boxes represent the optimized arc solution, while dark grey boxes represent the clinical arc template. The median is given as the red line inside each box, while the average is denoted as filled black diamonds. Outliers are illustrated with filled red circles. Statistically significant differences are illustrated with black stars.

From Figure 9, one statistically significant dose increase was found for the right kidney of 0.15 Gy (p = 0.0312) on average using optimized arcs. The left kidney mean dose was reduced on average using optimized arcs by 0.24 Gy, however this reduction was not statistically significant.

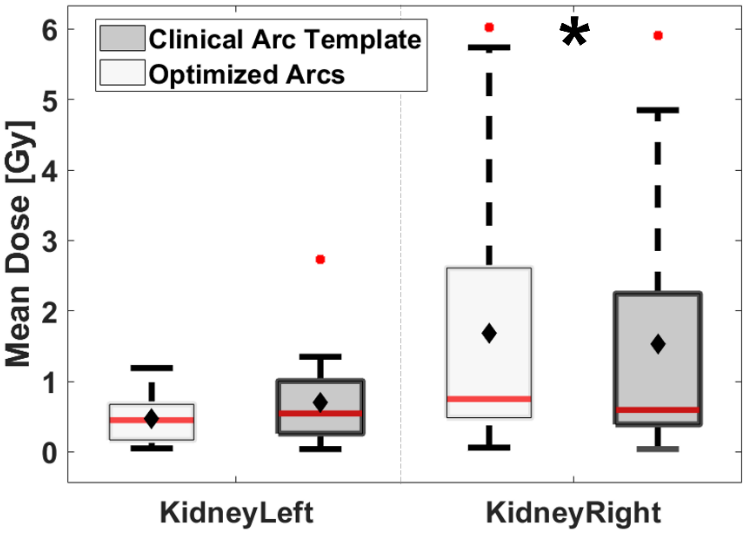

Figure 6.9: Left and right kidneys were considered in the optimization with mean dose constraints. Light grey boxes represent the optimized arc solution, while dark grey boxes represent the clinical arc template. The median is given as the red line inside each box, while the average is denoted as filled black diamonds. Outliers are illustrated with filled red circles. Statistically significant differences are denoted with black stars.

6.6 Discussion

In this work, a methodology was presented that incorporates OAR specific biology into the construction of a BEV cost map. These biological considerations are more pertinent in extracranial sites, such as the liver, as compared to the cranium, and are especially important in hypofractionated dosing regimes. Combining the unique avoidance priorities of serial, parallel, and parallel encompassing OARs into a single cost map then allowed for a stochastic pathfinding algorithm to search for an optimized solution. Considerations were made in attempt to choose arc trajectories that optimized delivery efficiency, BEV cost, and trajectory sampling simultaneously. The method was compared to a clinical arc template used in our institution for treating liver SBRT.

On average, in the cohort of 16 patients that were planned with a clinical arc geometry and optimized non-coplanar arc geometry, the analysis shows an overall tradeoff between liver sparing and OAR sparing. This is reflected in the dose reduction results for the liver as shown in Figure 6.3 – Figure 6.5, and Figure 6.6B, in contrast to the maximum dose results of Figure 6.8 and the example DVHs of Figure 6.6C and Figure 6.6D.

Our results can be compared to othernon-coplanar optimizations in the literature for liver SBRT [23,83]. In both works, compared to coplanar VMAT, non-coplanar IMRT was performed with 14 to 22 beams on a cohort of 10 patients[23] and 20 field IMRT on a cohort of 20 patients[83], respectively. Woods *et al.* also chose to compare three to four non-coplanar VMAT arcs that were selected without optimization. In our work, the stochastic optimization chose four arcs on average. They separately found superior OAR maximum point dose reductions using IMRT compared to coplanar and non-coplanar VMAT. We found agreement with their research as their

IMRT OAR doses are comparable to but less than what we found using both optimized non-coplanar and non-optimized coplanar VMAT arc selection. Liver sparing was quantified in terms of the volume receiving greater than 15 Gy, compared to our research that used V10Gy, V18Gy, and V21 Gy in accordance with RTOG1112 [17]. Both authors quote reductions in V15Gy on the order of 50 cc to 80 cc with IMRT, while our work found reductions in V10Gy V18Gy and V21 Gy of 7.8%, 60.9 cc and 28.4 cc, respectively.

Although non-coplanar IMRT has the capabilty to reduce doses in liver SBRT and faciliate dose escalation, the number of treatment fields is clinically cumbmersome to deliver [23,83]. Additionally, when considering patient motion throughout the course of treatment, efficient techniques are needed. The optimized arc solutions created in this research apply considerations for delivery efficiency. This tradeoff is readily apparent in the increased maximum doses to OARs compared to the non-coplanar IMRT proposed by Dong *et al.* and Woods *et al.* However, similar dose reductions to liver were found in our work with efficient patient specific optimized arc geometries.

To compare the duodenum, which was not included by Dong *et al.* or Woods *et al.,* largest maximum doses and average maximum doses found in our work are lower than those found for similar GI structures in pancreas SBRT [73].

A limitation of this study includes the simple approximation made when considering thresholding the BEV cost maps specific to the encompassing liver OAR. Opening the solution space to depths less than the mean depth value could be suboptimal in a centrally positioned target where all depths are approximately equal. Furthermore, more sophisticated methods could be applied to combine the invidual BEV cost maps to better reflect biology. Specifically, the addition of weighting factors to each of encompassing, parallel, and serial OAR BEV cost maps could bias the solution towards specific OAR avoidance if desired. The method of Wang *et al.* uses a cost associated with partial volumes [73] which could also be applied to improve the BEV cost equation used in our research. Finally, the stochastic arc selection algorithm has potential to be improved without using an empirically chosen lower bound of MAD informed arc selection. Further research is required to undestand the relationship between MAD and conformity. Given this information, the solution set has the potential to be expanded at the lower bound corresponding to acceptable clinical conformity which is not known at this point until after treatment planning.

6.7 Conclusion

In conclusion, this research demonstrated a methodology of non-coplanar arc optimization for VMAT as applied to liver SBRT. Biological considerations for the degree of seriality of specific OARs were incorporated into a BEV cost function, and a stochastic search algorithm chose optimized arc trajectories that considered delivery efficiency, BEV cost, and trajectory sampling using MAD. On average, maximum doses to OARs remained below tolerances specified by RTOG1112 for liver SBRT. The average number of arcs (4 ± 1) could be delivered more efficiently than 14 – 22 field IMRT proposed in the literature given the limitations of current clinical applications. These results showed significant reductions of irradiated healthy liver volumes for a collection of small and large targets compared to VMAT using a coplanar arc template.

7 Chapter 7: Conclusions

7.1 Summary

The purpose of this thesis was to optimize and automate the procedure of non-coplanar arc selection for SABR treatment planning with VMAT, while simultaneously lowering OAR doses and improving plan quality. Using automation to complement decision-making processes during SABR treatment planning alleviates the potentially laborious process of characterizing the optimality of a VMAT arc trajectory. Robustly examining the parameters that would be involved in this type of decision making allows planners to gain more insight into the potential trade-offs in plan quality, without having to explicitly create many treatment plans. SABR treatment planning has additional layers of complexity due to the ablative dosing regimes, a consideration that does not have comparatively lethal consequences in standard fractionation radiotherapy. These complexities are different for all anatomical sites, however this thesis also aimed to extend optimization proposed for intra-cranial SABR (SRS/SRT) to extracranial SABR (SBRT). Thoroughly optimizing these procedures provides a general overview how patient specific VMAT arc selection can be translated into clinical practice.

The arc selection procedure for intracranial SABR was addressed in the first manuscript (Chapter 4) where the complexity of optimizing the amount of BEV overlap in the PTV was associated with choosing patient specific arc trajectories that outperformed, in terms of maximum doses to OARs, a less complex anatomically informed template and least complex commercial geometric arc template.

The methods of Chapter 4 were broadened in the second manuscript (Chapter 5) to include the consideration of extracranial sites for large OAR volumes in lung SABR and complement

BEV overlap with the trajectory sampling metric MAD[12] to ensure adequate arc spacing and conformity. These optimized arc trajectories reduced maximum dose to OARs compared to a clinical arc template, while also maintaining acceptable target conformity.

Considering the biology of parallel encompassing, parallel, and serial OARs allowed the methods of Chapter 5 to be extended to liver SABR in the third manuscript (Chapter 6) where different BEV cost calculations accounted for unique avoidance priorities for each OAR type. Optimizations that considered balancing BEV cost with MAD, number of control points and number of arcs in this way resulted in significant sparing to liver metrics.

The first manuscript addresses the clinical utility of using templates for intra-cranial SABR treatment planning compared to optimizing a patient specific arc trajectory. Although current clinical practice uses an arc template[79,130], no anatomical information is considered. Thus, template arcs based on BEV overlap in six cranial anatomical class solutions were created. Eighteen artificial targets were contoured in anatomical regions of interest corresponding to the class solutions, and the three methods for arc selection were compared using a method that simulated automatic treatment planning. All OARs (brainstem, optic chiasm, eyes, lenses, optic nerves) showed maximum dose reductions using the patient specific arcs compared to the class solutions and geometric arc template, while the patient specific arcs were the only solutions on average that demonstrated statistically significant maximum dose reductions. It was concluded that increasing the complexity of the arc selection process in terms of patient specificity, yielded superior maximum dose sparing compared to both anatomical and geometric class solutions.

The second manuscript examines the considerations for optimizing arcs for extracranial SABR. The specific use case was lung SABR where OAR volumes are much larger than those found in cranial SABR. These size differences cause the cost equation used in the first manuscript to break down, and thus a new method was required. Raytracing was used calculate a dose surrogate through interpolation on a PDD, which then informed the suitability of BEVs for arc selection optimization. This method was combined with the trajectory sampling metric MAD whose utility had been previously only assessed in cranial SABR[12]. Contributions of these metrics were balanced to select arcs that optimized both BEV cost and MAD while also respecting the patient specific collision zones of the 18 test cases[77]. Through an iterative process, the final balancing of weights for each metric resulted in statistically significant maximum dose reductions to esophagus, trachea, spinal cord, aorta, and large bronchus, while ensuring comparable conformity to a clinical arc template. On average eight arcs were chosen for the optimized patient specific trajectories with no consideration for delivery efficiency.

The third and final manuscript extends considerations made in extracranial SABR to biological decision making that occur for liver SABR where the avoidance of many proximal serial and parallel structures must be balanced with also reducing dose to the parallel encompassing liver volume. Three separate BEV cost calculations were performed depending on an OAR's specific seriality (parallel encompassing, parallel, serial). The parallel encompassing liver BEV cost was related to the depths of the PTV inside the liver, with the aim to prioritize shallow beam paths through the normal liver and avoid long beam paths that would irradiate a larger liver volume. Parallel OARs that did not encompass the PTV were computed with the same BEV cost calculation from the second manuscript. Serial OARs were subject to a fall-off constraint calculation before BEV cost was calculated to account for proximity to the PTV in the overlap cost equation. Arc selection followed a modification of the second manuscript to include delivery efficiency by means of including an optimization for the number of arcs used. The average number of arcs selected compared to the second manuscript was halved (four), and this trade-off was reflected in statistically and clinically insignificant maximum dose reductions to stomach, duodenum, and spinal cord compared to a clinical arc template. The third manuscript work had an aim to use fewer arcs built into the cost function, while the second manuscript did not. However, these optimized arcs were statistically significant at sparing liver volumes up to 262 cc at the 21 Gy isodose level and reducing effective liver volume (V_{eff}), V10Gy, V18Gy and V21Gy.

7.2 Future Works

Non-coplanar arc optimizations have been discussed throughout this dissertation to improve dosimetric plan quality of various SABR sites. The hallmarks of non-coplanar optimization discussed in Chapter 3.1 suggest a myriad of potential avenues for future work. In this section the discussion will be limited to addressing specific limitations of each manuscript that can inform future work.

In the manuscript of Chapter 4, the constrained Bellman-Ford algorithm[5] does not make considerations for trajectory sampling or delivery efficiency. Its complexity is underscored by its ability to minimize one cost metric at a time: overlap in the BEV. To potentially improve class solutions, MAD could be incorporated into the optimization to ensure trajectories are adequately spaced. The brain is a particular organ where PTV and OARs are all contained within the parallel encompassing OAR. The dose metric V12Gy could be optimized further by incorporating shallow beam path considerations as in the third manuscript.

In the manuscript of Chapter 5, delivery efficiency was not considered. Motion management is a significant clinical problem in lung SABR which would be exacerbated with longer treatments requiring many arcs and intra-fractional imaging. Conversely, the short arcs offered in this manuscript could facilitate breath hold procedures and contribute to shortening delivery. To address the large number of arcs, the optimization from Chapter 6 could be applied to bring the arc number down to a number comparable to current clinical practice. However, this could result in inferior dosimetric plan quality, another subject for future work. Future work is required on the efficiency of combining optimized non-coplanar arcs with intra-fractional imaging. The shallow path length method could also be used in combination with the methods of Chapter 5 to include considerations for the ipsilateral lung which is a parallel-encompassing OAR.

In the manuscript of Chapter 6 a trade-off was realized between statistically significant maximum dose sparing found in Chapters 4 and 5 between encompassing and non-encompassing OARs. The cost equation presented in Chapter 6 may require unique parallel and serial weighting factors for each biological OAR type being used. For example, the “urgent sparing factor”[29] could be applied. However, if other OARs are spared the same degree of liver sparing may not be realized.

For each manuscript, optimization methods were created for arc trajectories while bearing in mind that IMRT ports and dynamic trajectories are also current areas of interest. The class solution methodology of Chapter 4 could easily be subjected to a optimized IMRT port search, bi-directional gradient search[30], or A* algorithm[7]. More work would be required to extend these pathfinding algorithms to Chapters 5 and 6. To optimize the candidate arc selection process, the non-collisional space could be randomly subdivided and subjected to a static port or dynamic path search that could be ranked using the same stochastic search methods provided in those manuscripts.

Clinical translation of trajectories that include increased non-coplanar couch angles could require additional quality control (QC) and quality assurance (QA). These tests would need to account for patient specific verification QA, intrafractional imaging, and extension of tests to dynamic trajectories. It is possible for dynamic trajectories that a dynamic Winston – Lutz test could be developed as well as additional monthly QC tests. Future work should investigate standardization of these tests for clinical translation of non-coplanar trajectories.

Finally, the clinical utility of these non-coplanar arc optimizations needs to be examined for other anatomic sites (spine, prostate, accelerated partial breast, pancreas, kidney, stomach, etc). Multimetases cases could also be investigated and optimized using the methods of MacDonald *et al*.[6,31,131]

7.3 Concluding Remarks

In this dissertation, patient specific non-coplanar arc optimizations were robustly characterized and evaluated for three common SABR sites. They fill a void in the literature of non-coplanar arc optimizations and have the potential to inform further developments in the field. They offer advantages compared to the current standard of clinical practice in terms of low and high dose reduction to OARs with varying biological complexity. This is achieved by means of BEV, arc sampling, and efficiency optimization along arc trajectories with systematic and stochastic formulations. These non-coplanar arc optimizations also aim to provide automated solutions to aid planners that offer minimal disruptions to current clinical procedures. They are presently ready to implement in any treatment planning system that has the capacity for VMAT.

Bibliography

1. Society CC. Canadian Cancer Statistics: A 2022 special report on cancer prevalence. . 2022. http://cancer.ca/Canadian-Cancer-Statistics-2022-EN Accessed May, 2023.

2. Organization WH. *Constitution.* World Health Organization; 1989.

3. Khan FM, Sperduto PW, Gibbons JP. *Khan's Treatment Planning in Radiation Oncology.* Lippincott Williams & Wilkins; 2021.

4. Otto K. Volumetric modulated arc therapy: IMRT in a single gantry arc. *Medical physics.* 2008;35(1):310-317.

5. MacDonald RL, Syme A, Little B, Ward L, Thomas CG. Toward the combined optimization of dynamic axes (CODA) for stereotactic radiotherapy and radiosurgery using fixed couch trajectories. *Medical physics.* 2020;47(2):307-316.

6. Lee E, MacDonald RL, Thomas CG, Syme A. Intra-arc binary collimation with dynamic axes trajectory optimization for the SRS treatment of multiple metastases with multiple prescriptions. *Medical Physics.* 2022;49(7):4305-4321.

7. Guyer G, Mueller S, Koechli C, et al. Enabling non-isocentric dynamic trajectory radiotherapy by integration of dynamic table translations. *Physics in Medicine & Biology.* 2022;67(17):175003.

8. Podgoršak EB. *Radiation physics for medical physicists.* Vol 1: Springer; 2006.

9. Reed AB. The history of radiation use in medicine. In. Vol 53: Elsevier; 2011:3S-5S.

10. Hall EJ, Giaccia AJ. *Radiobiology for the Radiologist.* Vol 6: Philadelphia; 2006.

11. Smyth G, Evans PM, Bamber JC, Bedford JL. Recent developments in non-coplanar radiotherapy. *The British journal of radiology.* 2019;92(1097):20180908.

12. MacDonald RL, Lincoln J, Church C, Thomas C, Syme A. Mean Arc Distance (MAD): a quantity to compare trajectory 4π sampling in single target cranial stereotactic radiotherapy. *Biomedical Physics & Engineering Express.* 2022;8(5):055006.

13. Clarke R. THE STRUCTURE AND FUNCTIONS OF THE CEREBELLUM EXAMINED BY A NEW METHOD. By SIR VICTOR HORSLEY, FRS, FRCS, AND. *Brain: A Journal of Neurology.* 1908;45.

14. Folkert MR, Timmerman RD. Stereotactic ablative body radiosurgery (SABR) or Stereotactic body radiation therapy (SBRT). *Advanced drug delivery reviews.* 2017;109:3-14.

15. Leksell L. The stereotactic method and radiosurgery of the brain. *Acta chir scand.* 1951;102(4):316-319.

16. Andrews DW, Scott CB, Sperduto PW, et al. Whole brain radiation therapy with or without stereotactic radiosurgery boost for patients with one to three brain metastases: phase III results of the RTOG 9508 randomised trial. *The Lancet.* 2004;363(9422):1665-1672.

17. Dawson LA, Zhu A, Knox J, et al. Radiation Therapy Oncology Group RTOG 1112 randomized phase III study of sorafenib versus stereotactic body radiation therapy followed by sorafenib in hepatocellular carcinoma. *Radiation Oncology Available online: https://www ctsu org.* 2020.

18. Videtic GM, Hu C, Singh AK, et al. A randomized phase 2 study comparing 2 stereotactic body radiation therapy schedules for medically inoperable patients with stage I peripheral non-small cell lung cancer: NRG Oncology RTOG 0915 (NCCTG N0927). *International Journal of Radiation Oncology* Biology* Physics.* 2015;93(4):757-764.

19. Fowler JF. The linear-quadratic formula and progress in fractionated radiotherapy. *The British journal of radiology.* 1989;62(740):679-694.

20. Benedict SH, Schlesinger DJ, Goetsch SJ, Kavanagh BD. *Stereotactic radiosurgery and stereotactic body radiation therapy.* CRC Press; 2014.

21. Wu Q, Mohan R, Niemierko A. IMRT optimization based on the generalized equivalent uniform dose (EUD). Paper presented at: Proceedings of the 22nd Annual International Conference of the IEEE Engineering in Medicine and Biology Society (Cat. No. 00CH37143)2000.

22. Dong P, Lee P, Ruan D, et al. 4π noncoplanar stereotactic body radiation therapy for centrally located or larger lung tumors. *International Journal of Radiation Oncology* Biology* Physics.* 2013;86(3):407-413.

23. Dong P, Lee P, Ruan D, et al. 4π non-coplanar liver SBRT: a novel delivery technique. *International Journal of Radiation Oncology* Biology* Physics.* 2013;85(5):1360-1366.

24. Fix MK, Frei D, Volken W, et al. Part 1: Optimization and evaluation of dynamic trajectory radiotherapy. *Medical physics.* 2018;45(9):4201-4212.

25. Mueller S, Manser P, Volken W, et al. Part 2: Dynamic mixed beam radiotherapy (DYMBER): Photon dynamic trajectories combined with modulated electron beams. *Medical physics.* 2018;45(9):4213-4226.

26. Trifiletti DM, Chao ST, Sahgal A, Sheehan JP. *Stereotactic Radiosurgery and Stereotactic Body Radiation Therapy.* Springer; 2019.

27. Mahajan A, Ahmed S, McAleer MF, et al. Post-operative stereotactic radiosurgery versus observation for completely resected brain metastases: a single-centre, randomised, controlled, phase 3 trial. *The lancet oncology.* 2017;18(8):1040-1048.

28. Kirkpatrick JP, Wang Z, Sampson JH, et al. Defining the optimal planning target volume in image-guided stereotactic radiosurgery of brain metastases: results of a randomized trial. *International Journal of Radiation Oncology* Biology* Physics.* 2015;91(1):100-108.

29. MacDonald RL, Robar JL, Thomas CG. Overlap-guided fixed-patient support positioning optimization for cranial SRT. *Medical physics.* 2017;44(1):17-27.

30. MacDonald RL, Thomas CG. Dynamic trajectory-based couch motion for improvement of radiation therapy trajectories in cranial SRT. *Medical physics.* 2015;42(5):2317-2325.

31. MacDonald RL, Thomas CG, Ward L, Syme A. Intra-arc binary collimation algorithm for the optimization of stereotactic radiotherapy treatment of multiple metastases with multiple prescriptions. *Medical physics.* 2018;45(12):5597-5607.

32. Mann TD, Ploquin NP, Gill WR, Thind KS. Development and clinical implementation of eclipse scripting-based automated patient-specific collision avoidance software. *Journal of Applied Clinical Medical Physics.* 2019;20(9):12-19.

33. Mann TD, Thind KS, Ploquin NP. Fast stereotactic radiosurgery planning using patient-specific beam angle optimization and automation. *Physics and Imaging in Radiation Oncology.* 2022;21:90-95.

34. Mullins J, Renaud MA, Heng V, Ruo R, DeBlois F, Seuntjens J. Trajectory-based VMAT for cranial targets with delivery at shortened SAD. *Medical Physics.* 2020;47(7):3103-3112.

35. Mullins J, Renaud MA, Serban M, Seuntjens J. Simultaneous trajectory generation and volumetric modulated arc therapy optimization. *Medical Physics.* 2020;47(7):3078-3090.

36. Church C, MacDonald RL, Parsons D, Syme A. Evaluation of plan quality and treatment efficiency in cranial stereotactic radiosurgery treatment plans with a variable source-to-axis distance. *Medical Physics.* 2023.

37. Videtic GM, Stephans KL. The role of stereotactic body radiotherapy in the management of non-small cell lung cancer: an emerging standard for the medically inoperable patient? *Current oncology reports.* 2010;12:235-241.

38. Uematsu M, Shioda A, Suda A, et al. Computed tomography-guided frameless stereotactic radiotherapy for stage I non-small cell lung cancer: a 5-year experience. *International Journal of Radiation Oncology* Biology* Physics.* 2001;51(3):666-670.

39. Timmerman R, Papiez L, McGarry R, et al. Extracranial stereotactic radioablation: results of a phase I study in medically inoperable stage I non-small cell lung cancer. *Chest.* 2003;124(5):1946-1955.

40. McGarry RC, Papiez L, Williams M, Whitford T, Timmerman RD. Stereotactic body radiation therapy of early-stage non–small-cell lung carcinoma: Phase I study. *International Journal of Radiation Oncology* Biology* Physics.* 2005;63(4):1010-1015.

41. Knox JJ, Cleary SP, Dawson LA. Localized and systemic approaches to treating hepatocellular carcinoma. *Journal of clinical oncology: official journal of the American Society of Clinical Oncology.* 2015;33(16):1835-1844.

42. Munoz-Schuffenegger P, Ng S, Dawson LA. Radiation-induced liver toxicity. Paper presented at: Seminars in radiation oncology2017.

43. Pan CC, Kavanagh BD, Dawson LA, et al. Radiation-associated liver injury. *International Journal of Radiation Oncology* Biology* Physics.* 2010;76(3):S94-S100.

44. Herfarth KK, Debus Jr, Lohr F, et al. Stereotactic single-dose radiation therapy of liver tumors: results of a phase I/II trial. *Journal of Clinical Oncology.* 2001;19(1):164-170.

45. Regina VT, Hawkins M, Lockwood G, et al. Phase I study of individualized stereotactic body radiotherapy for hepatocellular carcinoma and intrahepatic cholangiocarcinoma. *J Clin Oncol.* 2008;26(4):657-664.

46. Chang DT, Swaminath A, Kozak M, et al. Stereotactic body radiotherapy for colorectal liver metastases: a pooled analysis. *Cancer.* 2011;117(17):4060-4069.

47. Mendez Romero A, Wunderink W, Hussain SM, et al. Stereotactic body radiation therapy for primary and metastatic liver tumors: A single institution phase i-ii study. *Acta oncologica.* 2006;45(7):831-837.

48. Jang WI, Kim M-S, Bae SH, et al. High-dose stereotactic body radiotherapy correlates increased local control and overall survival in patients with inoperable hepatocellular carcinoma. *Radiation oncology.* 2013;8(1):1-12.

49. Blomgren H, Lax I, Näslund I, Svanström R. Stereotactic high dose fraction radiation therapy of extracranial tumors using an accelerator: clinical experience of the first thirty-one patients. *Acta oncologica.* 1995;34(6):861-870.

50. Bujold A, Massey CA, Kim JJ, et al. Sequential phase I and II trials of stereotactic body radiotherapy for locally advanced hepatocellular carcinoma. *J Clin Oncol.* 2013;31(13):1631-1639.

51. Takeda A, Sanuki N, Tsurugai Y, et al. Phase 2 study of stereotactic body radiotherapy and optional transarterial chemoembolization for solitary hepatocellular carcinoma not amenable to resection and radiofrequency ablation. *Cancer.* 2016;122(13):2041-2049.

52. Grimm J, Marks LB, Jackson A, Kavanagh BD, Xue J, Yorke E. High dose per fraction, hypofractionated treatment effects in the clinic (HyTEC): an overview. *International journal of radiation oncology, biology, physics.* 2021;110(1):1-10.

53. Marks LB, Yorke ED, Jackson A, et al. Use of normal tissue complication probability models in the clinic. *International Journal of Radiation Oncology* Biology* Physics.* 2010;76(3):S10-S19.

54. Emami B, Lyman J, Brown A, et al. Tolerance of normal tissue to therapeutic irradiation. *International Journal of Radiation Oncology* Biology* Physics.* 1991;21(1):109-122.

55. Burman C, Kutcher G, Emami B, Goitein M. Fitting of normal tissue tolerance data to an analytic function. *International Journal of Radiation Oncology* Biology* Physics.* 1991;21(1):123-135.

56. Kearney V, Cheung JP, McGuinness C, Solberg TD. CyberArc: a non-coplanar-arc optimization algorithm for CyberKnife. *Physics in Medicine & Biology.* 2017;62(14):5777.

57. Bedford JL, Nill S, Oelfke U. Dosimetric accuracy of delivering SBRT using dynamic arcs on Cyberknife. *Medical physics.* 2020;47(4):1533-1544.

58. Mendel JT, Schroeder S, Plitt A, et al. Expanded radiosurgery capabilities utilizing gamma knife icon™. *Cureus.* 2021;13(3).

59. Yang W, Jones R, Lu W, et al. Feasibility of non-coplanar tomotherapy for lung cancer stereotactic body radiation therapy. *Technology in cancer research & treatment.* 2011;10(4):307-315.

60. Yuasa M, Kurosaki H. Noncoplanar radiation using tomotherapy: a phantom study. *Technology in Cancer Research & Treatment.* 2020;19:1533033820945776.

61. Meyer J, Hummel S, Cho P, Austin-Seymour M, Phillips M. Automatic selection of non-coplanar beam directions for three-dimensional conformal radiotherapy. *The British journal of radiology.* 2005;78(928):316-327.

62. Yang Y, Zhang P, Happersett L, et al. Choreographing couch and collimator in volumetric modulated arc therapy. *International Journal of Radiation Oncology* Biology* Physics.* 2011;80(4):1238-1247.

63. Shepard DM, Earl MA, Li XA, Naqvi S, Yu C. Direct aperture optimization: a turnkey solution for step-and-shoot IMRT. *Medical physics.* 2002;29(6):1007-1018.

64. Ulmer W, Brenneisen W. Application of an Analytical Pencil Beam Model to Stereotactic Radiation Therapy Planning. *Journal of Radiosurgery.* 1998;1(3):169-176.

65. Ulmer W, Harder D. A triple Gaussian pencil beam model for photon beam treatment planning. *Zeitschrift für medizinische Physik.* 1995;5(1):25-30.

66. Han T, Mikell JK, Salehpour M, Mourtada F. Dosimetric comparison of Acuros XB deterministic radiation transport method with Monte Carlo and model-based convolution methods in heterogeneous media. *Medical Physics.* 2011;38(5):2651-2664.

67. Lewis EE, Miller WF. Computational methods of neutron transport. 1984.

68. Sarkar B, Ganesh T, Munshi A, Manikandan A, Mohanti BK. 4π radiotherapy using a linear accelerator: A misnomer in violation of the solid geometric boundary conditions in three-dimensional Euclidean space. *Journal of medical physics.* 2019;44(4):283.

69. Sarkar B. In regard to "Tran A, Zhang J, Woods K, Yu V, Nguyen D, Gustafson G, Rosen L, Sheng K. Treatment planning comparison of IMPT, VMAT and 4π radiotherapy for prostate cases. *Radiation oncology.* 2017;12(1):10.

70. Sarkar B. In Regard to Dong et al. *International Journal of Radiation Oncology, Biology, Physics.* 2018;101(3):741-742.

71. Commission I. Radiotherapy equipment—coordinates, movements and scales. *IEC1217.* 1996.

72. Yu V, Y, Landers A, Woods K, et al. A prospective 4π radiation therapy clinical study in recurrent high-grade glioma patients. *International Journal of Radiation Oncology* Biology* Physics.* 2018;101(1):144-151.

73. Wang G, Wang H, Zhuang H, Yang R. An Investigation of Non-Coplanar Volumetric Modulated Radiation Therapy for Locally Advanced Unresectable Pancreatic Cancer Using a Trajectory Optimization Method. *Frontiers in Oncology.* 2021;11:717634.

74. Smyth G, Bamber JC, Evans PM, Bedford JL. Trajectory optimization for dynamic couch rotation during volumetric modulated arc radiotherapy. *Physics in Medicine & Biology.* 2013;58(22):8163.

75. Bedford JL, Smyth G, Hanson IM, Tree AC, Dearnaley DP, Hansen VN. Quality of treatment plans and accuracy of in vivo portal dosimetry in hybrid intensity-modulated radiation therapy and volumetric modulated arc therapy for prostate cancer. *Radiotherapy and Oncology.* 2016;120(2):320-326.

76. Smyth G, Evans PM, Bamber JC, et al. Non-coplanar trajectories to improve organ at risk sparing in volumetric modulated arc therapy for primary brain tumors. *Radiotherapy and Oncology.* 2016;121(1):124-131.

77. Northway C, Lincoln JD, Little B, Syme A, Thomas CG. Patient-specific collision zones for 4π trajectory optimized radiation therapy. *Medical Physics.* 2022;49(3):1407-1416.

78. Shaitelman SF, Kim LH, Yan D, Martinez AA, Vicini FA, Grills IS. Continuous arc rotation of the couch therapy for the delivery of accelerated partial breast irradiation: a treatment planning analysis. *International Journal of Radiation Oncology* Biology* Physics.* 2011;80(3):771-778.

79. Clark GM, Popple RA, Young PE, Fiveash JB. Feasibility of single-isocenter volumetric modulated arc radiosurgery for treatment of multiple brain metastases. *International Journal of Radiation Oncology* Biology* Physics.* 2010;76(1):296-302.

80. Ohira S, Ueda Y, Akino Y, et al. HyperArc VMAT planning for single and multiple brain metastases stereotactic radiosurgery: a new treatment planning approach. *Radiation Oncology.* 2018;13(1):1-9.

81. Slosarek K, Bekman B, Wendykier J, Grządziel A, Fogliata A, Cozzi L. In silico assessment of the dosimetric quality of a novel, automated radiation treatment planning strategy for linac-based radiosurgery of multiple brain metastases and a comparison with robotic methods. *Radiation Oncology.* 2018;13:1-10.

82. Woods K, Chin RK, Cook KA, et al. Automated non-coplanar VMAT for dose escalation in recurrent head and neck cancer patients. *Cancers.* 2021;13(8):1910.

83. Woods K, Nguyen D, Tran A, et al. Viability of Noncoplanar VMAT for liver SBRT compared with coplanar VMAT and beam orientation optimized 4π IMRT. *Advances in radiation oncology.* 2016;1(1):67-75.

84. Bellman R. On a routing problem. *Quarterly of applied mathematics.* 1958;16(1):87-90.

85. Okoli F, Bert J, Abdelaziz S, Boussion N, Visvikis D. Optimizing the Beam Selection for Noncoplanar VMAT by Using Simulated Annealing Approach. *IEEE Transactions on Radiation and Plasma Medical Sciences.* 2021;6(5):609-618.

86. Fahimian B, Yu V, Horst K, Xing L, Hristov D. Trajectory modulated prone breast irradiation: a LINAC-based technique combining intensity modulated delivery and motion of the couch. *Radiotherapy and Oncology.* 2013;109(3):475-481.

87. Popescu CC, Beckham WA, Patenaude VV, Olivotto IA, Vlachaki MT. Simultaneous couch and gantry dynamic arc rotation (CG-Darc) in the treatment of breast cancer with accelerated partial breast irradiation (APBI): a feasibility study. *Journal of applied clinical medical physics.* 2013;14(1):161-175.

88. Liang J, Atwood T, von Eyben R, et al. Trajectory modulated arc therapy: a fully dynamic delivery with synchronized couch and gantry motion significantly improves dosimetric indices correlated with poor cosmesis in accelerated partial breast irradiation. *International Journal of Radiation Oncology* Biology* Physics.* 2015;92(5):1148-1156.

89. Podgorsak EB, Olivier A, Pla M, Hazel J, de Lotbinière A, Pike B. Physical aspects of dynamic stereotactic radiosurgery. *Stereotactic and Functional Neurosurgery.* 1987;50(1-6):263-268.

90. Podgorsak EB, Olivier A, Pla M, Lefebvre P-Y, Hazel J. Dynamic stereotactic radiosurgery. *International Journal of Radiation Oncology* Biology* Physics.* 1988;14(1):115-126.

91. Bertholet J, Mackeprang P-H, Mueller S, et al. Organ-at-risk sparing with dynamic trajectory radiotherapy for head and neck cancer: comparison with volumetric arc therapy on a publicly available library of cases. *Radiation oncology.* 2022;17(1):122.

92. Hart PE, Nilsson NJ, Raphael B. A formal basis for the heuristic determination of minimum cost paths. *IEEE transactions on Systems Science and Cybernetics.* 1968;4(2):100-107.

93. Dijksta EW. A note on two problems in connexion with graphs. *Numerische mathematik.* 1959;1(1):269-271.

94. Lyu Q, Victoria YY, Ruan D, Neph R, O'Connor D, Sheng K. A novel optimization framework for VMAT with dynamic gantry couch rotation. *Physics in Medicine & Biology.* 2018;63(12):125013.

95. Wilson B, Otto K, Gete E. A simple and robust trajectory-based stereotactic radiosurgery treatment. *Medical Physics.* 2017;44(1):240-248.

96. Cignoni P, Callieri M, Corsini M, Dellepiane M, Ganovelli F, Ranzuglia G. Meshlab: an open-source mesh processing tool. Paper presented at: Eurographics Italian chapter conference2008.

97. Rogers D. Fifty years of Monte Carlo simulations for medical physics. *Physics in Medicine & Biology.* 2006;51(13):R287.

98. Siddon RL. Fast calculation of the exact radiological path for a three-dimensional CT array. *Medical physics.* 1985;12(2):252-255.

99. Möller T, Trumbore B. Fast, minimum storage ray/triangle intersection. In: *ACM SIGGRAPH 2005 Courses.* 2005:7-es.

100. Lincoln JD, MacDonald RL, Little B, Syme A, Thomas CG. Comparison of anatomically informed class solution template trajectories with patient-specific trajectories for stereotactic radiosurgery and radiotherapy. *Journal of Applied Clinical Medical Physics.* 2022;23(11):e13765.

101. Bijman R, Rossi L, Sharfo AW, et al. Automated radiotherapy planning for patient-specific exploration of the trade-off between tumor dose coverage and predicted radiation-induced toxicity—a proof of principle study for prostate cancer. *Frontiers in Oncology.* 2020;10:943.

102. Cilla S, Ianiro A, Romano C, Deodato F, Macchia G, Buwenge M. Template based automation of treatment planning in advanced radiotherapy: a comprehensive dosimetric and clinical evaluation. *Sci Rep.* 2020;10:423.

103. Ghobadi K, Ghaffari HR, Aleman DM, Jaffray DA, Ruschin M. Automated treatment planning for a dedicated multi-source intracranial radiosurgery treatment unit using projected gradient and grassfire algorithms. *Medical physics.* 2012;39(6Part1):3134-3141.

104. Winkel D, Bol GH, Van Asselen B, et al. Development and clinical introduction of automated radiotherapy treatment planning for prostate cancer. *Physics in Medicine & Biology.* 2016;61(24):8587.

105. Clarke S, Goodworth J, Westhuyzen J, et al. Software-based evaluation of a class solution for prostate IMRT planning. *Reports of Practical Oncology and Radiotherapy.* 2017;22(6):441-449.

106. Hoffmann M, Pacey J, Goodworth J, et al. Analysis of a volumetric-modulated arc therapy (VMAT) single phase prostate template as a class solution. *Reports of Practical Oncology and Radiotherapy.* 2019;24(1):92-96.

107. Huang L, Qi P, Chao S, Xia P. A treatment planning class solution for hippocampal avoidance whole brain irradiation using volumetric-modulated arc radiotherapy. *Appl Radiat Oncol.* 2013;4:8-11.

108. Weksberg DC, Palmer MB, Vu KN, et al. Generalizable class solutions for treatment planning of spinal stereotactic body radiation therapy. *International Journal of Radiation Oncology* Biology* Physics.* 2012;84(3):847-853.

109. Collins DL, Neelin P, Peters TM, Evans AC. Automatic 3D intersubject registration of MR volumetric data in standardized Talairach space. *Journal of computer assisted tomography.* 1994;18(2):192-205.

110. Systems VM. *Varian PO_13.2.6 VMAT optimization algorithm.* 2018.

111. Ma C-MC. Physics and Dosimetric Principles of SRS and SBRT. *Mathews Journal of Cancer Science.* 2019;4(2):1-16.

112. Narayanasamy G, Desai D, Maraboyina S, Penagaricano J, Zwicker R, Johnson EL. A dose falloff gradient study in RapidArc planning of lung stereotactic body radiation therapy. *Journal of Medical Physics.* 2018;43(3):147.

113. Systems VM. *Varian AAA_13.2.6 Dose Calculation Algorithm.* 2018.

114. Paddick I. A simple scoring ratio to index the conformity of radiosurgical treatment plans. *Journal of neurosurgery.* 2000;93(supplement_3):219-222.

115. Paddick I, Lippitz B. A simple dose gradient measurement tool to complement the conformity index. *Journal of neurosurgery.* 2006;105(Supplement):194-201.

116. Lincoln JD, MacDonald RL, Syme A, Thomas CG. Static couch non-coplanar arc selection optimization for lung SBRT treatment planning. *Physics in Medicine & Biology.* 2023.

117. Webb S. Optimization of conformal radiotherapy dose distributions by simulated annealing: II. Inclusion of scatter in the 2D technique. *Physics in Medicine & Biology.* 1991;36(9):1227.

118. Bortfeld TR, Kahler DL, Waldron TJ, Boyer AL. X-ray field compensation with multileaf collimators. *International Journal of Radiation Oncology* Biology* Physics.* 1994;28(3):723-730.

119. Hardcastle N, Davies A, Foo K, Miller A, Metcalfe PE. Rectal dose reduction with IMRT for prostate radiotherapy. *Journal of medical imaging and radiation oncology.* 2010;54(3):235-248.

120. Guckenberger M, Flentje M. Intensity-Modulated Radiotherapy (IMRT) of Localized Prostate Cancer. *Strahlentherapie und Onkologie.* 2007;183(2).

121. Mendenhall WM, Amdur RJ, Palta JR. Intensity-modulated radiotherapy in the standard management of head and neck cancer: promises and pitfalls. *Journal of clinical oncology.* 2006;24(17):2618-2623.

122. Thilmann C, Zabel A, Nill S, et al. Intensity-modulated radiotherapy of the female breast. *Medical Dosimetry.* 2002;27(2):79-90.

123. Llacer J, Li S, Agazaryan N, Promberger C, Solberg TD. Non-coplanar automatic beam orientation selection in cranial IMRT: a practical methodology. *Physics in Medicine & Biology.* 2009;54(5):1337.

124. Yu V, Landers A, Woods K, et al. A Prospective 4PI Radiotherapy Clinical Trial in Recurrent Glioblastoma Multiforme (GBM) Patients. Paper presented at: MEDICAL PHYSICS2017.

125. Bentzen SM, Constine LS, Deasy JO, et al. Quantitative Analyses of Normal Tissue Effects in the Clinic (QUANTEC): an introduction to the scientific issues. *International Journal of Radiation Oncology* Biology* Physics.* 2010;76(3):S3-S9.

126. Bush K, Gagne I, Zavgorodni S, Ansbacher W, Beckham W. Dosimetric validation of Acuros® XB with Monte Carlo methods for photon dose calculations. *Medical physics.* 2011;38(4):2208-2221.

127. Woolson RF. Wilcoxon signed-rank test. *Wiley encyclopedia of clinical trials.* 2007.1-3.

128. QM Reis C, Little B, Lee MacDonald R, Syme A, Thomas CG, Robar JL. SBRT of ventricular tachycardia using 4pi optimized trajectories. *Journal of Applied Clinical Medical Physics.* 2021;22(12):72-86.

129. Meedt G, Alber M, Nüsslin F. Non-coplanar beam direction optimization for intensity-modulated radiotherapy. *Physics in Medicine & Biology.* 2003;48(18):2999.

130. Clark GM, Popple RA, Prendergast BM, et al. Plan quality and treatment planning technique for single isocenter cranial radiosurgery with volumetric modulated arc therapy. *Practical radiation oncology.* 2012;2(4):306-313.

131. MacDonald RL, Thomas CG, Syme A. Dynamic collimator trajectory algorithm for multiple metastases dynamic conformal arc treatment planning. *Medical physics.* 2018;45(1):5-17.

Appendix A Copyright Permission

A.1 PERMISSION FOR: COMPARISON OF ANATOMICALLY INFORMED CLASS SOLUTION TEMPLATE TRAJECTORIES FOR STEREOTACTIC RADIOSURGERY AND RADIOTHERAPY

Comparison of anatomically informed class solution template trajectories with patient-specific trajectories for stereotactic radiosurgery and radiotherapy

Author: Christopher Grant Thomas, Alasdair Syme, Brian Little, et al

Publication: Journal of Applied Clinical Medical Physics

Publisher: John Wiley and Sons

Date: Sep 2, 2022

© 2022 The Authors. Journal of Applied Clinical Medical Physics published by Wiley Periodicals, LLC on behalf of The American Association of Physicists in Medicine.

Open Access Article

This is an open access article distributed under the terms of the Creative Commons CC BY license, which permits unrestricted use, distribution, and reproduction in any medium, provided the original work is properly cited.

You are not required to obtain permission to reuse this article.

For an understanding of what is meant by the terms of the Creative Commons License, please refer to Wiley's Open Access Terms and Conditions.

Permission is not required for this type of reuse.

Wiley offers a professional reprint service for high quality reproduction of articles from over 1400 scientific and medical journals. Wiley's reprint service offers:

- Peer reviewed research or reviews
- Tailored collections of articles
- A professional high quality finish
- Glossy journal style color covers
- Company or brand customisation
- Language translations
- Prompt turnaround times and delivery directly to your office, warehouse or congress.

Please contact our Reprints department for a quotation. Email corporatesaleseurope@wiley.com or corporatesalesusa@wiley.com or corporatesalesDE@wiley.com.

Rightslink® by Copyright Clearance Center

A.2 PERMISSION FOR: STATIC COUCH NON-COPLANAR ARC SELECTION OPTIMIZATION FOR LUNG SBRT TREATMENT PLANNING

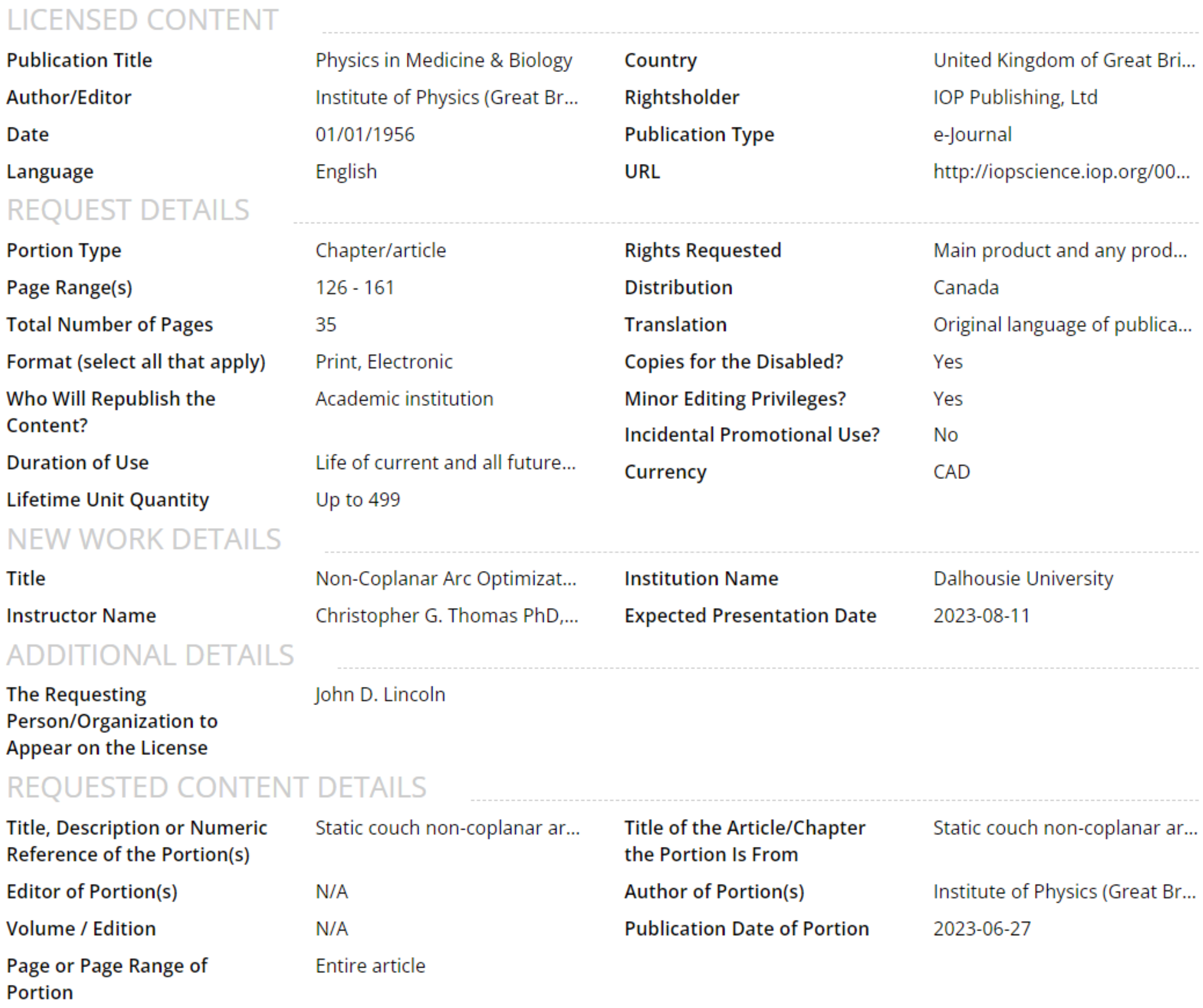

LICENSED CONTENT

Publication Title	Physics in Medicine & Biology	Country	United Kingdom of Great Bri...
Author/Editor	Institute of Physics (Great Br...	Rightsholder	IOP Publishing, Ltd
Date	01/01/1956	Publication Type	e-Journal
Language	English	URL	http://iopscience.iop.org/00...

REQUEST DETAILS

Portion Type	Chapter/article	Rights Requested	Main product and any prod...
Page Range(s)	126 - 161	Distribution	Canada
Total Number of Pages	35	Translation	Original language of publica...
Format (select all that apply)	Print, Electronic	Copies for the Disabled?	Yes
Who Will Republish the Content?	Academic institution	Minor Editing Privileges?	Yes
		Incidental Promotional Use?	No
Duration of Use	Life of current and all future...	Currency	CAD
Lifetime Unit Quantity	Up to 499		

NEW WORK DETAILS

Title	Non-Coplanar Arc Optimizat...	Institution Name	Dalhousie University
Instructor Name	Christopher G. Thomas PhD,...	Expected Presentation Date	2023-08-11

ADDITIONAL DETAILS

The Requesting Person/Organization to Appear on the License	John D. Lincoln

REQUESTED CONTENT DETAILS

Title, Description or Numeric Reference of the Portion(s)	Static couch non-coplanar ar...	Title of the Article/Chapter the Portion Is From	Static couch non-coplanar ar...
Editor of Portion(s)	N/A	Author of Portion(s)	Institute of Physics (Great Br...
Volume / Edition	N/A	Publication Date of Portion	2023-06-27
Page or Page Range of Portion	Entire article		